

THESIS

POTENTIAL VORTICITY AND ENERGY ASPECTS OF THE
MJO THROUGH EQUATORIAL WAVE THEORY

Submitted by

Matthew Thomas Masarik

Department of Atmospheric Science

In partial fulfillment of the requirements

for the Degree of Master of Science

Colorado State University

Fort Collins, Colorado

Spring 2007

COLORADO STATE UNIVERSITY

January 05, 2007

WE HEREBY RECOMMEND THAT THE THESIS PREPARED UNDER OUR SUPERVISION BY MATTHEW THOMAS MASARIK ENTITLED POTENTIAL VORTICITY AND ENERGY ASPECTS OF THE MJO THROUGH EQUATORIAL WAVE THEORY BE ACCEPTED AS FULFILLING IN PART REQUIREMENTS FOR THE DEGREE OF MASTER OF SCIENCE.

Committee on Graduate Work

Outside Member: Prof. Richard E. Eykholt

Department Member: Prof. David A. Randall

Co-Advisor: Prof. Thomas H. Vonder Haar

Advisor: Prof. Wayne H. Schubert

Department Head: Prof. Richard H. Johnson

ABSTRACT OF THESIS

POTENTIAL VORTICITY AND ENERGY ASPECTS OF THE MJO THROUGH EQUATORIAL WAVE THEORY

Considering linearized motion about a resting basic state, we derive analytical solutions of the equatorial β -plane primitive equations under the assumption that the flow is steady in a reference frame moving eastward with a diabatic forcing resembling a Madden-Julian oscillation (MJO) convective envelope. The spectral series solutions allow us to decompose the total response into equatorial wave components.

The diabatic source term in the potential vorticity (PV) principle contains a factor of βy which acts to suppress PV generation at the equator, while maximizing it at the poleward edges of the convection. In this way a moving heat source can produce two ribbons of lower tropospheric PV anomaly, a positive one off the equator in the northern hemisphere and a negative one off the equator in the southern hemisphere, with oppositely signed PV anomalies in the upper troposphere. An approximate relationship between the geopotential and streamfunction is used to formulate an invertibility principle. The balanced wind and mass fields recovered from inverting the primitive equation PV quite accurately reproduce the flow west of the forcing. While this result demonstrates the MJO wake response can be described by simple PV dynamics, it also illustrates the Kelvin response ahead of the convection cannot be captured within this balanced framework.

We then derive the primitive equation total energy principle which reduces to a balance between generation and dissipation under the assumed steady state. The total energy

can be expressed as a physical space integral, or equivalently as an infinite sum in spectral space through a Parseval relation. Using the spectral sum we can isolate the individual equatorial wave contributions to the total energy. The dependence of wave response energy on the horizontal shape, propagation speed, and meridional position of the prescribed forcing are examined by evaluating the Parseval relation for different values of these forcing parameters.

Matthew Thomas Masarik
Department of Atmospheric Science
Colorado State University
Fort Collins, Colorado 80523
Spring 2007

ACKNOWLEDGEMENTS

My sincerest gratitude goes to Dr. Wayne Schubert. I appreciate his patience and enjoy his genuine excitement for learning. His humble nature in spite of his exceptional insight is truly inspiring, and has given me a high ideal to strive for.

I would like to thank Dr. David Randall and Dr. Richard Eykholt for their willingness to discuss my research and the thoughtful feedback they have provided. I thank Dr. Tom Vonder Haar for his encouragement, and for the opportunity to work on this exciting project.

I am grateful to the entire Schubert research group for their friendship, for readily offering assistance whenever needed, and for the many stimulating conversations that have taught me to examine claims more critically and have pushed me to improve the rigor of my own arguments. A special thanks goes to Brian McNoldy for the expertise and time that went into producing most of the graphics within. Special thanks also goes to Paul Ciesielski for contributing material from previous work, and for sharing his thoughts on the MJO. I thank Rick Taft and Jonathan Vigh for providing technical support.

I am also grateful for my friends inside and outside this department. Their comradery has given me strength and their perspectives have been enlightening and inspiring.

My deepest sentiments go to my family for their invaluable love, encouragement, and support.

This research was supported by the DoD Center for Geosciences/Atmospheric Research at Colorado State University under Cooperative Agreement DAAD19-02-2-0005 and W911NF-06-2-0015 with the Army Research Laboratory.

DEDICATION

mark tami jason seth

CONTENTS

1	Introduction	1
1.1	Opening Remarks	1
1.2	Literature Review	3
1.3	Overview	15
2	Primitive Equation Model	17
2.1	Governing Equations	17
2.2	Separation of Horizontal and Vertical Structure	19
2.3	Model Diabatic Forcing	22
2.4	Horizontal Structure Problem	23
2.5	Solutions	31
3	Potential Vorticity Aspects	37
3.1	Primitive Equation Potential Vorticity	37
3.2	Parameters Controlling PV Wake	40
3.3	Invertibility Principle	42
3.4	Proposed Prognostic Equation	48
4	Energy Considerations	51
4.1	Energy Principle	51
4.2	Parseval Relation	54
4.3	Parameter Dependency	57
5	Conclusions	64
5.1	Chapter 2 Summary	64
5.2	Chapter 3 Summary	65
5.3	Chapter 4 Summary	67
 Appendix		
A	Conversion to the log-pressure vertical coordinate	69
B	Vertical normal mode transform	72
C	Transformation to the ξ-coordinate	75

D Eigenfunctions for zonally symmetric Rossby modes	76
E Meridional normal mode transform of the heating function	77
F Computational procedure	78
G Idealized PV principle solution	79
H Equatorial balance relation	80
I Group velocity concepts for discrete wavenumbers	81
Bibliography	84

Chapter 1

INTRODUCTION

1.1 Opening Remarks

The Madden-Julian oscillation (MJO) is a tropical weather phenomenon in which wave disturbances form quasi-periodically in the Indian ocean and propagate eastward. These disturbances exist on an intraseasonal time scale [longer than synoptic time scales (~ 2 weeks), though shorter than a season (90 days) (Lau and Waliser, 2005)] and consist of a convective region and its surrounding flow field. This wave pulse travels along the equator at an average speed of 5 ms^{-1} until it reaches the central Pacific where the convection dissipates due to lower sea surface temperatures. This marks the transition of the MJO from the convective phase to the dry phase, where the forced waves are free to propagate away. The dry phase is essentially the continued eastward movement of the now decoupled Kelvin response which travels at its free wave speed. This study is restricted to the convective phase of the MJO lifecycle.

By filtering outgoing longwave radiation (OLR) time series data for frequencies and wavenumbers characteristic of the MJO, a composite lifecycle of MJO convection can be constructed. In this view the negative OLR anomalies are used as a proxy for the convective region. Fig. 1.1 consists of panels at 6 day intervals showing the evolution of the OLR anomaly associated with the MJO during its convective phase.

The next section will discuss some of the literature regarding the MJO. As a testament to its complexity, the material available on this subject is vast and covers many facets. Since an exhaustive survey is not appropriate here, the following treatment will attempt

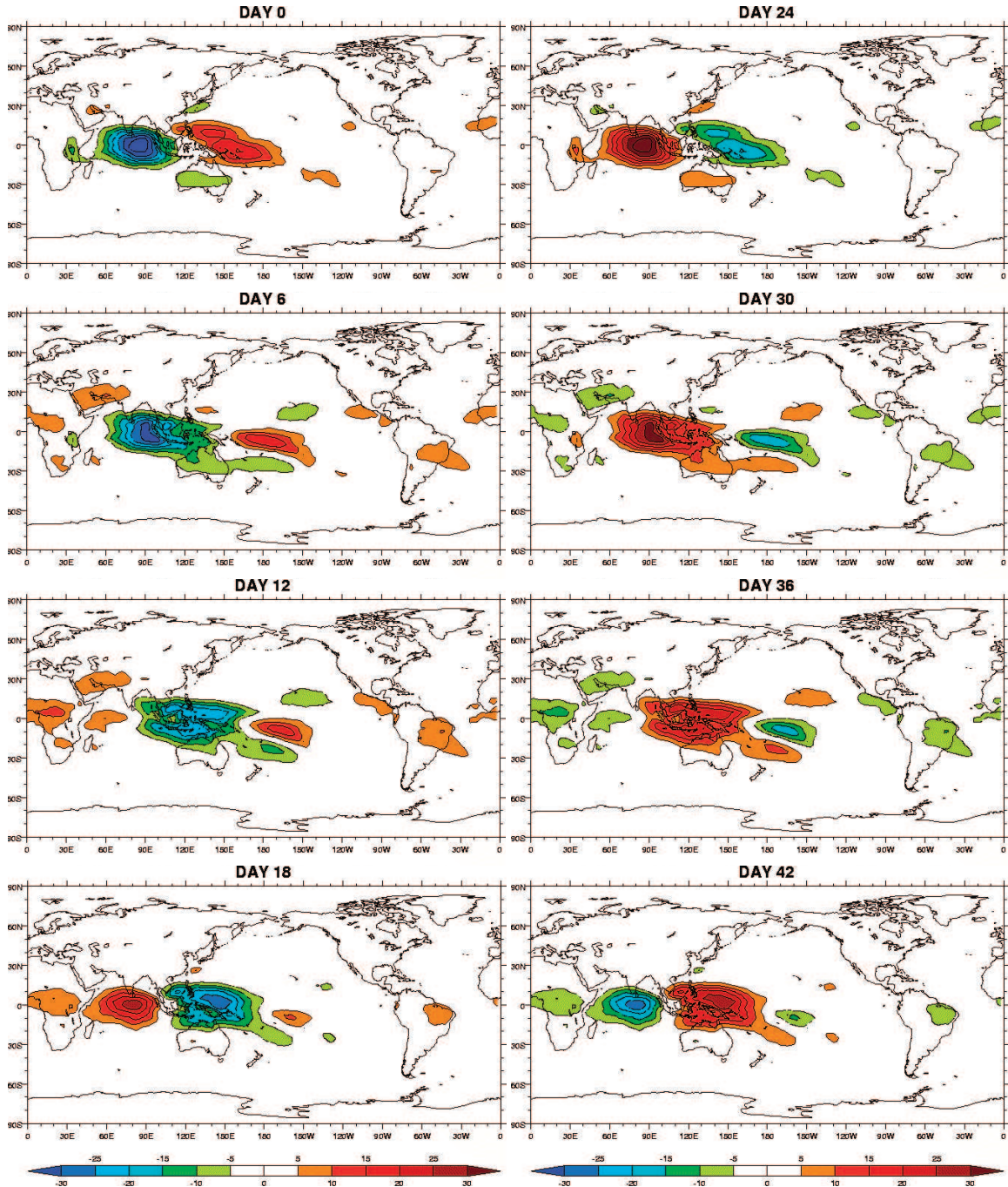


Figure 1.1: A composite lifecycle of MJO convection as seen through filtered OLR time series data. Negative OLR anomalies (cool colors) are used as a proxy for enhanced convection, denoting an active phase of the oscillation. Positive OLR anomalies (warm colors) are used as a proxy for suppressed convection, corresponding to an inactive phase. This figure is composed of select time snap shots originally from an animation (Matthews).

to establish the basic characteristics of the MJO (especially those most relevant to this study), as well as briefly cover modeling efforts and theoretical work. It's acknowledged that some well documented aspects, deemed not as crucial to this study, have been left out. In addition, only a sampling of the influential papers on the topics addressed were able to be covered. To mitigate this, some comprehensive reviews are mentioned which provide an introduction to many interesting aspects of this phenomenon and also contain references for further study.

1.2 Literature Review

The phenomenon most commonly referred to as the Madden-Julian oscillation (MJO) was discovered in 1970 by Roland Madden and Paul Julian (hereafter referred to as MJ) during research stimulated by the discovery of the Quasibiennial oscillation (QBO) (Madden and Julian, 2005). By spectrally analyzing approximately 10 years of rawinsonde data from Canton Island (3°S , 172°W) over a broad range of frequencies they observed an oscillation in the station pressure and zonal wind with a frequency lower than that of any hypothesized wave mode, but higher than any seasonal variation. Based on its spectral peak in the frequency range associated with periods of 41–53 days, MJ referred to the finding as a 40–50 day oscillation. They also reported that the low-level and upper-level zonal wind and pressure fields were out of phase and concluded the new phenomenon could most adequately be described as a large circulation cell oriented in the equatorial zonal plane (Madden and Julian, 1971). A year later MJ published a follow-up paper involving cross-spectral analysis of time series data from stations located in the tropics to study the spatial scale of the 40–50 day oscillation (Madden and Julian, 1972). Their results suggested that the oscillation has a global scale zonally but is restricted to the tropics (10°S , 10°N), and possessed features of a wave moving eastward from the Indian ocean to the eastern Pacific whose characteristics changed with time. The paper concluded by summarizing what was known about the oscillation at the time in a schematic (see Fig. 1.2).

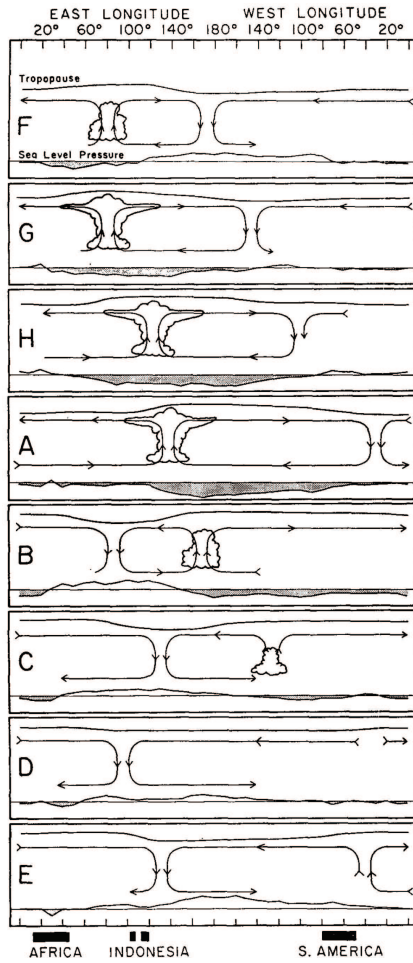


Figure 1.2: Reproduced from Madden and Julian (1972). Depicts the time and space variations in the zonal plane associated with the 40–50 day oscillation. Mean sea level pressure anomalies are represented in the bottom of each panel by the curve that deviates from the straight line, where the negative anomalies are shaded. The sketched cumulus clouds represent regions of enhanced large-scale convection, with streamlines indicating the associated zonal circulation. The curve at the top of each panel represents the relative tropopause height. Block continents are found at the bottom of the figure, and relative dates are given by letters (indexed from the surface low pressure anomaly at Canton Island). **F** - Surface low pressure anomaly over East Africa and the Indian ocean. Large scale convection initiates over the Indian ocean. Circulation cells form. **G** - Convection strengthens, pressure anomaly and eastern circulation cell spread eastward. **H** - Convection moving east across Indonesia. **A** - Surface low pressure anomaly over Canton Island. **B** - Convection starts to weaken, western circulation cell shrinks, and descending branch of circulation characteristic of the inactive phase is seen to the west. **C** - Convection decays further in the colder waters of the central Pacific. **D** - Convection is dead, subsidence dominates Indonesia. **E** - Subsiding branch continues to move east, surface high pressure anomaly over Canton Island, dry phase signal seen on eastern side of South America.

Space-time spectral analysis on 8-years of outgoing longwave radiation (OLR) data was employed by Nakazawa (1986) to look at the mean features of intraseasonal variation (ISV), in which he found strong power between the periods of 30–60 days. In this time range he identified clustering of active convective regions consisting of multiple synoptic scale convective cells with horizontal scale $O(1000 \text{ km})$ and a lifecycle of less than 10 days. He noted that both the 30–60 day variation and the synoptic scale convective regions it contained moved eastward. Nakazawa (1988) gave further detail of the fine structure within the convective region by analyzing 3-hourly geostationary satellite infrared data. The outcome was a heirarchical view of the convective components contained in an ISV envelope. The synoptic scale cells mentioned above were given the name “super clusters” (a term which is avoided during discussion of our convective forcing due to ambiguity), and were seen to be composed of mesoscale “cloud clusters” (CC), having a horizontal scale of $O(100 \text{ km})$. Surprisingly, these CC which have a lifecycle of 1–2 days, travel westward. It is by the successive eastward formation of each westward traveling CC that the super cluster moves eastward. These features are seen explicitly in the Hovmoller diagrams of Fig. 1.3.

Another look at the convective organization, and in addition the accompanying large-scale circulation disturbances, is provided by Hendon and Liebmann (1994). Composite lifecycles are constructed by regression of band-pass filtered winds, divergences, MSUT (microwave sounding unit temperature), and OLR for MJO episodes within an 11-year record that have a discrete large-scale convective signal present. The motivating question is whether the oscillation simply organizes existing convection on all scales such that co-operative growth with the circulation occurs, or if the multi-scale convective structure is responsible for the evolution of the oscillation. They observed that synoptic-scale variability is strongly modulated within the convective envelope, and that feedback between the circulation and convection occurs at this scale, though no predominant mode was detected. On the mesoscale, a predominant mode of variability with ~ 2 -day period was observed, though its small variance suggested its role in the MJO was more one of effect rather than

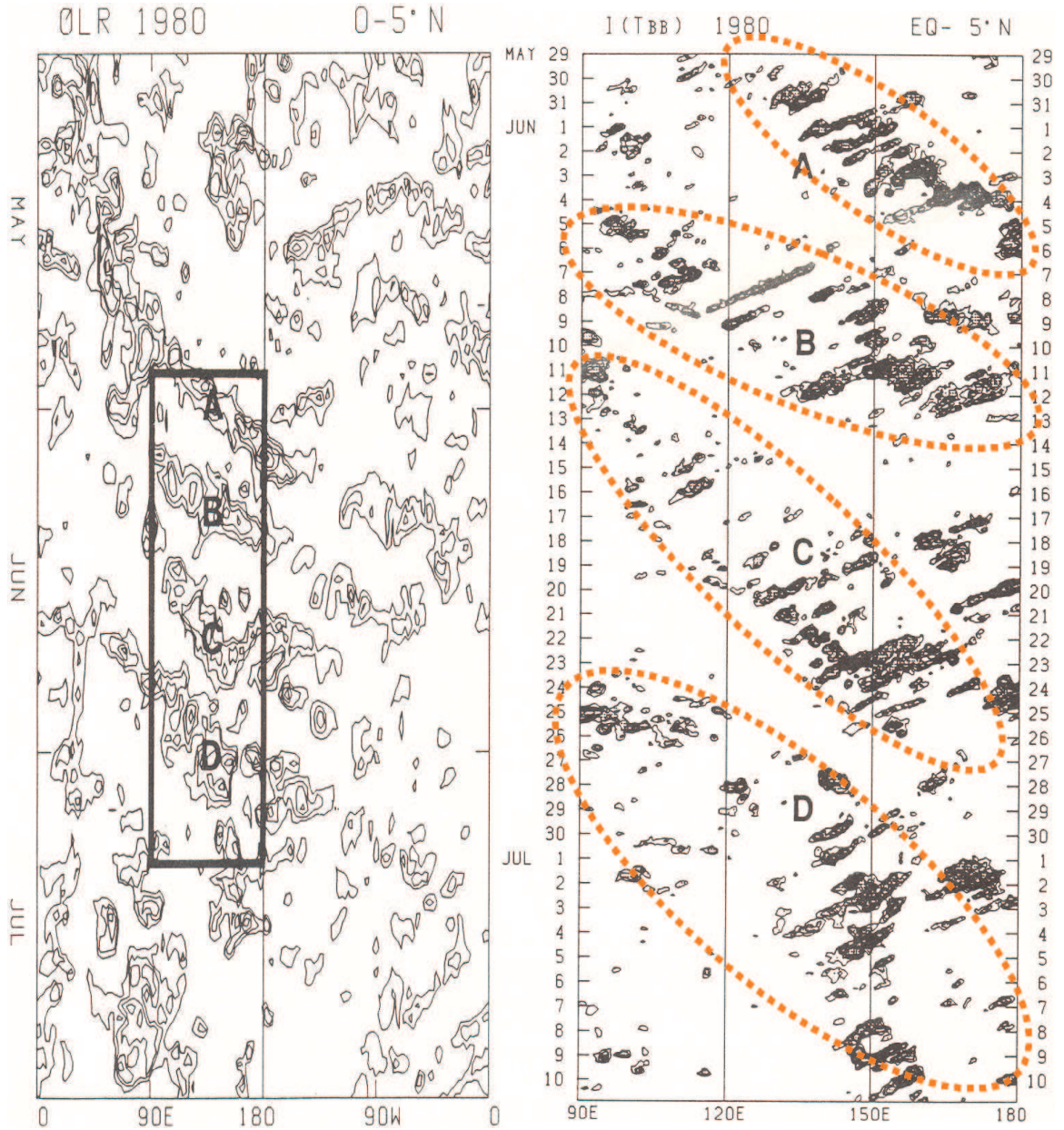


Figure 1.3: Reproduced from Nakazawa (1988). The figure on the left is a time-longitude section of transient (seasonal trend removed) OLR averaged between the equator and 5°N from May to July in 1980. Negative OLR anomalies are contoured in decrements of 30 W m^{-2} starting at -15 W m^{-2} . The letters **A**, **B**, **C**, and **D** label 4 super clusters. The figure on the right is a time-longitude section of the area mean black body temperature integrated between the equator and 5°N obtained from 3-hourly IR data from 29 May 00Z to 10 July 21Z, 1980 (corresponds to the thick-lined box in the left figure). The contour interval is 10 K and shading denotes regions where values are greater than 20 K. Dashed orange ellipses have been added to highlight the super clusters **A**–**D** composed of the westward propagating cloud clusters.

cause. Also noted was the observance of a Kelvin-like feature that appeared to be a distinct mode of synoptic-scale variability along the equator, though not unique to the convective envelope. The characteristics of this mode were reminiscent of Nakazawa's "super clusters" and were assumed to not play a major role in the evolution of the MJO.

A statistical study using radiosonde, reanalysis, and OLR data by Kiladis et al. (2005) examines the zonal and vertical structures of the MJO and their changes during eastward propagation. Fig. 1.4 displays a large-scale horizontal view of the MJO convection and circulation at 850 hPa and 200 hPa visualized through anomalous OLR (shading), streamfunction (contours), and winds (vectors). Some features to note at the 850 hPa level are the cyclonic Rossby gyres flanking the convection, the strong equatorial westerlies found to the west of and extending through the convection, and the broad, zonally long region of easterlies to the east of the convection. These circulation patterns have led to the general interpretation of the MJO flow as a convectively forced Rossby-Kelvin response. The heavy orange lines have been added to illustrate the zonal scale of the OLR minimum (darkest shading). Approximately 2/3 of this core convective region is contained within 20° of longitude. Noting that at the equator $111\text{ km} \approx 1^{\circ}$ of longitude, the east-west length of the entire minimum is $O(2000\text{ km} - 3000\text{ km})$. This scale is consistent with those found in other studies which have constructed composite MJO's using OLR data (Hendon and Salby, 1994; Hendon and Liebmann, 1994). Also consistent among these studies is the elliptical shape where the semi-major axis runs east-west. At the 200 hPa level there is divergent flow over and near much of the anomalous OLR region. Features corresponding to those in the low-level for a baroclinic structure can be seen (i.e., Rossby anticyclones, equatorial zonal winds of opposite sign from those at 850 hPa). This change in sign of the zonal winds with height is clearly seen in Fig. 1.5, which depicts the vertical structure of the zonal wind associated with Fig. 1.4. It is also evident that the magnitude of the upper-level zonal winds are approximately twice that of those in the low-level. The low-level westerlies are noticeably stronger than the low-level easterlies, though the easterlies have a longer zonal

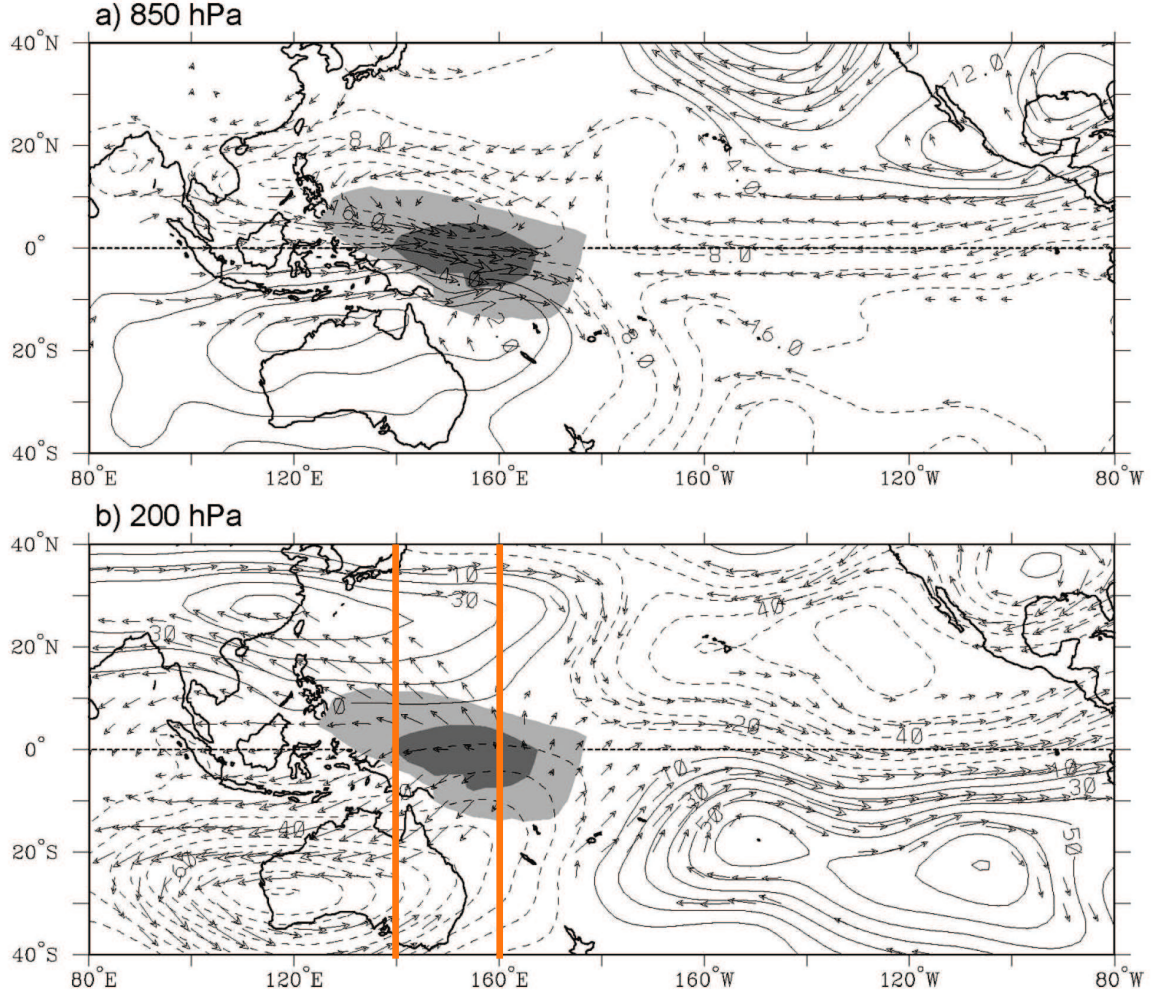


Figure 1.4: Reproduced from Kiladis et al. (2005). Anomalous OLR and circulation from ERA-15 reanalysis on day 0 associated with a -40 W m^{-2} perturbation in MJO-filtered OLR at the equator, 155°E for the period 1979–93, all seasons included; (a) 850 hPa and (b) 200 hPa. Dark (light) shading denotes OLR anomalies less than -32 W m^{-2} (-16 W m^{-2}). Streamfunction contour interval is (a) $4 \times 10^5 \text{ m}^2 \text{s}^{-1}$ and (a) $10 \times 10^5 \text{ m}^2 \text{s}^{-1}$. Locally statistically significant wind vectors at the 95% level are shown. The largest vectors are about 2 m s^{-1} in (a) and around 5 m s^{-1} in (b). The heavy orange lines in (b) have been added to delimit 20° of longitude over the OLR minimum.

extent. Notice that the OLR minimum is located within the low-level westerlies. This is stated to generally be the case, though the convective center can be found closer to the boundary between the low-level easterlies and westerlies. This structure is most likely to occur early in the lifecycle when the convection is over the Indian ocean, as the convection moves eastward, the low-level westerlies tend to push through and out in front of it.

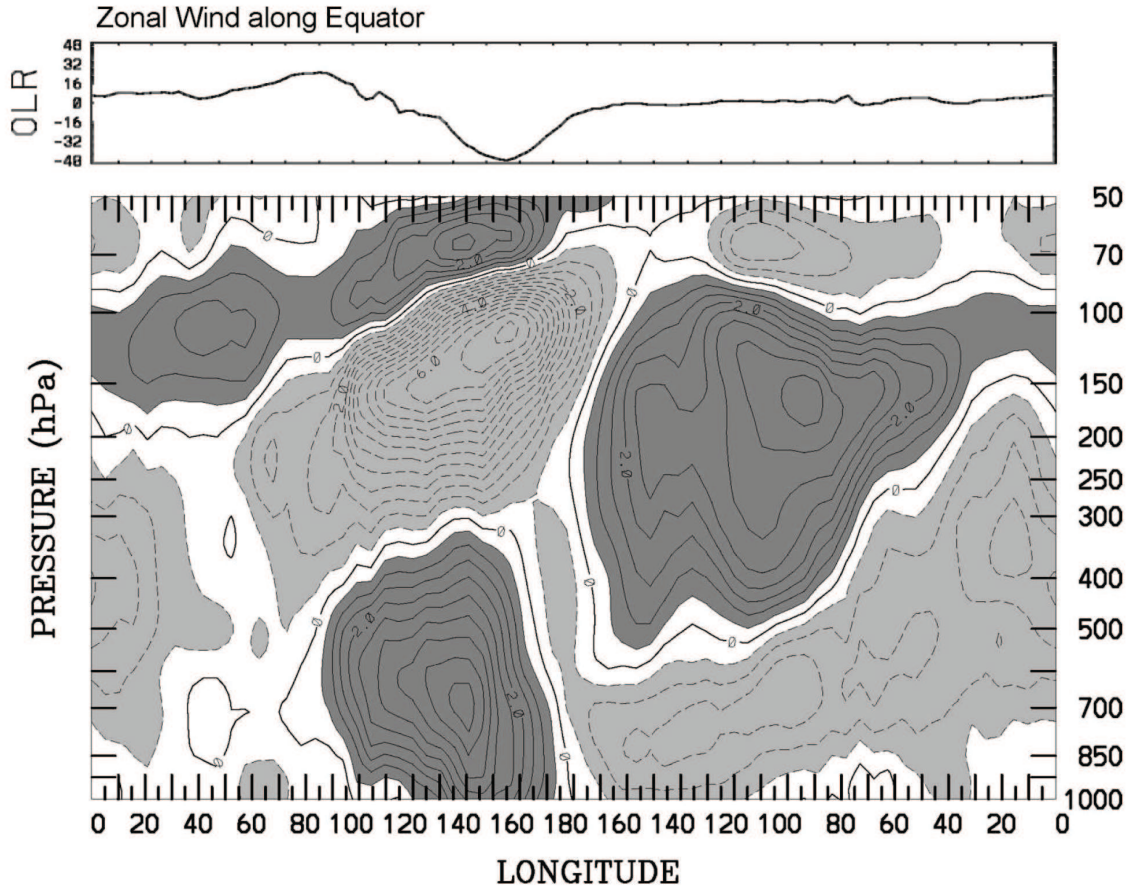


Figure 1.5: Reproduced from Kiladis et al. (2005). Zonal/height cross-section of anomalous zonal winds along the equator associated with Fig. 1.4. Contour interval is 0.5 m s^{-1} ; negative contours dashed. Dark (light) shading denotes anomalies greater than (less than) $\pm 0.5 \text{ m s}^{-1}$. The associated OLR anomaly along the equator is shown at the top in W m^{-2} .

The seasonality of the MJO in terms of low-level zonal winds and precipitation is documented by Zhang and Dong (2004). The main features can be summarized as follows: Near the equator, the MJO has a single peak season in the Indian and western Pacific oceans during the northern hemisphere winter. In the broader equatorial belt of the tropical Indian and western Pacific oceans the MJO migrates in latitude seasonally (see Fig. 1.6), and experiences two peak seasons. The primary peak season occurs during the northern hemisphere winter when the strongest signals are found between $5^\circ\text{--}10^\circ\text{S}$. The secondary peak season occurs in the northern hemisphere summer when the strongest signals are found between $5^\circ\text{--}10^\circ\text{N}$. This cross-equatorial migration is more pronounced in the western

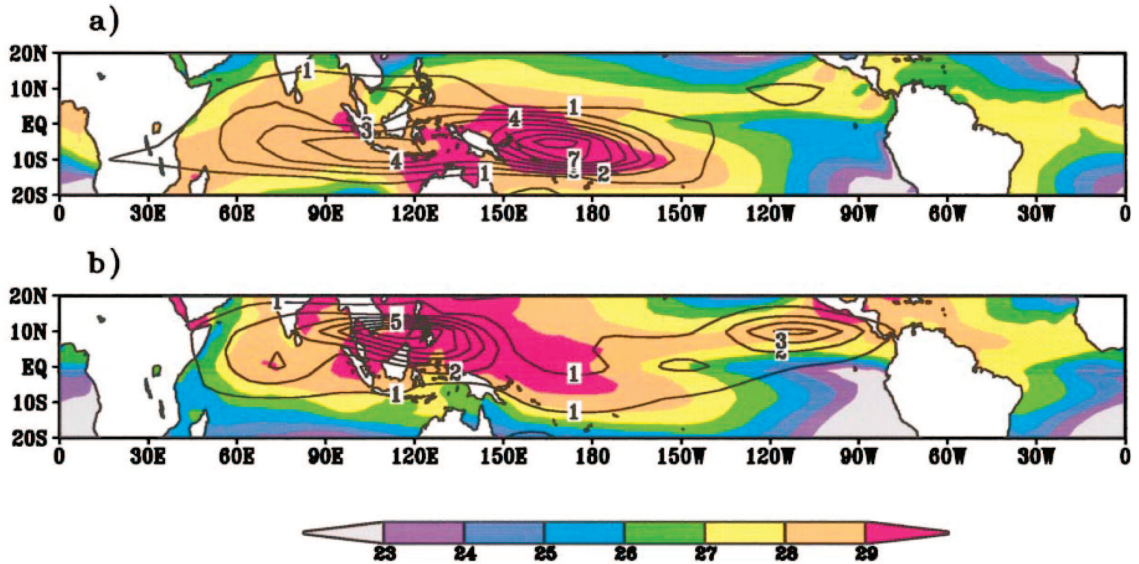


Figure 1.6: Reproduced from Zhang and Dong (2004). Zonal wind variance ($\text{m}^2 \text{s}^{-2}$, contours) at 850 hPa and mean SST ($^{\circ}\text{C}$, colors) averaged over (a) Dec–Mar and (b) Jun–Sep. Note the maximum zonal wind variance and SST during the northern hemisphere winter are in phase between 5° – 10°S , and are in phase between 5° – 10°N during the northern hemisphere summer. The stronger zonal wind variance signal during the northern hemisphere winter is also seen.

Pacific ocean than in the Indian ocean. Though it is tempting, Zhang and Dong warn against interpreting this seasonal migration as simply due to the seasonality of the sea surface temperatures (SST). One reason to believe it is more complex is that even though the MJO migration is in phase with the SST, their amplitudes do not match.

While complex models have some degree of success producing intraseasonal oscillations, understanding why can be difficult. Stripping away some of the complicated details by opting for a simplified theoretical model has helped in elucidating some of the basic dynamical concepts. The observed Rossby-Kelvin flow response associated with an MJO convective region hints at the usefulness of linear equatorial wave theory (Matsuno, 1966), which has formed the basis for investigating many tropical convection related phenomena (the MJO included). The “long-wave approximation” to the shallow water equatorial β -plane equations has been successful in producing analytical solutions for steady-state (Gill, 1980) and time-dependent (Heckley and Gill, 1984) localized diabatic forcing. Chao (1987)

considered the MJO using the “long-wave approximation” to the equatorial β -plane equations with a first internal baroclinic mode vertical structure, forced by a zonally propagating diabatic source. In solving the equatorial β -plane equations without introducing the “long-wave approximation” (Schubert and Masarik, 2006), chapter 2 of this research can be seen as the primitive equation generalization to Chao’s study.

Though not as manageable as linear systems, non-linear models can capture some of the richer detail which simpler frameworks are not capable of. This point is seen in research by Harris (1999), who uses a non-linear global shallow water model to study the effect of tropical convection on the large-scale atmosphere. Of particular interest to this research is a result regarding the dependence of Kelvin wave strength on the time-scale of forcing. By running simulations with different forcing time scales, the Kelvin and Rossby wave responses were seen to get stronger as the forcing time-scale became shorter. This was true down to a limit of approximately 2-3 days, at which point the response became dominated by gravity waves. When the forcing exists on this time scale, and is of large magnitude (“explosive” large-scale tropical convection), the Kelvin response is maximized and could influence the surrounding atmosphere as to trigger an MJO event. More specifically, if convection in the Indian Ocean became intense but short-lived, a strong Kelvin response could result, which could then couple with the convection and propagate eastward. Assuming this disturbance maintained a strong convective core which supported a Rossby response as well, this could be a potential mechanism (convectively-coupled Kelvin wave induced) for initiation of an MJO event.

Continuing upward in model sophistication, GCMs (general circulation model) are near the top due to their global scale, increasingly finer resolutions, and length of simulations. The state of GCM skill in producing intraseasonal oscillations is documented by Slingo et al. (1996), who reported the results from a subproject of AMIP (Atmospheric Model Intercomparison Project) focusing on the ability of 15 AGCMs (atmospheric general circulation model) to simulate the MJO. This was achieved by comparison of velocity po-

tential (χ) time-longitude data from the 15 models, with χ data compiled from European Centre for Medium-range Weather Forecasts (ECMWF) analysis (not reproduced here). Time-longitude diagrams of χ from the 15 models (2 realizations of the ECMWF model) are displayed in Fig. 1.7, in which the characteristics discussed below can be seen. The findings of this study can be summarized as follows: The models involved exhibited a wide range of skill in simulating the MJO. In terms of propagation direction alone, most models produced an eastward propagating χ anomaly, though some tended toward a standing oscillation, and at least one gave a chaotic field with no preference of propagation direction. Of the models that did produce a definite eastward propagating signal, the associated periodicities were reasonable though they tended to be shorter (25–30 days) than the analysis (40–50 days). Most models underestimated the strength of the signal, with the exception of GLA, NCAR, RPN, and UKMO. Most of the models were unable to capture the seasonality (Zhang and Dong, 2004) inherent to the MJO, with the exception of GLA, RPN, UKMO. None of the models produced a distinctive change in phase speed near the dateline as did the analysis (from 6 ms^{-1} to 16 ms^{-1} , due to the effect of convective decoupling from the Kelvin wave response). The conclusion is that among the models surveyed, a wide range of skill existed from complete inability, to reasonable resolution of several key features. Thus, while some models do exhibit a level of skill in simulating portions of an MJO, all contained significant deficiencies that need to be resolved before being able to claim simulation of an MJO “event”.

Analogous to GCM’s, theoretical work involving the MJO has had some degree of success, but still has deficiencies. To date, no theory has been given that adequately (completely) describes the MJO. It is likely though that some existing theory, or combinations thereof, explain aspects of the MJO. Many of the theories can be grouped under one of three types: (1) wave-CISK (Conditional Instability of the Second Kind) is based on the idea that the interaction between the Kelvin wave and the convection it is coupled to determine the eastward propagation of the MJO (Lau and Peng, 1987).

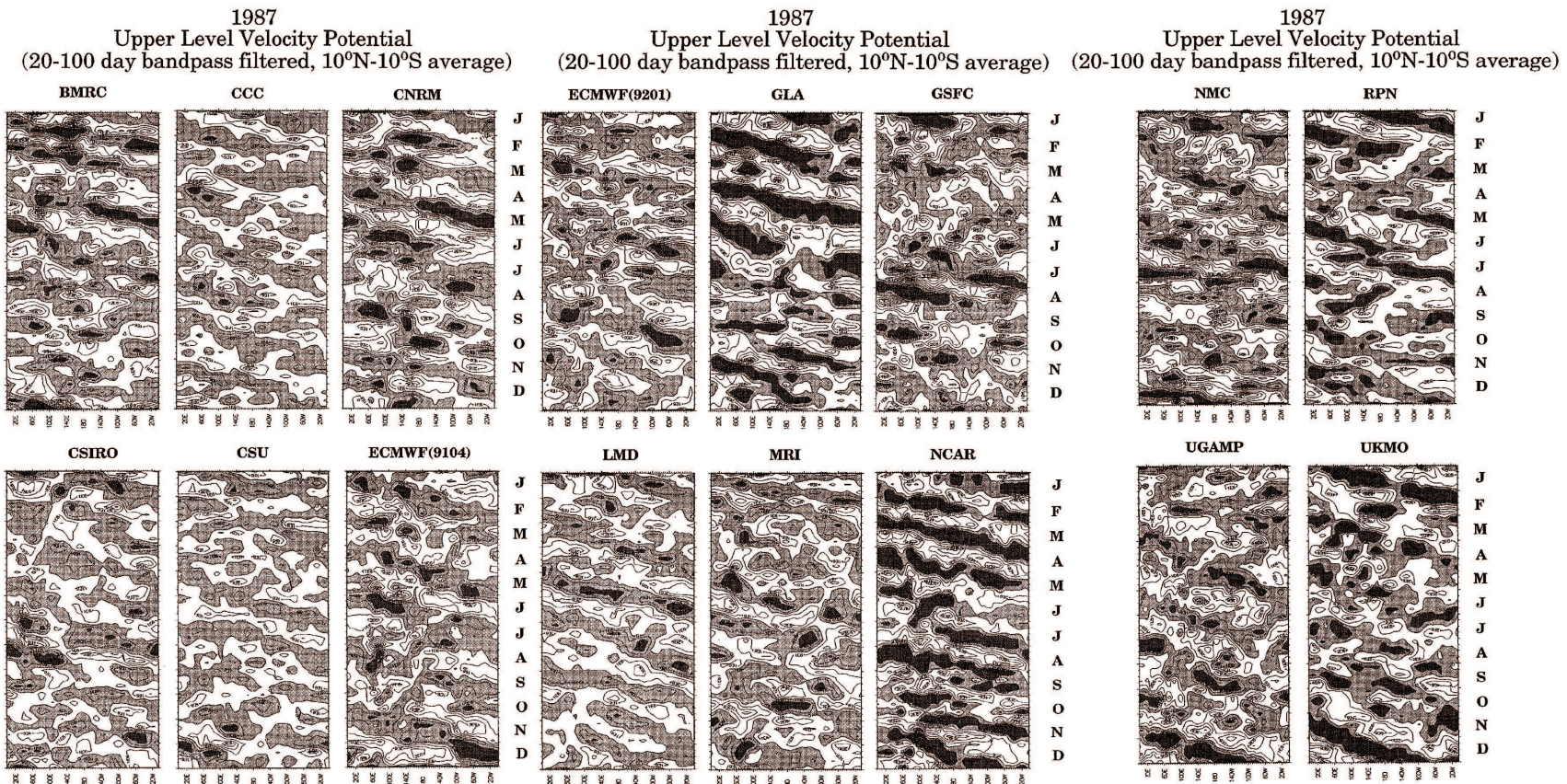


Figure 1.7: Reproduced from Slingo et al. (1996). Time-longitude diagrams for 1987 of the 20–100 day filtered velocity potential (χ) at 200 hPa (300 hPa for CCC), averaged between 10°N and 10°S , from the participating models. The model (institute) acronym is displayed above each diagram. Time increases downward. The contour interval is $1 \times 10^6 \text{ m}^2 \text{ s}^{-1}$ for all models except GLA, NCAR, RPN, and UKMO where it is $2 \times 10^6 \text{ m}^2 \text{ s}^{-1}$. Negative values are shaded.

The main problem with this theory is reconciling the observed phase speed with the required vertical scale. (2) WISHE (Wind-Induced Surface Heat Exchange) theory states that the waves which compose the MJO result from instability which is derived from the latent heat flux produced from wind-induced evaporation (Emanuel, 1987). A key problem with this is the assumption that the mean surface winds are easterlies, though the observed mean winds in the equatorial Indian and western Pacific oceans are westerlies. (3) Discharge-Recharge (Hu and Randall, 1994) proposes that non-linear interactions between radiation, cumulus convection, and surface moisture flux allow a stationary forcing which can periodically trigger MJO events. The time scale of the oscillation is thus determined by the time involved with drying of the atmosphere as an MJO event passes (“discharge”), and then the time required for the above mechanisms to remoisten the atmosphere so that it is primed for the next event (“recharge”). More detail on each of these theories can be found in Wang (2005).

As mentioned, it was only possible to cover a small portion of the extensive literature related to the MJO. The following reviews are suggested to learn more about the aspects introduced, and those which were not able to be included. An overview of the first 20 years of observational studies is presented by Madden and Julian (1994). A more recent paper, Zhang (2005), gives a concise survey of MJO topics including theoretical and modeling approaches. For a detailed treatment of intraseasonal variability (ISV) see Lau and Waliser (2005), in which each chapter is devoted to a particular aspect and the relevant literature has been reviewed by an authority in that area.

Lastly, two new papers utilizing up-to-date technology and data are listed. Preliminary results from an icosahedral-grid cloud-resolving AGCM (atmospheric general circulation model) are reported in Tomita et al. (2005), where simulations using 7 km and 3.5 km grid intervals produce an intraseasonal oscillation similar to the MJO. An analysis of the MJO using rainfall data from the TRMM satellite (Tropical Rainfall Measuring Mission) is presented in Benedict and Randall (2007).

1.3 Overview

Since its discovery 35 years ago much has been learned about the MJO, though in spite of the ample literature it has inspired, a satisfactory theory explaining it is elusive. This may not be surprising considering the complexities involved with a phenomenon that exists on an intraseasonal time scale, and across all spatial scales. With this in mind, a good approach may be to attack one piece of the puzzle rather than trying to solve the whole problem at once. We proceed by looking at an aspect of the MJO that has not been sufficiently explored—the extent to which the flow in the wake of the convective envelope can be interpreted as balanced and derivable from the potential vorticity (PV) field (Schubert and Masarik, 2006).

The motivation for this approach is as follows. Balanced theories, such as quasi-geostrophic theory and semi-geostrophic theory, provide a foundation for understanding the dynamics of midlatitude weather systems. These theories are more tractable than the primitive equations and can be succinctly expressed as two equations—a prognostic equation for the material conservation of potential vorticity, and a diagnostic equation (or invertibility principle) relating the potential vorticity to the streamfunction. In many tropical weather systems, such as the ITCZ and tropical cyclones, the release of latent heat plays a crucial role, so that potential vorticity is not materially conserved. However, even in these cases, a useful strategy is to formulate a balanced model that predicts the potential vorticity and then inverts it to find the associated balanced wind and mass fields. This approach has yielded insights into the dynamics of ITCZ breakdown and the formation of easterly waves (e.g., Schubert et al., 1991) and into the extreme PV structures that evolve in tropical cyclones (e.g., Hausman et al., 2006). What about large-scale weather systems that occur on the equator, such as the MJO? Are the concepts of balance and invertibility useful in understanding the essential dynamics of the MJO? Here we attempt to answer this question in the simplest context, i.e., in the context of a linearized equatorial β -plane model.

In the next chapter this simple theoretical model is used to explore the flow field

surrounding an eastward propagating forcing that is prescribed to coarsely resemble an MJO convective core. Analytical solutions are found and decomposed into equatorial wave components.

In chapter 3, the potential vorticity associated with the primitive equation model is calculated and a PV principle is derived. By considering an idealized version of the PV principle, a ratio which determines the magnitude of the PV anomaly is discovered. An invertibility principle is proposed based on an equatorial balance relation which allows us to invert the primitive equation PV.

Chapter 4 looks at the energy associated with the primitive equation solutions. We first derive a total energy principle, and then an associated Parseval relation. The Parseval relation allows computation of the total energy via spectral sums which has the advantage of being easier to calculate than a physical space integral, as well as the ability to partition the energy among the equatorial wave types. Lastly, the dependence of the response energy on the forcing parameters is studied using the Parseval relation.

Chapter 2

PRIMITIVE EQUATION MODEL

2.1 Governing Equations

The model used in this study is admittedly simple, though we believe for the expressed goals it is quite appropriate. Before proceeding, some brief physical considerations regarding the MJO are given to argue the models suitability.

The MJO is normally found in a narrow band about the equator ($\sim 10^{\circ}\text{S}, 10^{\circ}\text{N}$) so using an equatorial β -plane to approximate this region is very reasonable. The observed horizontal circulation patterns are $O(10,000 \text{ km})$, making the quasi-static approximation well-founded. Latent heating effects due to water vapor in the atmosphere are especially important in the tropics. While they most certainly play an important role in the evolution of this tropical weather system, the essential large scale features, which are of concern here, should be satisfactorily resolved without including a detailed moisture budget, but rather by simply including a specified diabatic heating. Based on these judgements, the equatorial β -plane quasi-static primitive equations are a legitimate theoretical framework. These are listed as the set (2.1)–(2.5),

$$\frac{Du}{Dt} - \beta yv + \frac{1}{\rho} \frac{\partial p}{\partial x} = F_x, \quad (2.1)$$

$$\frac{Dv}{Dt} + \beta yu + \frac{1}{\rho} \frac{\partial p}{\partial y} = F_y, \quad (2.2)$$

$$\frac{1}{\rho} \frac{\partial p}{\partial z} + g = 0, \quad (2.3)$$

$$\frac{\partial \rho}{\partial t} + \nabla \cdot (\rho \mathbf{V}) = 0, \quad (2.4)$$

$$c_p \frac{DT}{Dt} - \frac{1}{\rho} \frac{Dp}{Dt} = \mathcal{D}. \quad (2.5)$$

For a stratified, compressible atmosphere the standard forms of the hydrostatic and continuity equations are given by (2.3) and (2.4) respectively. The horizontal momentum equations (2.1), (2.2) have frictional forcing terms F_x and F_y . The last equation, the first law of thermodynamics, has a forcing term (\mathcal{D}) that accounts for all diabatic effects.

For convenience we choose to use the vertical log-pressure coordinate, $z = \ln(p_0/p)$, where $p_0 = 1010$ hPa is a constant “surface” pressure. Conversion of equations (2.1)–(2.4) to this vertical coordinate is the topic of Appendix A. Restricting our attention to small amplitude disturbances that arise from perturbing a resting basic state, we reach the following form of the governing equations,

$$\begin{aligned} \frac{\partial u}{\partial t} - \beta y v + \frac{\partial \phi}{\partial x} &= -\alpha u, \\ \frac{\partial v}{\partial t} + \beta y u + \frac{\partial \phi}{\partial y} &= -\alpha v, \\ \frac{\partial \phi}{\partial z} &= RT, \\ \frac{\partial u}{\partial x} + \frac{\partial v}{\partial y} + \frac{\partial w}{\partial z} - w &= 0, \\ \frac{\partial T}{\partial t} + \Gamma w &= -\alpha T + \frac{Q}{c_p}, \end{aligned} \quad (2.6)$$

where u is the eastward component of velocity, v the northward component, $w = Dz/Dt$ the “vertical log-pressure velocity,” ϕ the perturbation geopotential, T the perturbation temperature, $\beta = 2\Omega/a$ the equatorial value of the northward gradient of the Coriolis parameter, Ω the Earth’s rotation rate, a the Earth’s radius, α the constant coefficient for Rayleigh friction and Newtonian cooling. We have assumed the frictional dissipation, F_x , F_y , takes the form, $-\alpha u$, $-\alpha v$, respectively. The total diabatic effect term, \mathcal{D} , has been partitioned into dissipation due to radiative cooling, $-\alpha T$, and generation due to convective heating, Q/c_p . The basic state static stability, $\Gamma = d\bar{T}/dz + \kappa\bar{T}$ ($\kappa = R/c_p$), is computed from the basic state temperature profile, $\bar{T}(z)$. For simplicity we assume that Γ is a constant, and choose the tropical tropospheric mean value $\Gamma = 23.79$ K. We seek solutions of (2.6) on a domain that is infinite in y , periodic over $-\pi a \leq x \leq \pi a$, and confined between $z = 0$ and $z = z_T = \ln(1010/200) \approx 1.619$, with the boundary conditions $w = 0$ at $z = 0, z_T$.

2.2 Separation of Horizontal and Vertical Structure

Our first step in solving the governing equations is to separate off the vertical structure. This is done by performing a vertical normal mode transform on equations (2.6). Appendix B details this process by following the treatment in Fulton and Schubert (1985), which results in the variables taking the following series forms,

$$\begin{pmatrix} u(x, y, z, t) \\ v(x, y, z, t) \\ \phi(x, y, z, t) \end{pmatrix} = \sum_{\ell=1}^{\infty} \begin{pmatrix} u_{\ell}(x, y, t) \\ v_{\ell}(x, y, t) \\ \phi_{\ell}(x, y, t) \end{pmatrix} Z_{\ell}(z), \quad \begin{pmatrix} T(x, y, z, t) \\ w(x, y, z, t) \\ Q(x, y, z, t) \end{pmatrix} = \sum_{\ell=1}^{\infty} \begin{pmatrix} T_{\ell}(x, y, t) \\ w_{\ell}(x, y, t) \\ Q_{\ell}(x, y, t) \end{pmatrix} Z'_{\ell}(z), \quad (2.7)$$

where the orthogonal functions $Z_{\ell}(z)$ and their derivatives $Z'_{\ell}(z) = (d/dz)Z_{\ell}(z)$ compose the vertical structure. The specific form of the vertical modes can be found by solving the Sturm-Liouville problem

$$\left(\frac{d}{dz} - 1 \right) \frac{d}{dz} Z_{\ell}(z) = - \left(\frac{\ell^2 \pi^2}{z_T^2} + \frac{1}{4} \right) Z_{\ell}(z), \quad (2.8)$$

$$Z'_{\ell}(0) = Z'_{\ell}(z_T) = 0, \quad (2.9)$$

which arose from imposed conditions during the separation process. The separation constants \bar{c}_{ℓ}^2 turn out to be the square of the internal pure gravity wave phase speeds corresponding to the vertical internal modes $\ell = 1, 2, \dots$ and are defined as

$$\frac{R\Gamma}{\bar{c}_{\ell}^2} = \left(\frac{\ell^2 \pi^2}{z_T^2} + \frac{1}{4} \right)$$

The first internal vertical mode $Z_1(z)$ and its derivative $Z'_1(z)$ can be written in normalized form as

$$Z_1(z) = \left(\frac{\pi^2}{z_T^2} + \frac{1}{4} \right)^{-\frac{1}{2}} e^{(z-z_m)/2} \left[\frac{z_T}{2\pi} \sin \left(\frac{\pi z}{z_T} \right) - \cos \left(\frac{\pi z}{z_T} \right) \right], \quad (2.10)$$

and

$$Z'_1(z) = \left(1 + \frac{z_T^2}{4\pi^2} \right)^{\frac{1}{2}} e^{(z-z_m)/2} \sin \left(\frac{\pi z}{z_T} \right), \quad (2.11)$$

where z_m , the level at which $Z'_1(z)$ reaches its maximum value, is given by $\pi z_m/z_T = \pi + \tan^{-1}(-2\pi/z_T)$, which, for $z_T \approx 1.619$, turns out to be $z_m \approx 0.5803z_T$. For later

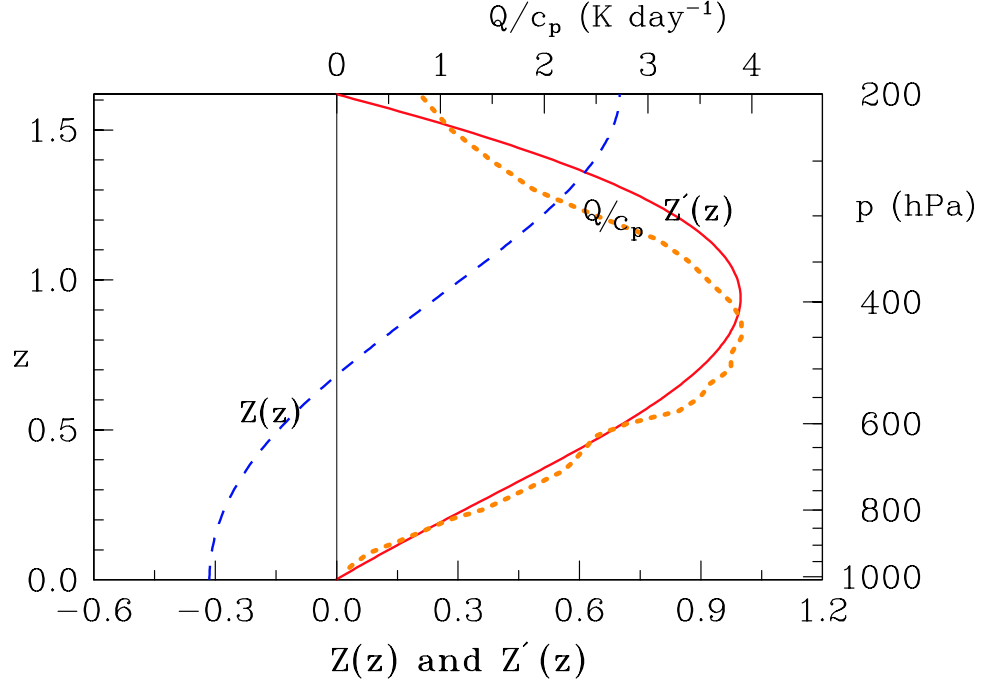


Figure 2.1: The curves labeled $Z(z)$ (blue,dashed) and $Z'(z)$ (red,solid)—interpreted using the lower scale—are the vertical structure functions defined by (2.10) and (2.11). The curve labeled Q/c_p (orange,dotted)—interpreted using the upper scale—is the 120-day mean vertical profile of heating rate for the western Pacific warm pool, as determined by Johnson and Ciesielski (2000). Note that $Z'(z)$ reaches its maximum at $p \approx 395$ hPa.

convenience, the normalization chosen in (2.10) and (2.11) yields $Z'_1(z_m) = 1$. Relabeling these functions to be $Z(z) \equiv Z_1(z)$ and $Z'(z) \equiv Z'_1(z)$, their plots are shown in Fig. 2.1. Also shown in Fig. 2.1 is the 120-day mean (November 1992 – February 1993) vertical profile of the heating rate for the western Pacific warm pool (Johnson and Ciesielski, 2000). The observed mean profile of Q/c_p has a peak value of approximately 4 K day^{-1} , and its shape is closely approximated by $Z'(z)$, the vertical structure of our constructed Q/c_p . Based on this good approximation we make the simplifying assumption that the heating excites only the first vertical internal mode. In doing so, the infinite series is truncated to this single mode. The variable expressions in (2.7) can then be rewritten as

$$\begin{pmatrix} u(x, y, z, t) \\ v(x, y, z, t) \\ \phi(x, y, z, t) \end{pmatrix} = \begin{pmatrix} \hat{u}(x, y, t) \\ \hat{v}(x, y, t) \\ \hat{\phi}(x, y, t) \end{pmatrix} Z(z), \quad \begin{pmatrix} T(x, y, z, t) \\ w(x, y, z, t) \\ Q(x, y, z, t) \end{pmatrix} = \begin{pmatrix} \hat{T}(x, y, t) \\ \hat{w}(x, y, t) \\ \hat{Q}(x, y, t) \end{pmatrix} Z'(z), \quad (2.12)$$

where the $(\hat{\cdot})$'s on the transformed variables denote their lack of z -dependence. The gravity wave speed that corresponds to the first internal vertical mode is

$$\bar{c} \equiv \bar{c}_1 = \frac{(R\Gamma)^{1/2}}{\left[\frac{\pi^2}{z_T^2} + \frac{1}{4}\right]^{1/2}} \approx 41.25 \text{ m s}^{-1}. \quad (2.13)$$

Over the 120-day observational period there were two MJO passages (Lin and Johnson, 1996; Yanai et al., 2000). During these two periods of enhanced convection the shape of the vertical profile of Q/c_p was very similar to the shape of the time mean profile shown in Fig. 2.1, but the peak values were considerably larger, 10 K day^{-1} for the first MJO and 16 K day^{-1} for the second. Thus, for the vertical profile of heating at the time of peak convective activity during the passage of an MJO, our model uses the $Z'(z)$ profile shown in Fig. 2.1, but scaled so the peak value is 12 K day^{-1} (chosen as an intermediate value between the two MJO peak values) rather than 4 K day^{-1} . Assuming now that u, v, ϕ, T, w, Q have the separable forms given in (2.12) we can convert (2.6) into the following system for the horizontal structure functions $\hat{u}, \hat{v}, \hat{\phi}, \hat{T}, \hat{w}$:

$$\begin{aligned} \frac{\partial \hat{u}}{\partial t} - \beta y \hat{v} + \frac{\partial \hat{\phi}}{\partial x} &= -\alpha \hat{u}, \\ \frac{\partial \hat{v}}{\partial t} + \beta y \hat{u} + \frac{\partial \hat{\phi}}{\partial y} &= -\alpha \hat{v}, \\ \hat{\phi} &= R \hat{T}, \\ \frac{\partial \hat{u}}{\partial x} + \frac{\partial \hat{v}}{\partial y} - \left(\frac{\pi^2}{z_T^2} + \frac{1}{4}\right) \hat{w} &= 0, \\ \frac{\partial \hat{T}}{\partial t} + \Gamma \hat{w} &= -\alpha \hat{T} + \frac{\hat{Q}}{c_p}. \end{aligned} \quad (2.14)$$

In section 2.4 we present an analytical solution of (2.14). The solution can be considered as the primitive equation generalization of the simplest MJO model involving the first baroclinic mode response to a moving planetary scale heat source under the long wave approximation (Chao, 1987).

2.3 Model Diabatic Forcing

A limitation of using prescribed forcing is that the flow field cannot exert any influence on it. In other words, the forcing acts on the model atmosphere altering its structure, though the circulation that results is not able to communicate its new state back to the forcing. If feedback from the circulation does not significantly change the “net effect” of the forcing, then this interaction could be neglected in a first approximation when large-scale features are of interest. Under this rationale we proceed forward with a prescribed diabatic forcing designed to resolve the net effect from an ensemble of convective cloud complexes (a general upward transport of mass). Thus, the multi-scale structure described in section 1.2 will not be captured, which is consistent with regard to scale when circulation feedbacks are not present.

$c_p = 1004 \text{ J kg}^{-1} \text{ K}^{-1}$	$\beta = 2\Omega/a$	$\bar{c} = 41.25 \text{ m s}^{-1}$	$y_0 = 0 \text{ or } 450 \text{ km}$
$R = 287 \text{ J kg}^{-1} \text{ K}^{-1}$	$p_0 = 1010 \text{ hPa}$	$\epsilon = 507.3$	$Q_0/c_p = 12 \text{ K day}^{-1}$
$\Omega = 7.292 \times 10^{-5} \text{ s}^{-1}$	$z_T = 1.619$	$a_0 = 1250 \text{ km}$	$c = 5 \text{ m s}^{-1}$
$a = 6370 \text{ km}$	$\Gamma = 23.79 \text{ K}$	$b_0 = 450 \text{ km}$	$\alpha = (4 \text{ days})^{-1}$

Table 2.1: Constants.

Since the diabatic forcing is due to an eastward propagating region of deep convection, a suitable zonal structure is a sinusoid function of $x - ct$, where $c > 0$ is the constant propagation speed of the cloud cluster. The exact form of the horizontal structure is given by

$$\hat{Q}(x, y, t) = \frac{1}{2}Q_0 \exp \left[-\left(\frac{y-y_0}{b_0} \right)^2 \right] \begin{cases} 1 + \cos(\pi\xi/a_0) & |\xi| \leq a_0, \\ 0 & |\xi| \geq a_0, \end{cases} \quad (2.15)$$

$\xi = x - ct$, y_0 its center, a_0 its half-width in x , b_0 its e -folding width in y , and Q_0 its peak amplitude. The values chosen for these parameters are listed in Table 2.1. The choices for a_0 , b_0 , and y_0 were based on reanalysis studies discussed in section 1.2, the value for Q_0 was based on observations during TOGA-COARE, discussed in section 2.2. A plot of (2.15) with $Q_0 = 1 \text{ J kg}^{-1} \text{s}^{-1}$ is shown in Fig. 2.2. It is interesting to note that the area integral

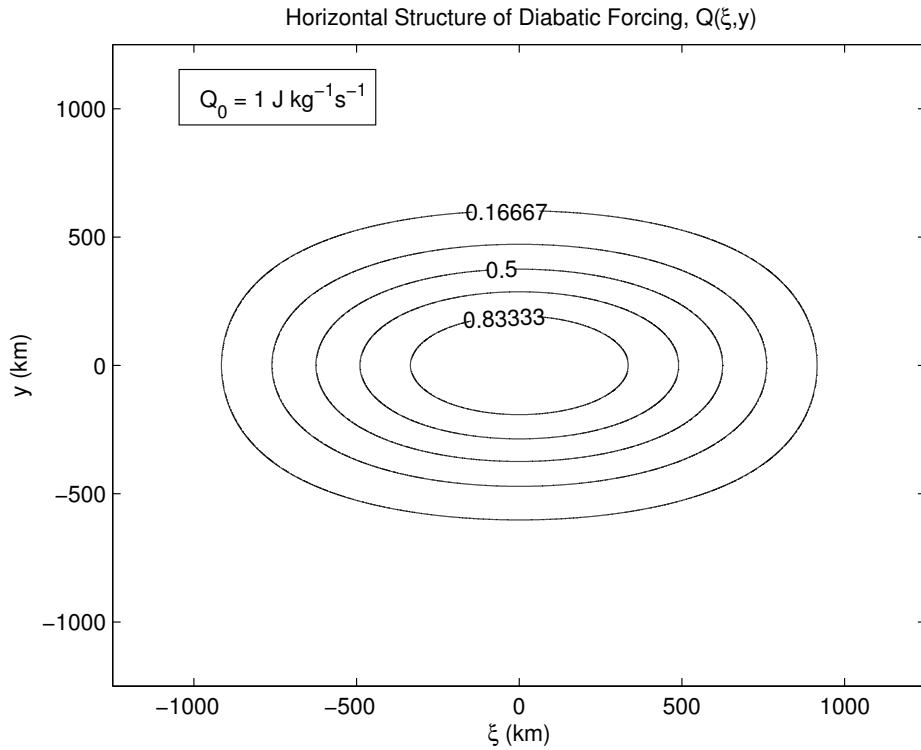


Figure 2.2: Contour plot of the diabatic forcing horizontal structure with Q_0 set to $1 \text{ J kg}^{-1}\text{s}^{-1}$.

of (2.15) yields $\iint \hat{Q}(\xi, y) dxdy = \pi^{\frac{1}{2}} Q_0 a_0 b_0$, so that our variation of the parameter y_0 has no effect on the total diabatic heating rate, $\pi^{\frac{1}{2}} Q_0 a_0 b_0$.

2.4 Horizontal Structure Problem

Our interest is in observing the flow field around the eastward moving constant source once all transient effects have ended. If we assume that it does reach a steady state, then viewing it from a reference frame that is moving at the same speed as the source would allow us to study the unchanging response pattern, versus watching the evolution of a particular region as the source passes through it. From this vantage point a change in time is proportional to a change in zonal position of the earth-relative steady state circulation. The shallow water equations (2.14) are converted to a system that is valid in this moving frame of reference by transforming both time and zonal derivatives to derivatives of the

“translating zonal distance coordinate” (ξ), introduced in the previous section. Making the replacements (see Appendix C for justification)

$$\frac{\partial}{\partial x} = \frac{\partial}{\partial \xi}, \quad (2.16)$$

$$\frac{\partial}{\partial t} = -c \frac{\partial}{\partial \xi}, \quad (2.17)$$

in (2.14) results in

$$\begin{aligned} -c \frac{\partial \hat{u}}{\partial \xi} - \beta y \hat{v} + \frac{\partial \hat{\phi}}{\partial \xi} &= -\alpha \hat{u}, \\ -c \frac{\partial \hat{v}}{\partial \xi} + \beta y \hat{u} + \frac{\partial \hat{\phi}}{\partial y} &= -\alpha \hat{v}, \\ \hat{\phi} &= R \hat{T}, \\ \frac{\partial \hat{u}}{\partial \xi} + \frac{\partial \hat{v}}{\partial y} - \left(\frac{\pi^2}{z_T^2} + \frac{1}{4} \right) \hat{w} &= 0, \\ -c \frac{\partial \hat{T}}{\partial \xi} + \Gamma \hat{w} &= -\alpha \hat{T} + \frac{\hat{Q}}{c_p}, \end{aligned} \quad (2.18)$$

reducing the number of independent variables from three to two. Next take the Fourier ξ -transform of the resulting system, defining, for example,

$$\hat{u}_m(y) = \frac{1}{2\pi a} \int_{-\pi a}^{\pi a} \hat{u}(\xi, y) e^{-im\xi/a} d\xi, \quad \hat{u}(\xi, y) = \sum_{m=-\infty}^{\infty} \hat{u}_m(y) e^{im\xi/a}, \quad (2.19)$$

where the integer m denotes the zonal wavenumber. Similar Fourier transform pairs exist for $\hat{v}_m(y)$, $\hat{\phi}_m(y)$, $\hat{T}_m(y)$, $\hat{w}_m(y)$, and $\hat{Q}_m(y)$. In this way, system (2.18) reduces to

$$\begin{aligned} \left(\alpha - \frac{imc}{a} \right) \hat{u}_m - \beta y \hat{v}_m + \frac{im}{a} \hat{\phi}_m &= 0, \\ \left(\alpha - \frac{imc}{a} \right) \hat{v}_m + \beta y \hat{u}_m + \frac{d\hat{\phi}_m}{dy} &= 0, \\ \left(\alpha - \frac{imc}{a} \right) \hat{\phi}_m + \bar{c}^2 \left(\frac{im}{a} \hat{u}_m + \frac{d\hat{v}_m}{dy} \right) &= \kappa \hat{Q}_m, \end{aligned} \quad (2.20)$$

after eliminating \hat{w}_m and \hat{T}_m by combining the hydrostatic, continuity, and thermodynamic equations. For each integer wavenumber m , (2.20) is a system of equations dependent only on meridional position. Once (2.20) has been solved for \hat{u}_m , \hat{v}_m , $\hat{\phi}_m$, the vertical velocity \hat{w}_m can be recovered from

$$\hat{w}_m = \left(\frac{\pi^2}{z_T^2} + \frac{1}{4} \right)^{-1} \left(\frac{im}{a} \hat{u}_m + \frac{d\hat{v}_m}{dy} \right). \quad (2.21)$$

The Fourier ξ -transform of $\hat{Q}(\xi, y)$, defined by (2.15), is given by

$$\hat{Q}_m(y) = (2\pi a)^{-1} \int_{-\pi a}^{\pi a} \hat{Q}(\xi, y) \exp(-im\xi/a) d\xi,$$

which is easily evaluated to yield

$$\hat{Q}_m(y) = \frac{\pi Q_0}{2[\pi^2 - (ma_0/a)^2]} \frac{\sin(ma_0/a)}{m} \exp\left[-\left(\frac{y-y_0}{b_0}\right)^2\right]. \quad (2.22)$$

We now write the system (2.20) in the convenient vector form ¹

$$\left(\alpha - \frac{imc}{a}\right) \hat{\eta}_m + \mathcal{L} \hat{\eta}_m = \kappa \hat{\mathbf{Q}}_m, \quad (2.23)$$

where

$$\mathcal{L} = \begin{pmatrix} 0 & -\beta y & im/a \\ \beta y & 0 & d/dy \\ \bar{c}^2 im/a & \bar{c}^2 d/dy & 0 \end{pmatrix}, \quad \hat{\eta}_m(y) = \begin{pmatrix} \hat{u}_m(y) \\ \hat{v}_m(y) \\ \hat{\phi}_m(y) \end{pmatrix}, \quad \hat{\mathbf{Q}}_m(y) = \begin{pmatrix} 0 \\ 0 \\ \hat{Q}_m(y) \end{pmatrix}. \quad (2.24)$$

The Fourier transformed equations (2.23) can be solved using a normal mode transform in the meridional direction. To accomplish this, first define the inner product

$$(\mathbf{f}, \mathbf{g}) = \int_{-\infty}^{\infty} \left(f_1 g_1^* + f_2 g_2^* + \frac{1}{\bar{c}^2} f_3 g_3^* \right) d\hat{y}, \quad (2.25)$$

where $\mathbf{f}(\hat{y})$ and $\mathbf{g}(\hat{y})$ are complex, three component vector functions of the dimensionless meridional coordinate $\hat{y} = (\beta/\bar{c})^{1/2} y = \epsilon^{1/4}(y/a)$, and where the $*$ symbol denotes the complex conjugate and $\epsilon = 4\Omega^2 a^2 / \bar{c}^2$ is Lamb's parameter. With $\bar{c} = 41.25 \text{ ms}^{-1}$ we obtain $\epsilon = 507.3$. The inner product (2.25), is suggested by the total energy principle (derived in section 4.1) associated with (2.23). The adjoint of \mathcal{L} , denoted by \mathcal{L}^\dagger and defined by $(\mathcal{L}\mathbf{f}, \mathbf{g}) = (\mathbf{f}, \mathcal{L}^\dagger \mathbf{g})$, is related to \mathcal{L} by $\mathcal{L}^\dagger = -\mathcal{L}$. In other words, the linear operator \mathcal{L} is skew-Hermitian with respect to the inner product (2.25). The skew-Hermitian property dictates that the eigenvalues of \mathcal{L} are pure imaginary and that the eigenfunctions form a complete

¹ The simplicity of the first term in (2.23) depends on the assumed equality for the damping rates associated with Rayleigh friction and Newtonian cooling. However, the derivation following (2.23) could easily be generalized to allow a 10–20 day radiative damping rate and a 3–5 day frictional damping rate (Lin et al., 2005).

(Wu and Moore, 2004), orthogonal set (as long as degeneracy does not occur). Denoting an eigenvalue by $i\nu_{mnr}$ and a corresponding eigenfunction by $\mathbf{K}_{mnr}(\hat{y})$, we have

$$\mathcal{L}\mathbf{K}_{mnr} = i\nu_{mnr}\mathbf{K}_{mnr}, \quad \text{with} \quad \mathbf{K}_{mnr}(\hat{y}) = \begin{pmatrix} U_{mnr}(\hat{y}) \\ V_{mnr}(\hat{y}) \\ \Phi_{mnr}(\hat{y}) \end{pmatrix}. \quad (2.26)$$

The eigenvalues of \mathcal{L} , which yield the dispersion relation for equatorially trapped waves,

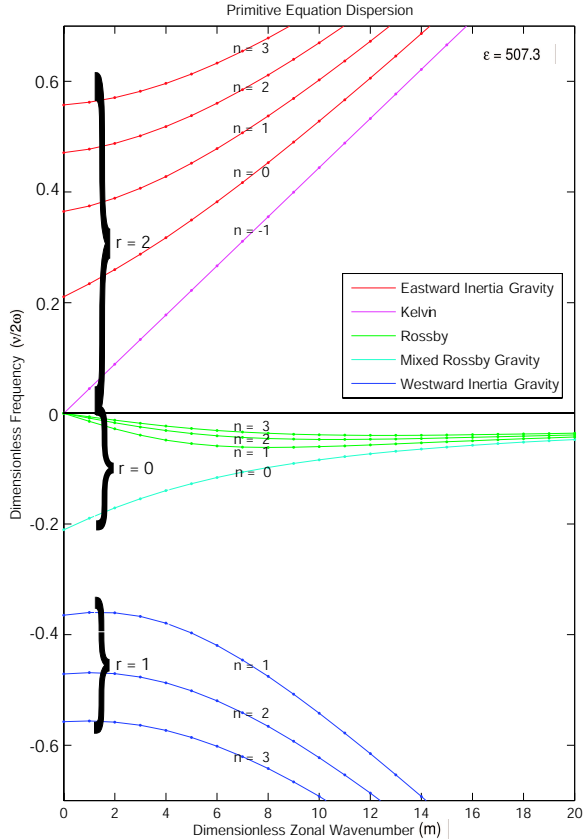


Figure 2.3: Dispersion diagram, $\hat{\nu}_{mnr}$ vs. m , for values $n = -1, 0, 1, 2, 3$ and $r = 0, 1, 2$.

satisfy the cubic equation (Matsuno, 1966)

$$\epsilon\hat{\nu}^2 - m^2 - \frac{m}{\hat{\nu}} = \epsilon^{\frac{1}{2}}(2n + 1), \quad (2.27)$$

where $n = 0, 1, 2, \dots$ is the index for the meridional mode and $\hat{\nu} = \nu/(2\Omega)$ is the dimensionless frequency. We let $r = 0, 1, 2$ be the index corresponding to the three roots of the

dispersion relation, so that the eigenfunctions and eigenvalues can be characterized by the triple index m, n, r . Special care is required for the case $n = 0$, for which (2.27) can be factored into $(\epsilon^{\frac{1}{2}}\hat{\nu} + m)(\epsilon^{\frac{1}{2}}\hat{\nu}^2 - m\hat{\nu} - 1) = 0$. The root $\epsilon^{\frac{1}{2}}\hat{\nu} = -m$ must be discarded because the corresponding eigenfunction is unbounded in \hat{y} . Thus, when $n = 0$, only the two solutions of $\epsilon^{\frac{1}{2}}\hat{\nu}^2 - m\hat{\nu} - 1 = 0$ are retained and are indexed by $r = 0$ (mixed Rossby-gravity wave) and $r = 2$ (eastward inertia-gravity wave). The eigenfunctions for Kelvin waves can be found separately by setting V_{mnr} to zero in (2.26). The Kelvin wave eigenvalues $\epsilon^{\frac{1}{2}}\hat{\nu} = m$ can be formally considered as a solution to (2.27) when $n = -1$. We index this solution as $r = 2$. Then, for given $n = -1, 0, 1, \dots$, $\mathbf{K}_{mnr}(\hat{y})$ is the eigenfunction corresponding to the eigenvalue ν_{mnr} . The form of $\mathbf{K}_{mnr}(\hat{y})$ is given by

$$\mathbf{K}_{mnr}(\hat{y}) = A_{mnr} \begin{pmatrix} \epsilon^{\frac{1}{4}} \left[\left(\epsilon^{\frac{1}{2}}\hat{\nu}_{mnr} + m \right) \left(\frac{n+1}{2} \right)^{\frac{1}{2}} \mathcal{H}_{n+1}(\hat{y}) + \left(\epsilon^{\frac{1}{2}}\hat{\nu}_{mnr} - m \right) \left(\frac{n}{2} \right)^{\frac{1}{2}} \mathcal{H}_{n-1}(\hat{y}) \right] \\ -i (\epsilon\hat{\nu}_{mnr}^2 - m^2) \mathcal{H}_n(\hat{y}) \\ \bar{\epsilon}\epsilon^{\frac{1}{4}} \left[\left(\epsilon^{\frac{1}{2}}\hat{\nu}_{mnr} + m \right) \left(\frac{n+1}{2} \right)^{\frac{1}{2}} \mathcal{H}_{n+1}(\hat{y}) - \left(\epsilon^{\frac{1}{2}}\hat{\nu}_{mnr} - m \right) \left(\frac{n}{2} \right)^{\frac{1}{2}} \mathcal{H}_{n-1}(\hat{y}) \right] \end{pmatrix}, \quad (2.28)$$

where the meridional structure functions $\mathcal{H}_n(\hat{y})$ ($n = 0, 1, 2, \dots$) are related to the Hermite polynomials $H_n(\hat{y})$ ($n = 0, 1, 2, \dots$) by ²

$$\mathcal{H}_n(\hat{y}) = \left(\pi^{\frac{1}{2}} 2^n n! \right)^{-\frac{1}{2}} H_n(\hat{y}) e^{-\frac{1}{2}\hat{y}^2}. \quad (2.29)$$

Since the Hermite polynomials satisfy the recurrence relation $\hat{y}H_n(\hat{y}) = \frac{1}{2}H_{n+1}(\hat{y}) + nH_{n-1}(\hat{y})$ and the derivative relation $dH_n(\hat{y})/d\hat{y} = 2nH_{n-1}(\hat{y})$, it is easily shown that the meridional structure functions $\mathcal{H}_n(\hat{y})$ satisfy the recurrence relation

$$\hat{y}\mathcal{H}_n(\hat{y}) = \left(\frac{n+1}{2} \right)^{\frac{1}{2}} \mathcal{H}_{n+1}(\hat{y}) + \left(\frac{n}{2} \right)^{\frac{1}{2}} \mathcal{H}_{n-1}(\hat{y}), \quad (2.30)$$

and the derivative relation

$$\frac{d\mathcal{H}_n(\hat{y})}{d\hat{y}} = - \left(\frac{n+1}{2} \right)^{\frac{1}{2}} \mathcal{H}_{n+1}(\hat{y}) + \left(\frac{n}{2} \right)^{\frac{1}{2}} \mathcal{H}_{n-1}(\hat{y}). \quad (2.31)$$

² The meridional structure functions \mathcal{H}_n are more convenient for our purposes than the parabolic cylinder functions D_n . The two functions are related by $\mathcal{H}_n(\hat{y}) = (\pi^{\frac{1}{2}} n!)^{-\frac{1}{2}} D_n(2^{\frac{1}{2}}\hat{y})$.

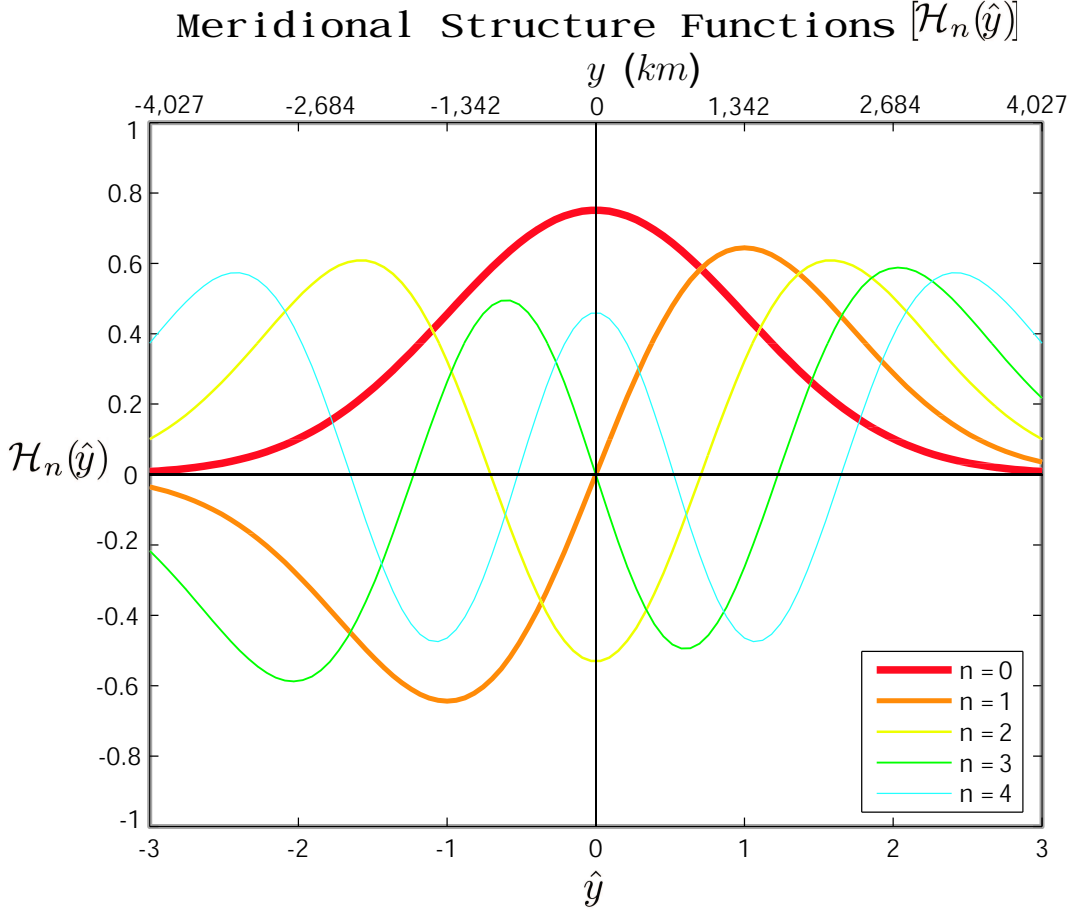


Figure 2.4: The meridional structure functions, $\mathcal{H}_n(\hat{y})$ for $n = 0, 1, 2, 3, 4$, are plotted over the equatorial band $\sim (35^\circ\text{S}, 35^\circ\text{N})$. The lower axis displays dimensionless meridional distance, $\hat{y} = \epsilon^{\frac{1}{4}}(y/a)$, and the upper axis displays the corresponding (integer) dimensional meridional distance, $y \text{ km}$.

The first two meridional structure functions are $\mathcal{H}_0(\hat{y}) = \pi^{-\frac{1}{4}} e^{-\frac{1}{2}\hat{y}^2}$ and $\mathcal{H}_1(\hat{y}) = 2^{\frac{1}{2}} \pi^{-\frac{1}{4}} \hat{y} e^{-\frac{1}{2}\hat{y}^2}$, from which all succeeding structure functions can be computed using the recurrence relation (2.30). Computing $\mathcal{H}_n(\hat{y})$ via its recurrence relation is much preferable to computing $H_n(\hat{y})$ via its recurrence relation and then computing $\mathcal{H}_n(\hat{y})$ by evaluation of the right hand side of (2.29), because the former method avoids explicit calculation of the factor $2^n n!$ for large n . Plots of $\mathcal{H}_n(\hat{y})$ for $n = 0, 1, 2, 3, 4$ are shown in Fig. 2.4. The normalization factor in (2.28) is given by

$$A_{mnr} = \left[\epsilon^{\frac{1}{2}}(n+1) \left(\epsilon^{\frac{1}{2}} \hat{\nu}_{mnr} + m \right)^2 + \epsilon^{\frac{1}{2}} n \left(\epsilon^{\frac{1}{2}} \hat{\nu}_{mnr} - m \right)^2 + (\epsilon \hat{\nu}_{mnr}^2 - m^2)^2 \right]^{-\frac{1}{2}} \quad (2.32)$$

for $n \geq 0$ and by

$$A_{m,-1,2} = 2^{-\frac{1}{2}}\pi^{-\frac{1}{4}} \quad (2.33)$$

for $n = -1$. These normalization factors result in the orthonormality property

$$\left(\mathbf{K}_{mnr}(\hat{y}), \mathbf{K}_{mn'r'}(\hat{y}) \right) = \begin{cases} 1 & (n', r') = (n, r) \\ 0 & (n', r') \neq (n, r). \end{cases} \quad (2.34)$$

The normality part of (2.34) is easily confirmed by substituting (2.28) into the left hand side and then using

$$\int_{-\infty}^{\infty} \mathcal{H}_n(\hat{y}) \mathcal{H}_{n'}(\hat{y}) d\hat{y} = \begin{cases} 1 & n' = n, \\ 0 & n' \neq n \end{cases} \quad (2.35)$$

to evaluate the three resulting integrals. It should be noted that there is a degeneracy for the zonally symmetric Rossby modes (i.e., for $m = 0, n > 0, r = 0$), in which case (2.28) is indeterminant because both m and $\hat{\nu}_{0n0}$ vanish. However, orthonormal eigenfunctions are easily constructed in this case, as discussed in Appendix D. Because of the orthonormality and completeness of the eigenfunctions $\mathbf{K}_{mnr}(\hat{y})$, we can set up the transform pair (Silva Dias et al., 1983; DeMaria, 1985)

$$\hat{\eta}_{mnr} = \left(\hat{\boldsymbol{\eta}}_m(\hat{y}), \mathbf{K}_{mnr}(\hat{y}) \right), \quad (2.36)$$

$$\hat{\boldsymbol{\eta}}_m(\hat{y}) = \sum_{n=-1}^{\infty} \sum_r \hat{\eta}_{mnr} \mathbf{K}_{mnr}(\hat{y}), \quad (2.37)$$

where $\hat{\eta}_{mnr}$ are the scalar coefficients in the normal mode expansion of the vector $\hat{\boldsymbol{\eta}}_m(\hat{y})$.

Note that (2.36) can be obtained by taking the inner product of (2.37) with $\mathbf{K}_{mn'r'}(\hat{y})$ and using the orthonormality property (2.34).

We now have the tools necessary to solve (2.23). Start by taking the inner product of (2.23) with the eigenfunction $\mathbf{K}_{mnr}(\hat{y})$,

$$\left(\left(\alpha - \frac{imc}{a} \right) \hat{\boldsymbol{\eta}}_m, \mathbf{K}_{mnr}(\hat{y}) \right) + (\mathcal{L}\hat{\boldsymbol{\eta}}_m, \mathbf{K}_{mnr}(\hat{y})) = \left(\kappa \hat{\mathbf{Q}}_m, \mathbf{K}_{mnr}(\hat{y}) \right),$$

next use the Skew-Hermitian property of \mathcal{L} ,

$$\left(\alpha - \frac{imc}{a} \right) (\hat{\boldsymbol{\eta}}_m, \mathbf{K}_{mnr}(\hat{y})) + (\hat{\boldsymbol{\eta}}_m, -\mathcal{L}\mathbf{K}_{mnr}(\hat{y})) = \kappa \left(\hat{\mathbf{Q}}_m, \mathbf{K}_{mnr}(\hat{y}) \right),$$

use the eigen-relation (2.26), (2.36), and the inner product $\hat{Q}_{mnr} = (\hat{\mathbf{Q}}_m, \mathbf{K}_{mnr})$,

$$\left(\alpha - \frac{imc}{a} \right) \hat{\eta}_{mnr} + i\nu_{mnr} (\hat{\boldsymbol{\eta}}_m, \mathbf{K}_{mnr}(\hat{y})) = \kappa \hat{Q}_{mnr},$$

finally,

$$\hat{\eta}_{mnr} = \frac{\kappa \hat{Q}_{mnr}}{\alpha + i(\nu_{mnr} - cm/a)}. \quad (2.38)$$

We have reduced the set of ordinary differential equations (2.23), to a decoupled system of algebraic equations (2.38), which can be solved independently for the values of $\hat{\eta}_{mnr}$. An expression for $(\hat{\mathbf{Q}}_m, \mathbf{K}_{mnr})$ is derived using the integral given in Appendix E. Using the result (E.1) twice, once with n replaced by $n+1$ and once with n replaced by $n-1$, we can write \hat{Q}_{mnr} as

$$\begin{aligned} \hat{Q}_{mnr} = & \frac{A_{mnr} \epsilon^{\frac{1}{2}} \pi Q_0 a_0 b_0}{2\bar{c}a^2 [\pi^2 - (ma_0/a)^2]} \frac{\sin(ma_0/a)}{(ma_0/a)} \left(\frac{2\pi}{2 + \hat{b}_0^2} \right)^{\frac{1}{2}} \exp \left(\frac{\hat{b}_0^2 \hat{y}_0^2}{4 - \hat{b}_0^4} \right) \\ & \cdot \left[(\epsilon^{\frac{1}{2}} \hat{\nu}_{mnr} + m) \left(\frac{2 - \hat{b}_0^2}{2 + \hat{b}_0^2} \right)^{\frac{n+1}{2}} \left(\frac{n+1}{2} \right)^{\frac{1}{2}} \mathcal{H}_{n+1} \left(\frac{2\hat{y}_0}{(4 - \hat{b}_0^4)^{\frac{1}{2}}} \right) \right. \\ & \left. - (\epsilon^{\frac{1}{2}} \hat{\nu}_{mnr} - m) \left(\frac{2 - \hat{b}_0^2}{2 + \hat{b}_0^2} \right)^{\frac{n-1}{2}} \left(\frac{n}{2} \right)^{\frac{1}{2}} \mathcal{H}_{n-1} \left(\frac{2\hat{y}_0}{(4 - \hat{b}_0^4)^{\frac{1}{2}}} \right) \right] \end{aligned} \quad (2.39)$$

for $n \geq 0$, and as

$$\hat{Q}_{mnr} = \frac{A_{mnr} \epsilon^{\frac{1}{4}} \pi Q_0 a_0 b_0}{2\bar{c}a^2 [\pi^2 - (ma_0/a)^2]} \frac{\sin(ma_0/a)}{(ma_0/a)} \left(\frac{2\pi}{2 + \hat{b}_0^2} \right)^{\frac{1}{2}} \exp \left(-\frac{\hat{y}_0^2}{2 + \hat{b}_0^2} \right). \quad (2.40)$$

for the Kelvin wave ($n = -1$, $r = 2$).

After $\hat{\eta}_{mnr}$ is computed from (2.38)–(2.40), the physical space fields u, v, ϕ can be recovered by making use of (2.37), followed by the inverse Fourier transform in ξ , i.e.,

$$\begin{pmatrix} u(\xi, y, z) \\ v(\xi, y, z) \\ \phi(\xi, y, z) \end{pmatrix} = Z(z) \sum_{m=-\infty}^{\infty} \sum_{n=-1}^{\infty} \sum_r \hat{\eta}_{mnr} \begin{pmatrix} U_{mnr}(\hat{y}) \\ V_{mnr}(\hat{y}) \\ \Phi_{mnr}(\hat{y}) \end{pmatrix} e^{im\xi/a}. \quad (2.41)$$

Using (2.21), (2.28) and (2.31) the physical space vertical log-pressure velocity can be recovered from

$$w(\xi, y, z) = \frac{Z'(z)}{R\Gamma} \sum_{m=-\infty}^{\infty} \sum_{n=-1}^{\infty} \sum_r i\nu_{mnr} \hat{\eta}_{mnr} \Phi_{mnr}(\hat{y}) e^{im\xi/a}. \quad (2.42)$$

For later use we note that the vertical log-pressure velocity $w = Dz/Dt$ is related to the vertical p -velocity $\omega = Dp/Dt$ by $\omega = -p_0 e^{-z} w$.

2.5 Solutions

All the model results shown in this section have been constructed by numerical evaluation of (2.41), and (2.42), which involves a superposition of zonal wavenumbers (sum over m), meridional wavenumbers (sum over n), and wave types (sum over r). In our examples the spectral coefficients $\hat{\eta}_{mnr}$ decay exponentially with n for all choices of m , which enables us to truncate the spectral solution at $n = N$ with a specified degree of accuracy. In general, $N = 200$ gives accurate results. Appendix F displays a flow chart outlining the procedure for computing the solutions.

Although the solutions have been computed over the entire zonal domain, only half the domain, centered on the forcing, is shown. This allows greater detail to be displayed for the region nearest the forcing. Using the parameters listed in Table 2.1, the 850 hPa wind and geopotential fields computed from (2.41) are shown in the top panel of Fig. 2.5 for $y_0 = 0$ and in the top panel of Fig. 2.7 for $y_0 = 450$ km. The choice of 850 hPa as the display level is arbitrary. According to the profile of $Z(z)$ shown in Fig. 2.1, upper tropospheric fields have the opposite sign and approximately twice the magnitude of the lower tropospheric fields. An interesting property of these simple linear solutions is that the lower tropospheric maximum westerly winds in the wake of the convective envelope are stronger than the lower tropospheric maximum easterly winds ahead of the convection. For example, in Fig. 2.5 the maximum 850 hPa westerly flow is 3.7 m s^{-1} while the maximum easterly flow is 1.6 m s^{-1} . In Fig. 2.7 the corresponding values are 4.2 m s^{-1} and 1.4 m s^{-1} . These wind speeds, the degree of asymmetry between westerlies and easterlies, and the larger zonal extent of the easterlies compared to the westerlies all agree well with the observed MJO composite ³

³ There is substantial variability in the cases that make up the MJO composite so that a detailed comparison of model results with an individual MJO case probably requires modeling the details of the diabatic forcing associated with that case.

(see Figs. 1.4 and 1.5) presented by Kiladis et al. (2005, Figs. 2 and 3). The remaining panels of Figs. 2.5 show the decomposition of the total fields into Rossby modes ($r = 0$ with $n \geq 1$), inertia-gravity modes ($r = 1, 2$ with $n \geq 1$ and $r = 2$ with $n = 0$), and Kelvin modes ($r = 2$ with $n = -1$). We have not plotted the contribution from mixed Rossby-gravity modes ($r = 0$ with $n = 0$) since it vanishes when $y_0 = 0$. The remaining panels in Fig. 2.7 show the same components as in Fig. 2.5, but also present is the mixed Rossby-gravity mode because it is nonzero when $y_0 \neq 0$. It should be noted that for small displacements off the equator the mixed Rossby-gravity response is negligible compared with the other components and was shown here only for completeness. The 395 hPa vertical motion field (recall that $Z'(z)$ reaches its maximum amplitude at $p \approx 395$ hPa) computed from (2.42) is shown in the top panel of Fig. 2.6 for $y_0 = 0$ and in the top panel of Fig. 2.8 for $y_0 = 450$ km. The other panels of Figs. 2.6 and 2.8 show the same components for the vertical motion field as were shown of the circulation in Figs. 2.5 and 2.7, respectively. These figures show that the vertical motion field is primarily composed of the Kelvin and inertia-gravity response as the Rossby vertical motion is very small for any value of y_0 , and the mixed-Rossby gravity response is identically zero on the equator, and relatively small otherwise.

Some notable features are apparent from Figs. 2.5–2.8. The total u, v, ϕ fields are composed of Rossby waves on the west side of the source, Kelvin waves on the east side, with “slaved” inertia-gravity waves providing low-level convergence near the source. As the center of the convective envelope is shifted north of the equator there is very little change in the response east of the forcing. In contrast, the response west of the forcing becomes biased to the northern hemisphere.

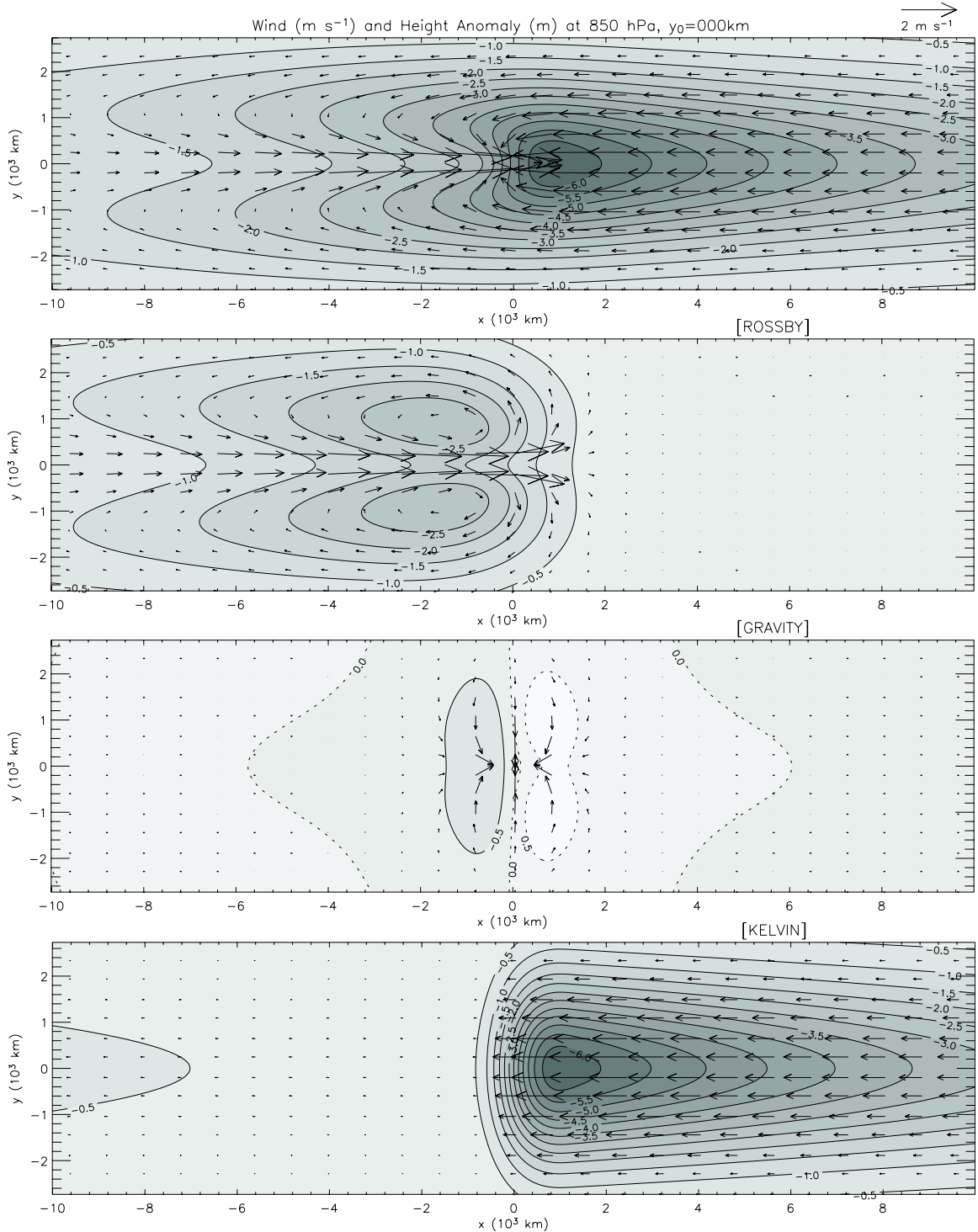


Figure 2.5: The upper panel shows the geopotential height anomaly and winds at 850 hPa for $y_0 = 0$ and for the remaining parameters listed in Table 2.1. The remaining three panels show respectively the contributions made by Rossby waves, inertia-gravity waves, and Kelvin waves.

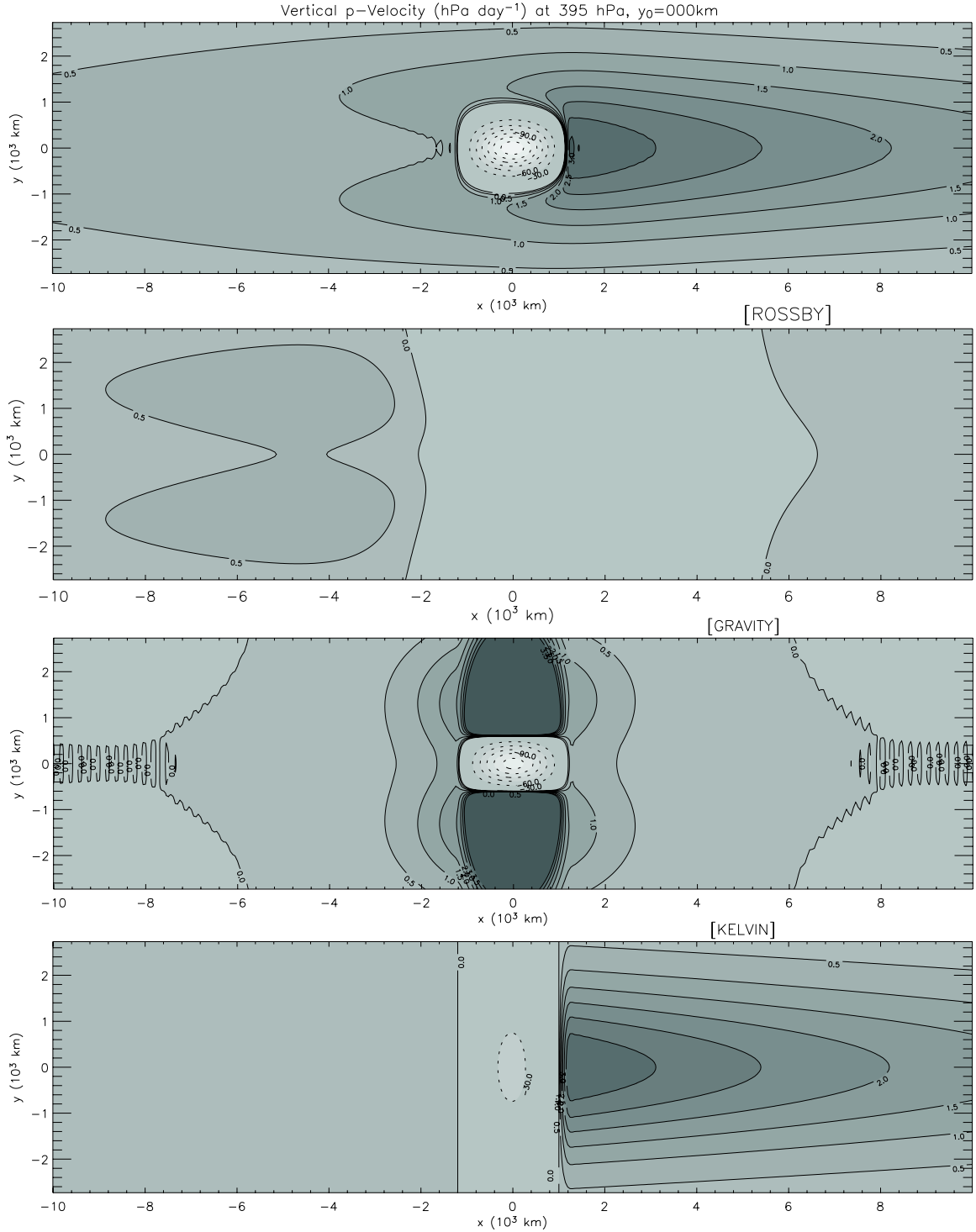


Figure 2.6: The first panel shows the vertical p -velocity, ω , at 395 hPa, with a contour interval of 30 hPa day^{-1} in the region of rising motion (dashed contours), and a contour interval of 0.5 hPa day^{-1} in the region of sinking motion (solid contours). The remaining panels show respective contributions of Rossby waves, inertia-gravity waves, and Kelvin waves to the vertical motion field. Results in this figure are for $y_0 = 0$.

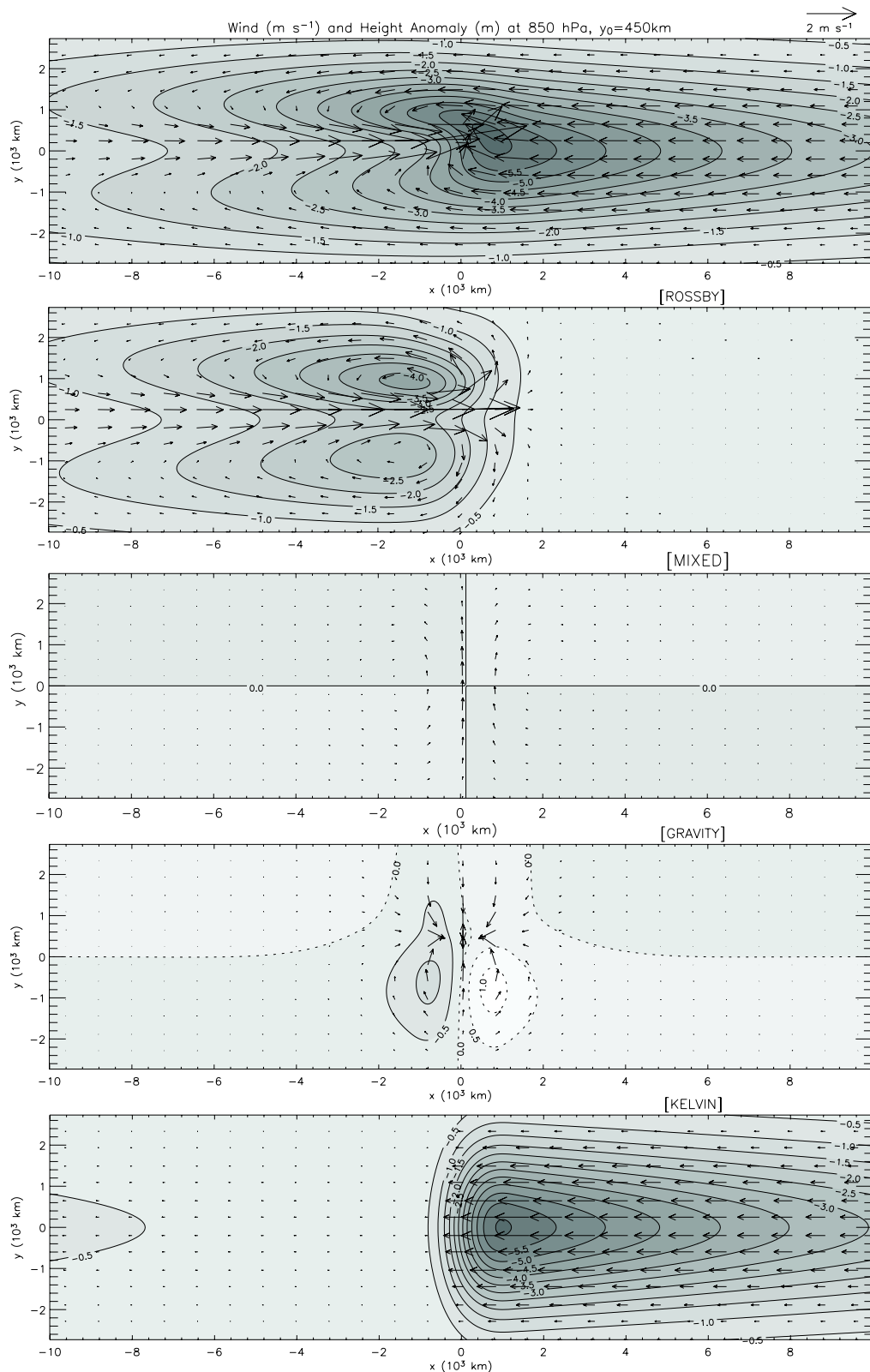


Figure 2.7: Same as Fig. 2.5, but the center of the convective forcing is shifted north of the equator ($y_0 = 450 \text{ km}$), so the nonzero mixed Rossby-gravity component is shown as well.

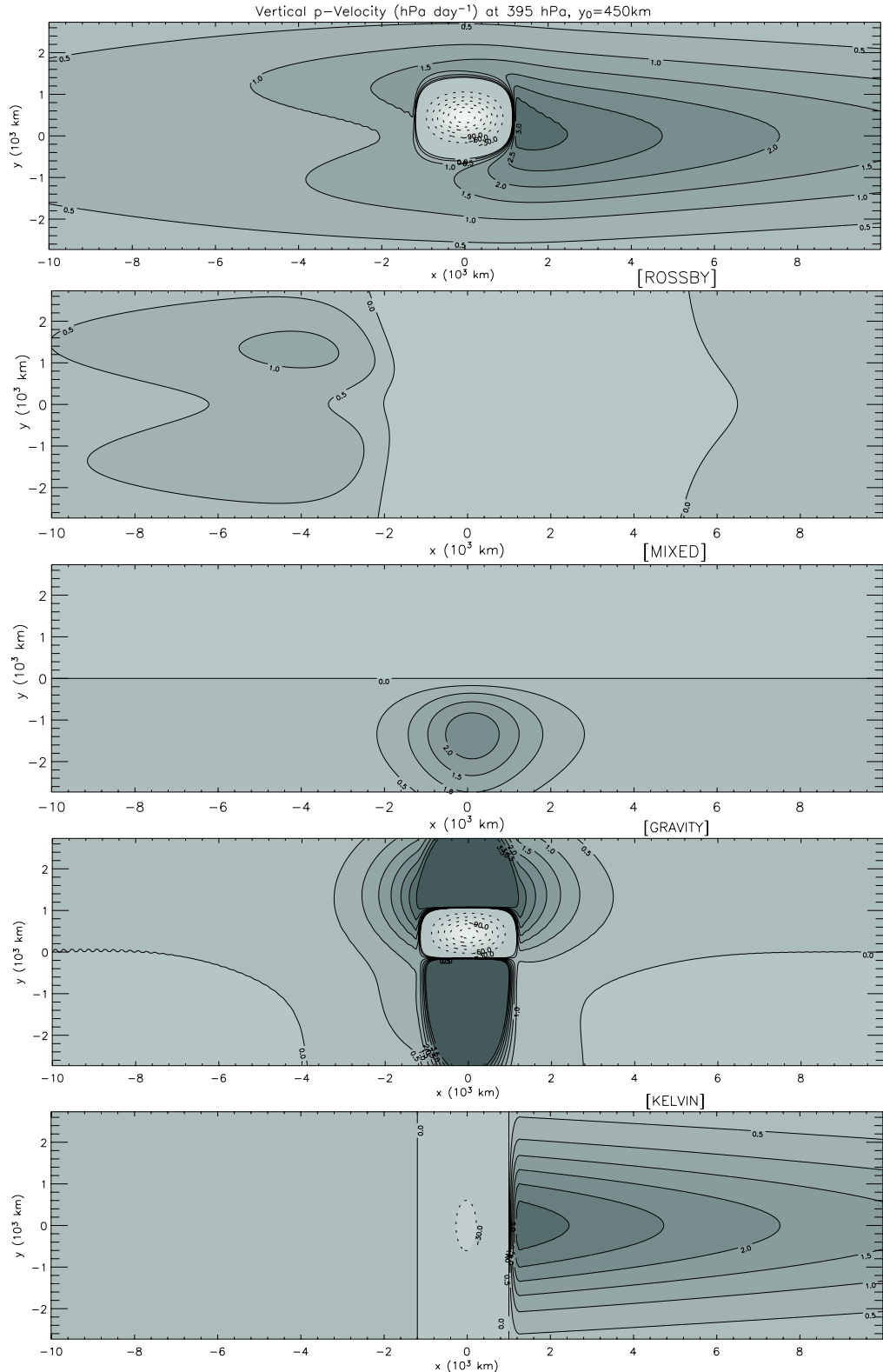


Figure 2.8: Same as Fig. 2.6, but the center of the convective forcing is shifted north of the equator ($y_0 = 450$ km), so the nonzero mixed Rossby-gravity component is shown as well.

Chapter 3

POTENTIAL VORTICITY ASPECTS

3.1 Primitive Equation Potential Vorticity

To derive the potential vorticity principle associated with (2.6) we first cross-differentiate the horizontal momentum equations to obtain the vorticity equation

$$\left(\frac{\partial}{\partial t} + \alpha \right) \left(\frac{\partial v}{\partial x} - \frac{\partial u}{\partial y} \right) + \beta y \left(\frac{\partial u}{\partial x} + \frac{\partial v}{\partial y} \right) + \beta v = 0, \quad (3.1)$$

and then combine the hydrostatic, continuity, and thermodynamic equations in such a way as to eliminate T and w , which results in

$$\left(\frac{\partial}{\partial t} + \alpha \right) \left(\frac{\partial}{\partial z} - 1 \right) \frac{\partial \phi}{\partial z} - R\Gamma \left(\frac{\partial u}{\partial x} + \frac{\partial v}{\partial y} \right) = \kappa \left(\frac{\partial}{\partial z} - 1 \right) Q. \quad (3.2)$$

Then, eliminating the horizontal divergence between (3.1) and (3.2) we obtain the potential vorticity principle

$$\frac{\partial q}{\partial t} + \beta v = -\alpha q + \frac{\beta y}{c_p \Gamma} \left(\frac{\partial}{\partial z} - 1 \right) Q, \quad (3.3)$$

where

$$q = \frac{\partial v}{\partial x} - \frac{\partial u}{\partial y} + \frac{\beta y}{R\Gamma} \left(\frac{\partial}{\partial z} - 1 \right) \frac{\partial \phi}{\partial z} \quad (3.4)$$

is the potential vorticity anomaly. From here it is an easy step to obtain the PV principle that is associated with the shallow water system (2.14). Refer back to the separable form (2.12) used in solving the primitive equation system in chapter 2. Using the variable expressions to separate off the vertical structure from (3.3) and (3.4), we arrive at the shallow water PV principle,

$$\frac{\partial \hat{q}}{\partial t} + \beta \hat{v} = -\alpha \hat{q} - \frac{\beta y}{\bar{c}^2} \kappa \hat{Q}, \quad (3.5)$$

where

$$\hat{q} = \frac{\partial \hat{v}}{\partial x} - \frac{\partial \hat{u}}{\partial y} - \frac{\beta y}{c^2} \hat{\phi} \quad (3.6)$$

is the shallow water PV anomaly. Following the general scheme used to solve the primitive equations, a spectral space series expression for PV can be derived. First perform a zonal Fourier transform (2.19) on (3.6), next use (2.37) to expand the variables in terms of meridional normal modes. The physical space PV can then be computed from its spectral components by

$$q(\xi, y, z) = Z(z) \sum_{m=-\infty}^{\infty} \sum_{n=-1}^{\infty} \sum_r \hat{q}_{mnr} \mathcal{H}_n(\hat{y}) e^{im\xi/a}, \quad (3.7)$$

where

$$\hat{q}_{mnr} = A_{mnr} \left(\frac{m^2 - \epsilon \hat{\nu}_{mnr}^2}{a \hat{\nu}_{mnr}} \right) \hat{\eta}_{mnr}. \quad (3.8)$$

According to (3.7) and (3.8), the physical space potential vorticity field is a superposition of the potential vorticity associated with all wave types except for the Kelvin wave. To see this recall that the Kelvin wave dispersion relation is $\epsilon^{\frac{1}{2}} \hat{\nu} = m$. Using this to evaluate the numerator in (3.8) we see that it is identically zero for all m , so the Kelvin wave contributes nothing to the sum. Although equatorial β -plane dynamics differ from midlatitude f -plane dynamics in the sense that inertia-gravity waves have zero potential vorticity on the midlatitude f -plane but not on the equatorial β -plane, the contribution of the equatorial β -plane inertia-gravity waves to the potential vorticity tends to be quite small. This is especially true for the higher zonal wavenumbers because for inertia-gravity waves $m^2 - \epsilon \hat{\nu}_{mnr}^2$ decreases and $|\hat{\nu}_{mnr}|$ increases as m increases. Recall that for $y_0 = 0$, the mixed Rossby-gravity wave is not excited. Even when it is excited ($y_0 \neq 0$), its contribution to the total circulation, and furthermore the PV, is small. It should be evident then that the total PV field is almost entirely due to the Rossby response, which is what we will use in what follows. It is interesting to interpret the flow patterns associated with the moving heat source in terms of a PV wake. For this interpretation the y -factor in the last term of (3.3) or (3.5) plays a crucial role. It causes the source term Q to be ineffective at generating a PV anomaly at the equator but maximizes the PV response near the poleward edges of the

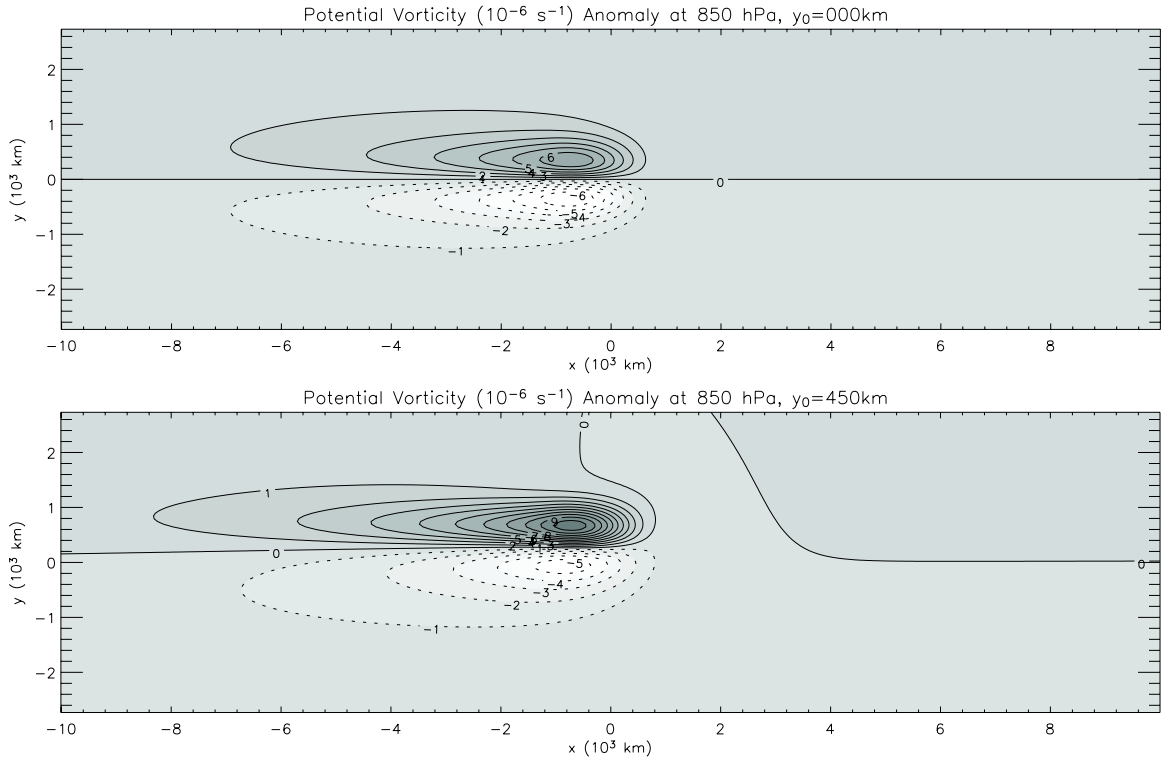


Figure 3.1: Both panels show the 850 hPa Rossby wave potential vorticity anomaly q , with a contour interval of $1 \times 10^{-6} \text{ s}^{-1}$. Top panel $y_0 = 0 \text{ km}$, bottom panel $y_0 = 450 \text{ km}$.

heat source. In this manner a moving equatorial heat source can produce two ribbons of lower tropospheric PV anomaly, a positive one off the equator in the northern hemisphere and a negative one off the equator in the southern hemisphere, with oppositely signed PV anomalies in the upper troposphere.

Examining the top panel of Fig. 3.1 and the second panel of Fig. 2.5, the PV anomaly patterns and the associated equatorial trough shear zones are zonally elongated because of the eastward movement of the convective envelope and the equatorward advection of the basic state PV in the wake of the convective envelope. As mentioned in section 2.5, shifting the center of convection north of the equator produces very little change in the response east of the forcing (compare last panel Figs. 2.5 and 2.7), yet the response west of the forcing (second panel Figs. 2.5, 2.7) becomes biased to the northern hemisphere. The behavior to the west of the forcing can be seen from the perspective of PV in Fig. 3.1. This plot shows the PV anomaly is nearly twice as strong in the northern hemisphere when $y_0 = 450 \text{ km}$.

3.2 Parameters Controlling PV Wake

Equation (3.3) states that q changes locally in time due to the Rossby term βv , the damping term $-\alpha q$, and the generation term $(c_p \Gamma)^{-1} \beta y (\partial/\partial z - 1) Q$. Insight into the importance of the βv term and into the critical parameters governing the PV wake can be obtained by calculating the hypothetical PV distribution that would result from forcing and dissipation only, i.e., the PV distribution resulting from the neglect of the Rossby term in (3.3). With the βv term neglected, and with the replacement $\partial/\partial t \rightarrow -c(\partial/\partial \xi)$, (3.3) reduces to

$$c \frac{\partial q}{\partial \xi} = \alpha q - \frac{\beta y}{c_p \Gamma} \left(\frac{\partial}{\partial z} - 1 \right) Q, \quad (3.9)$$

where Q is defined in (2.12) and (2.15). The solution of (3.9) is easily obtained (see Appendix G) and can be written in the form

$$q(\xi, y, z) = -\frac{\tau_p}{\tau_c} \left(\frac{\pi^2}{\pi^2 + \alpha^2 \tau_p^2} \right) F(\xi) \beta y \exp \left[-\left(\frac{y - y_0}{b_0} \right)^2 \right] Z(z), \quad (3.10)$$

where

$$F(\xi) = \begin{cases} \frac{\sinh[(\alpha/c)a_0]}{(\alpha/c)a_0} \exp [(\alpha/c)\xi] & -\infty < \xi \leq -a_0, \\ \frac{1 - \exp[-(\alpha/c)(a_0 - \xi)]}{2(\alpha/c)a_0} + \frac{\alpha a_0}{2\pi^2 c} [1 + \cos(\pi\xi/a_0)] - \frac{1}{2\pi} \sin(\pi\xi/a_0) & -a_0 \leq \xi \leq a_0, \\ 0 & a_0 \leq \xi < \infty. \end{cases} \quad (3.11)$$

In (3.10) the parameter $\tau_p = a_0/c$ is a measure of the passage time of the convective region and the parameter $\tau_c = \bar{c}^2/(\kappa Q_0)$ is a measure of the convective overturning time. A plot of (3.10) for $y_0 = 0$, with the remaining parameters listed in Table 2.1, is shown in the top panel of Fig. 3.2. This solution illustrates how a propagating convective region leaves in its wake two trailing PV strips on opposite sides of the equator. However, a comparison of the top and bottom panels of Fig. 3.2 shows that the neglect of βv results in a q field that has only 68% of the correct strength and does not extend far enough poleward or westward. The lower tropospheric meridional flow shown in Fig. 2.5 extends poleward and westward a considerable distance and results in an advection of basic state PV towards

the equator. This effect, included in Fig. 2.5 but excluded from the top panel of Fig. 3.2, tends to make the PV anomaly stronger and broader in both its westward and north-south extent, as seen in the bottom panel of Fig. 3.2. In spite of this weakness, the solution (3.10)

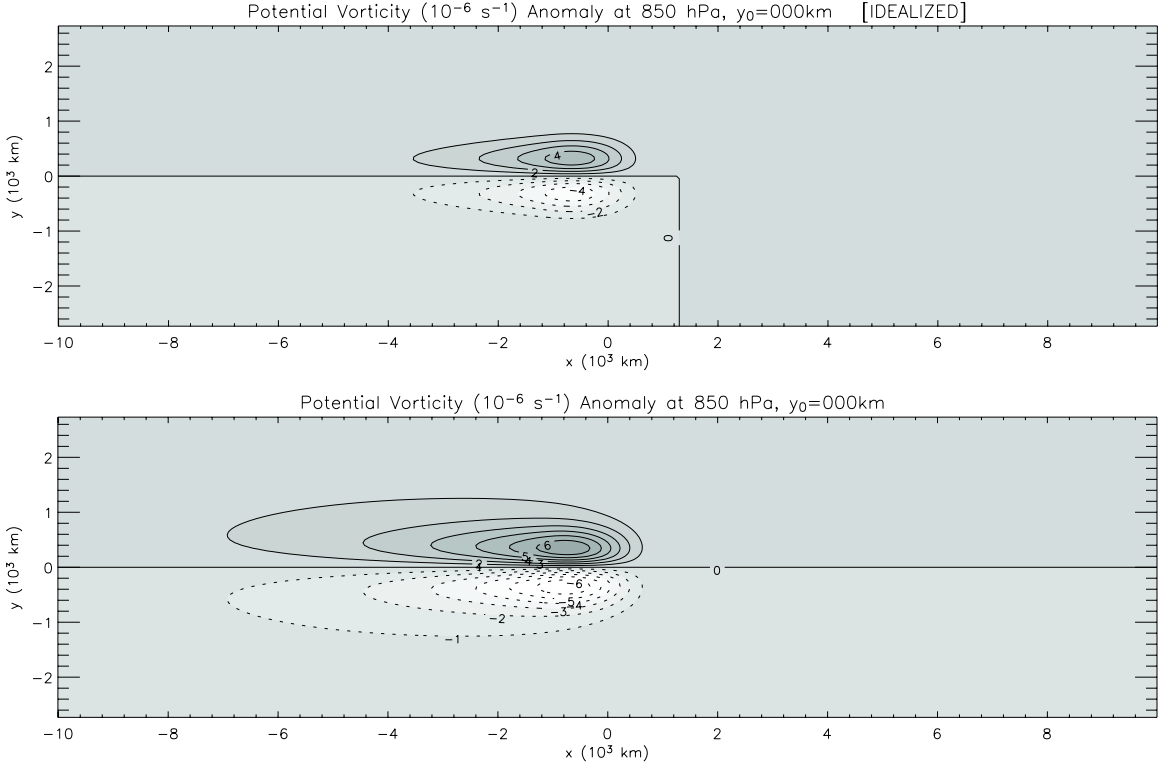


Figure 3.2: Potential vorticity anomalies q for $y_0 = 0$ km. The contour interval is $1 \times 10^{-6} \text{ s}^{-1}$. The top panel shows the hypothetical (idealized) potential vorticity distribution resulting from forcing and dissipation only, as computed from (3.10). The bottom panel, reproduced here for comparison, is the 850 hPa primitive equation Rossby component PV shown in the top panel of Fig. 3.1

reveals that three important parameters controlling the PV wake are the wake decay length c/α , the ratio of time scales τ_p/τ_c , and the dimensionless offset y_0/b_0 . For the example shown in the top panel Fig. 3.2 the wake decay length is $c/\alpha = 1728$ km, i.e., the PV anomaly trailing to the west of the convective region has a $1/e$ decay scale of 1728 km. The ratio τ_p/τ_c , which controls the strength of the PV anomaly, is a measure of the number of convective overturnings during the passage of the convection. The factor τ_p/τ_c is large, and the corresponding PV anomaly is large, for intensely raining, zonally wide, slowly moving

convective regions, while it is small, and the corresponding PV anomaly is small, for weakly raining, zonally narrow, fast moving convective regions. For the case shown in the bottom panel of Fig. 3.2, $a_0 = 1250$ km and $c = 5 \text{ m s}^{-1}$ so that $\tau_p = 69.4$ hr, while $\bar{c} = 41.25 \text{ m s}^{-1}$ and $Q_0/c_p = 12 \text{ K day}^{-1}$ so that $\tau_c = 11.9$ hr, resulting in $\tau_p/\tau_c = 5.8$.

Finally it is worth noting that the solution (3.10) can be used to obtain a rough indication of when nonlinear effects are expected to become important. For example, at 850 hPa and $x = -a_0$, and for $\alpha\tau_p \approx 0.72$, (3.10) becomes $q \approx -0.15(\tau_p/\tau_c)\beta y \exp[-(y - y_0)^2/b_0^2]$. As τ_p/τ_c becomes larger we expect that the potential vorticity anomaly q (and hence the relative vorticity $\partial v/\partial x - \partial u/\partial y$) will eventually become larger than βy , in which case the factor βy in the last term of (3.3) and (3.5) should be replaced by the total potential vorticity and the factor βy in the divergence term of (3.1) should be replaced by the absolute vorticity (a nonlinear effect). Although the inclusion of nonlinear terms in the case $\tau_p/\tau_c = 5.8$ should not lead to qualitative changes from the linear solution, larger values of τ_p/τ_c that cause intense westerly wind bursts ($\sim 15 \text{ m s}^{-1}$) should be expected to have significant nonlinear effects.

3.3 Invertibility Principle

We now show that the wind and mass fields in the wake of a convective envelope can be approximately recovered from the PV through a simple invertibility principle. The argument begins by returning to the PV anomaly expression, (3.4), written in the form

$$\nabla^2\psi + \frac{\beta y}{R\Gamma} \left(\frac{\partial}{\partial z} - 1 \right) \frac{\partial\phi}{\partial z} = q, \quad (3.12)$$

where ψ is the streamfunction for the rotational part of the flow and $\nabla^2 = \partial^2/\partial x^2 + \partial^2/\partial y^2$ is the horizontal Laplacian operator. No approximation has been made in writing the relative vorticity anomaly as $\nabla^2\psi$. Equation (3.12) can be converted into an invertibility principle by introducing an approximate balance relation between the wind and mass fields, i.e., a relation between ψ and ϕ . To derive this relationship start by differentiating the horizontal momentum equations, (2.6), along their respective orientations to get the divergence

equation,

$$\frac{\partial}{\partial t} \left(\frac{\partial u}{\partial x} + \frac{\partial v}{\partial y} \right) - \frac{\partial}{\partial x} (\beta y v) + \frac{\partial}{\partial y} (\beta y u) + \nabla^2 \phi = -\alpha \left(\frac{\partial u}{\partial x} + \frac{\partial v}{\partial y} \right). \quad (3.13)$$

In nearly balanced flows the divergence would be expected to be small. Furthermore, the magnitude of the dissipation and time rate of change of the divergence should be even smaller. Based on this the divergence terms that appear in (3.13) will be neglected. By the same rationale, it seems natural to approximate the total wind field by its rotational component. Using ψ , which was introduced above, this is done by writing

$$u \approx u_\psi \equiv -\frac{\partial \psi}{\partial y}, \quad v \approx v_\psi \equiv \frac{\partial \psi}{\partial x}. \quad (3.14)$$

Use of these two approximations in (3.13) reduces it to

$$-\frac{\partial}{\partial x} \left(\beta y \frac{\partial \psi}{\partial x} \right) - \frac{\partial}{\partial y} \left(\beta y \frac{\partial \psi}{\partial y} \right) + \nabla^2 \phi = 0, \quad (3.15)$$

which is known as the linear balance relation and can be written neatly as,

$$\nabla \cdot (\beta y \nabla \psi) = \nabla^2 \phi. \quad (3.16)$$

If we make the additional assumption that βy is slowly varying in space compared to ψ , (3.16) becomes

$$\nabla^2 (\beta y \psi) = \nabla^2 \phi. \quad (3.17)$$

Imposing the condition $\phi - \beta y \psi \rightarrow 0$ as $y \rightarrow \pm\infty$ on (3.17), it immediately follows that

$$\phi = \beta y \psi. \quad (3.18)$$

The validity of this last step is demonstrated in Appendix H. Returning to (3.12) and using the balance relation (3.18) to express ϕ in terms of ψ we arrive at

$$\nabla^2 \psi + \frac{\beta^2 y^2}{R\Gamma} \left(\frac{\partial}{\partial z} - 1 \right) \frac{\partial \psi}{\partial z} = q. \quad (3.19)$$

Concerning the boundary conditions for (3.19), we here use the simple conditions $\psi \rightarrow 0$ as $y \rightarrow \pm\infty$ and $\partial \psi / \partial z = 0$ at $z = 0, z_T$, noting that the lower condition could easily be

generalized to allow temperature variations at $z = 0$. Equation (3.19), together with its boundary conditions, constitute an invertibility principle. From this principle we can recover ψ , and then compute the rotational wind field from (3.14) and the mass field from (3.18). Although the invertibility principle (3.19) can be used in conjunction with an approximate PV equation to form a closed balanced theory (see section 3.4), our discussion in this section is limited to the use of (3.19) as a diagnostic aid for interpretation of the primitive equation model results.

To solve (3.19) we follow the arguments of sections 2.2 and 2.4 by separating off the vertical dependence, assuming the solution is steady in a reference frame moving eastward at speed c , and then taking the Fourier transform in the zonal direction. We find that (3.19) reduces to

$$\epsilon^{\frac{1}{2}} \left(\frac{d^2}{dy^2} - \hat{y}^2 \right) \hat{\psi}_m - m^2 \hat{\psi}_m = a^2 \hat{q}_m, \quad (3.20)$$

where, as before, $\hat{y} = \epsilon^{\frac{1}{4}}(y/a)$ is the dimensionless meridional coordinate. We now solve (3.20) by transforming in \hat{y} . The mathematical apparatus is simpler than in section 2.4 where we introduced the vector inner product (2.25), and the vector transform pair (2.36)–(2.37). To solve the scalar equation (3.20) we can use the scalar transform pair

$$\hat{\psi}_{mn} = \int_{-\infty}^{\infty} \hat{\psi}_m(\hat{y}) \mathcal{H}_n(\hat{y}) d\hat{y}, \quad (3.21)$$

$$\hat{\psi}_m(\hat{y}) = \sum_{n=0}^{\infty} \hat{\psi}_{mn} \mathcal{H}_n(\hat{y}). \quad (3.22)$$

A transform pair similar to (3.21) and (3.22) also exists for \hat{q}_{mn} , $\hat{q}_m(\hat{y})$. Note that (3.21) can be obtained through multiplication of (3.22) by $\mathcal{H}_{n'}(\hat{y})$, followed by integration over \hat{y} and use of the orthogonality relation (2.35). Multiplying (3.20) by $\mathcal{H}_n(\hat{y})$ and integrating over \hat{y} (i.e., taking the Hermite transform of (3.20)) we obtain

$$\hat{\psi}_{mn} = -\frac{a^2 \hat{q}_{mn}}{m^2 + \epsilon^{\frac{1}{2}} (2n + 1)}. \quad (3.23)$$

In the derivation of (3.23) we have used two integrations by parts (with vanishing boundary terms) and the fact that $\mathcal{H}_n(\hat{y})$ is an eigenfunction of the operator $(d^2/d\hat{y}^2 - \hat{y}^2)$, i.e.,

$(d^2/d\hat{y}^2 - \hat{y}^2)\mathcal{H}_n(\hat{y}) = -(2n+1)\mathcal{H}_n(\hat{y})$. The simplicity of the spectral form of the invertibility principle (3.23) is in fact due to this eigenfunction property of $\mathcal{H}_n(\hat{y})$.

Combining the inverse Hermite transform (3.22), inverse Fourier transform defined in (2.19), and the assumed vertical structure, we obtain

$$\psi(\xi, y, z) = Z(z) \sum_{m=-\infty}^{\infty} \sum_{n=0}^{\infty} \hat{\psi}_{mn} \mathcal{H}_n(\hat{y}) e^{im\xi/a}, \quad (3.24)$$

so that the physical space streamfunction field can be plotted by substituting (3.23) in (3.24) and then numerically evaluating the sums over m and n . However, we would like to examine more than just the $\psi(\xi, y, z)$ field, in particular the $u_\psi(\xi, y, z)$, $v_\psi(\xi, y, z)$, and $\phi(\xi, y, z)$ fields, all of which can be determined from the ψ field. Recalling that $u_\psi = -\partial\psi/\partial y$, $v_\psi = \partial\psi/\partial\xi$, and $\phi = \beta y\psi$, and using the recurrence and derivative relations (2.30) and (2.31), we have

$$\begin{pmatrix} u_\psi(\xi, y, z) \\ v_\psi(\xi, y, z) \\ \phi(\xi, y, z) \end{pmatrix} = Z(z) \sum_{m=-\infty}^{\infty} \sum_{n=0}^{\infty} \frac{\hat{\psi}_{mn}}{a} \begin{pmatrix} U_{mn}(\xi, \hat{y}) \\ V_{mn}(\xi, \hat{y}) \\ \Phi_{mn}(\xi, \hat{y}) \end{pmatrix} \quad (3.25)$$

where

$$\begin{pmatrix} U_{mn}(\xi, \hat{y}) \\ V_{mn}(\xi, \hat{y}) \\ \Phi_{mn}(\xi, \hat{y}) \end{pmatrix} = \begin{pmatrix} \epsilon^{\frac{1}{4}} \left[\left(\frac{n+1}{2}\right)^{\frac{1}{2}} \mathcal{H}_{n+1}(\hat{y}) - \left(\frac{n}{2}\right)^{\frac{1}{2}} \mathcal{H}_{n-1}(\hat{y}) \right] \\ im\mathcal{H}_n(\hat{y}) \\ \bar{c}\epsilon^{\frac{1}{4}} \left[\left(\frac{n+1}{2}\right)^{\frac{1}{2}} \mathcal{H}_{n+1}(\hat{y}) + \left(\frac{n}{2}\right)^{\frac{1}{2}} \mathcal{H}_{n-1}(\hat{y}) \right] \end{pmatrix} e^{im\xi/a}, \quad (3.26)$$

which are readily seen to be the Rossby wave approximations of (2.28). To summarize, once \hat{q}_{mn} is known, we can compute $\hat{\psi}_{mn}$ from (3.23), and then $u_\psi(\xi, y, z)$, $v_\psi(\xi, y, z)$, $\phi(\xi, y, z)$ via numerical evaluation of (3.25). For \hat{q}_{mn} in (3.23) we use the Rossby wave contribution to the total $q(\xi, y, z)$ field given in (3.7), i.e., we set $\hat{q}_{mn} = \hat{q}_{mn0}$, the latter of which is defined in (3.8). This is a reasonable approximation since the total $q(\xi, y, z)$ field is dominated by the Rossby wave contribution, as argued in section 3.1. For Fig. 3.3 the center of convective forcing is set to $y_0 = 0$ km. The top panel displays the Rossby PV field for reference. The second panel contains the flow field, $u_\psi(\xi, y, z)$, $v_\psi(\xi, y, z)$, and $\phi(\xi, y, z)$, attained from inverting the Rossby PV with (3.19). Lastly, the primitive

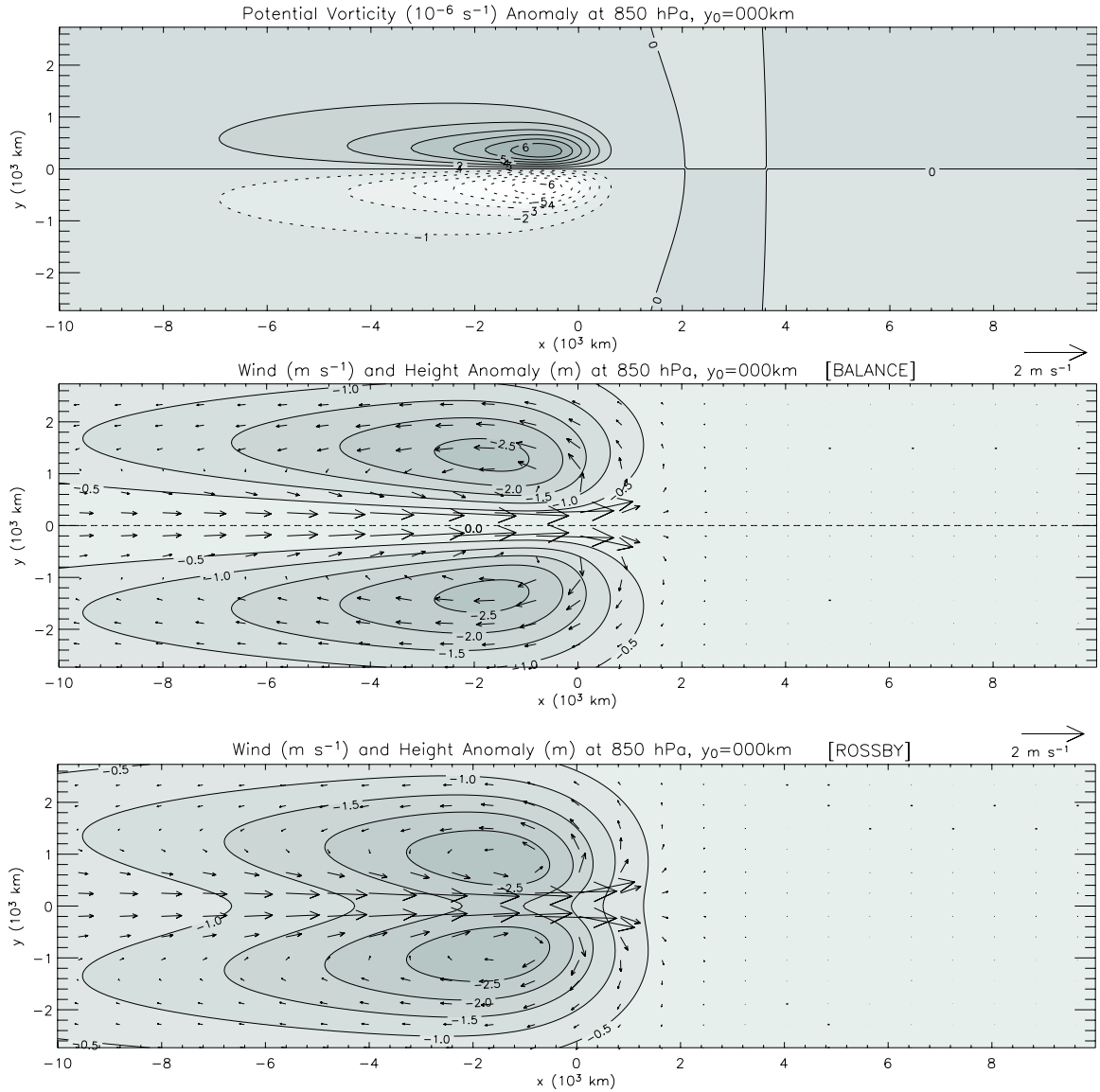


Figure 3.3: The top panel shows the Rossby wave contribution to the $q(\xi, y, z)$ field, while the second panel shows the $u_\psi(\xi, y, z)$, $v_\psi(\xi, y, z)$, $\phi(\xi, y, z)$ fields resulting from the solution of the invertibility principle (3.19) when its right hand side is given by the PV field shown in the top panel. The bottom panel is the Rossby contribution to the primitive equation circulation, included here for comparison with the middle panel. This figure is for $y_0 = 0 \text{ km}$.

equation Rossby component flow field is shown for comparison with the flow field recovered from the invertibility principle. The same fields are shown for $y_0 = 450 \text{ km}$ in Fig. 3.4. A comparison of the circulation fields for each figure shows that the balanced model mass field and rotational wind field are fairly good approximations of the Rossby wave contributions to the primitive equation results, the most apparent difference being that the zonal pressure

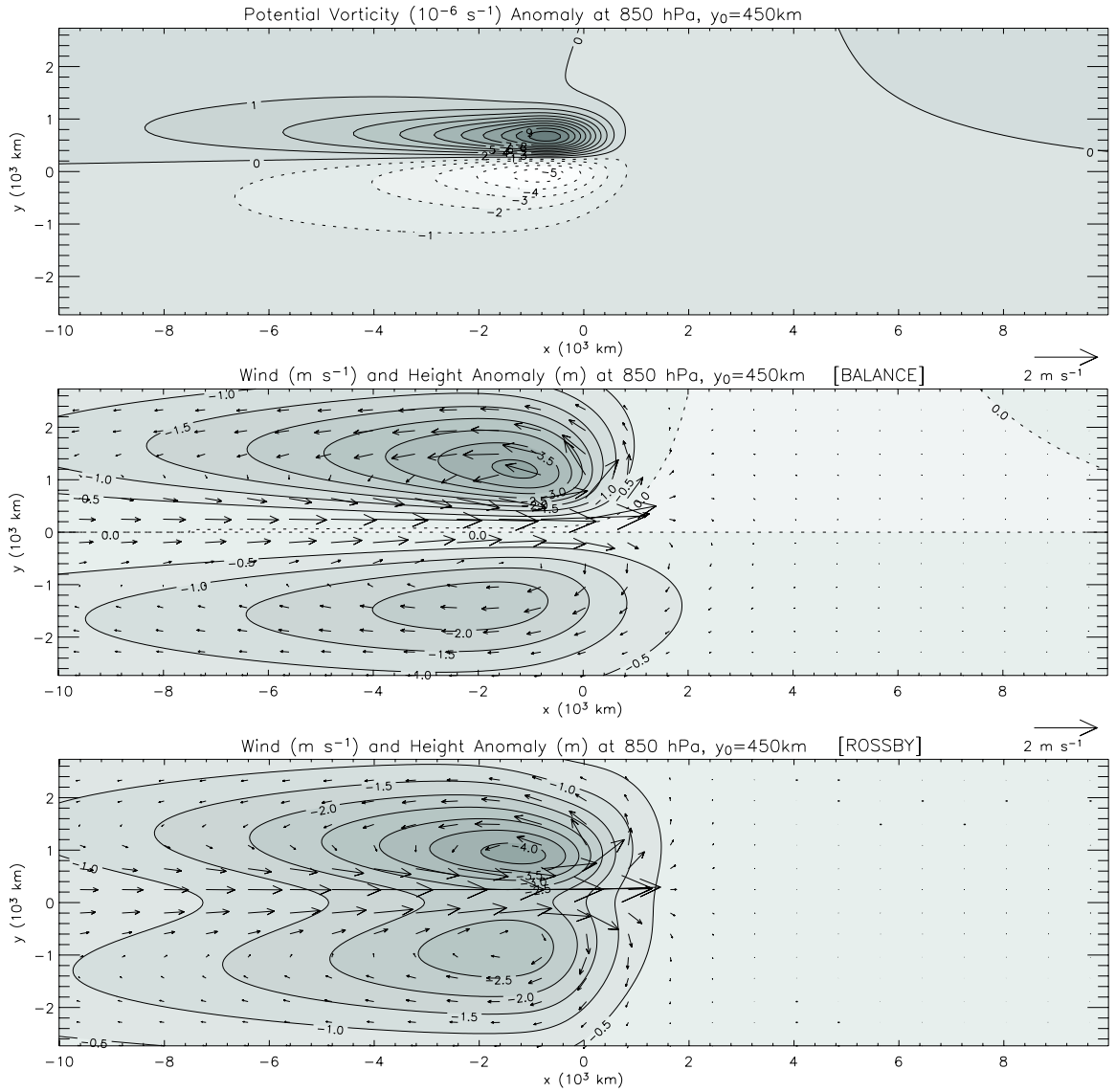


Figure 3.4: Same as Fig. 3.3 but for $y_0 = 450$ km.

gradient force at the equator in the primitive equation model is not reproduced in the solutions of the invertibility principle. Mathematically this is expected from the balance relationship, (3.18), which dictates that $\phi = 0$ at the equator due to the βy factor. However, an advantage of this balance relation should be noted as well. Compared to geostrophic balance, (3.18) is preferred because it is valid over the entire equatorial domain including the equator. In other words, the streamfunction derivative relationships for the rotational wind components, (3.14), can be evaluated at the equator, while the geostrophic wind relations

have a singularity there due to vanishing of the Coriolis force. It's worthwhile to point out the distinction between the wind fields computed in Quasi-Geostrophic (QG) theory and those computed under our equatorial β -plane approximate balance theory. In QG theory the horizontal wind is considered to be composed of geostrophic and ageostrophic components. After determining the geopotential by inverting the PV, the geostrophic component of the wind field is recovered from the geopotential. Under our equatorial balance theory we consider the wind to be composed of rotational and divergent components. In this case the PV is inverted to determine the streamfunction, which is then used to recover the rotational wind components. Having pointed out the difference, some similarity can also be seen. Differentiating (3.18) independently in the zonal direction and in the meridional direction, then using (3.14) yields

$$\beta y v_\psi = \frac{\partial \phi}{\partial x}, \quad \beta y u_\psi = -\frac{\partial \phi}{\partial y} + \beta \psi. \quad (3.27)$$

The relationship involving the meridional rotational wind and zonal pressure gradient is evocative of geostrophic balance, though the zonal rotational wind and meridional pressure gradient expression involves an additional term.

As a side note, the invertibility principle could have been expressed in terms of ϕ instead of ψ using (3.18), though inversion would probably be more difficult if possible. Interestingly, it has been suggested that, for some flow patterns, inversion of PV for ψ may give more accurate forecast results than inverting PV for ϕ (Phillips, 2000).

3.4 Proposed Prognostic Equation

It was noted that the invertibility principle (3.19) could be used as part of a complete balanced theory, i.e., it can be used in conjunction with an approximate PV equation. For example, in the context of inviscid, adiabatic flow we could consider the system

$$\frac{\partial q}{\partial t} + \beta \frac{\partial \psi}{\partial x} = 0, \quad (3.28)$$

$$\nabla^2 \psi + \frac{\beta^2 y^2}{R\Gamma} \left(\frac{\partial}{\partial z} - 1 \right) \frac{\partial \psi}{\partial z} = q, \quad (3.29)$$

for the dependent variables $q(x, y, z, t)$ and $\psi(x, y, z, t)$. Using (3.29) in (3.28) we can easily obtain a single equation for $\psi(x, y, z, t)$ and then show that solutions proportional to $Z(z)\mathcal{H}_n(\hat{y}) \exp[i(mx/a - \nu_{mn}t)]$ exist provided that

$$\frac{\nu_{mn}}{2\Omega} = -\frac{m}{m^2 + \epsilon^{\frac{1}{2}}(2n+1)}. \quad (3.30)$$

The dimensionless frequencies given by (3.30) represent an approximation to the low frequency solutions of the cubic equation (2.27). These approximate Rossby wave frequencies are plotted as the red lines in Fig. 3.5, while the exact primitive equation Rossby frequencies given by (2.27) are plotted as the blue lines. An inspection of Fig. 3.5 shows that the balanced model Rossby wave frequencies (3.30) are very good approximations to the primitive equation frequencies, with the exception of low zonal wavenumber sectoral harmonics, i.e., small $|m|$ for $n = 0$ (mixed Rossby-gravity mode). A simple interpretation of this result is that, in the primitive equation model, the low zonal wavenumber sectoral harmonics involve a combination of gravity wave dynamics and potential vorticity dynamics, and the balance model is able to accurately capture only the potential vorticity part of the dynamics. In cases where the $n = 0$ modes are absent or only weakly forced (e.g., when $y_0 = 0$ or $y_0 \ll b_0$) one might expect that accurate simulations of the MJO wake could be obtained by simply including in (3.28) the same forcing and dissipation terms that appear on the right hand side of (3.3). Having constructed solutions of such a model, we found that they are not accurate approximations to the primitive equation results discussed in Chapter 2. The problem is not in the approximation (3.29), but rather in the approximation of βv by $\beta \partial \psi / \partial x$ in the PV equation. In other words, the problem lies in the neglect of the advection of basic state PV by the divergent part of the flow. Examples of such divergent flows are shown in the third panel of Fig. 2.5 and in the fourth panel of Fig. 2.7. The flows extend poleward of the heated region and result in PV anomalies that are stronger and extend farther poleward than in models which approximate βv by $\beta \partial \psi / \partial x$.

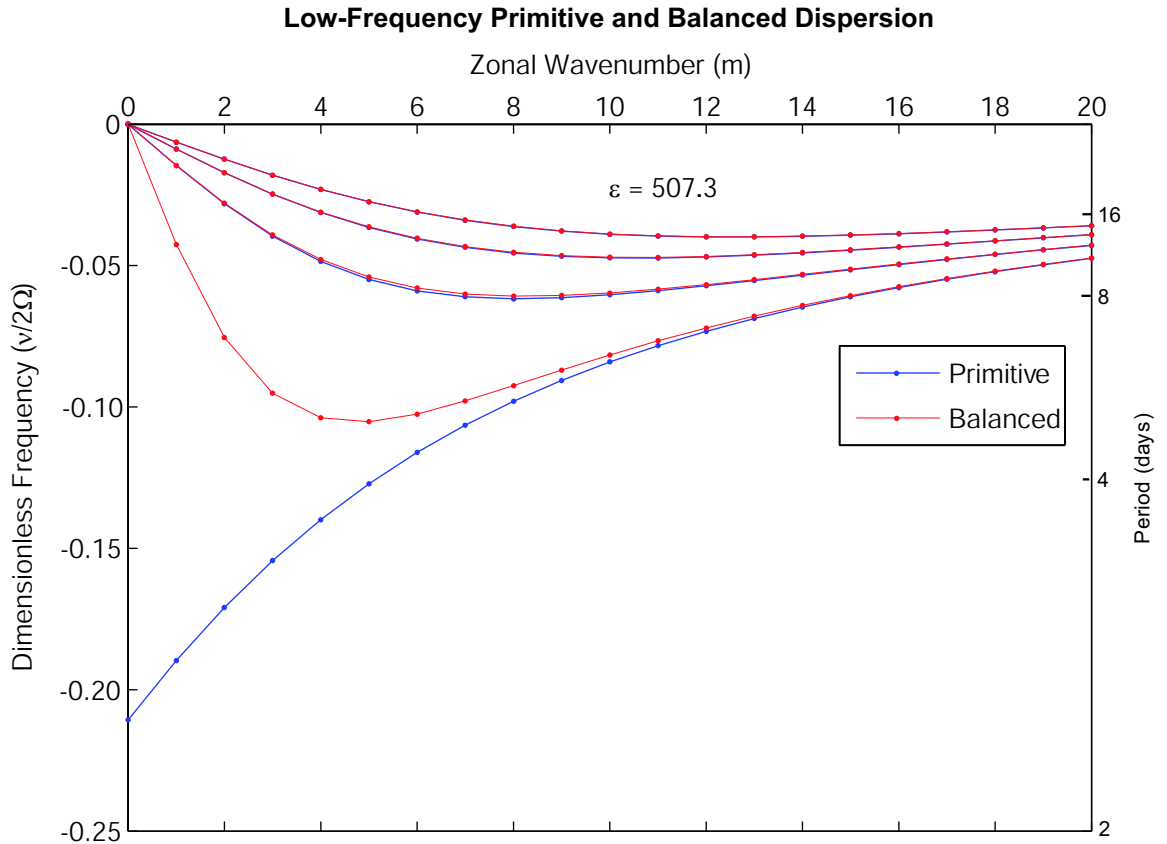


Figure 3.5: The blue lines show the dimensionless frequencies $\nu_{mnr}/2\Omega$ ($n = 0, 1, 2, 3$) for the Rossby modes ($r = 0$), as determined from the primitive equation dispersion relation (2.27). The red lines show the dimensionless frequencies $\nu_{mn}/2\Omega$ ($n = 0, 1, 2, 3$) as determined from the balanced model dispersion relation (3.30).

Chapter 4

ENERGY CONSIDERATIONS

4.1 Energy Principle

We discussed earlier the steady state assumption under which our solutions are valid. If we assume this in looking at the total energy of the system, we should arrive at a relation that describes an equilibrium energy state. Return to the linearized governing equations, (2.6), to derive a total energy principle for the model domain. Start with the horizontal momentum equations to get the kinetic energy equation,

$$\frac{\partial K_E}{\partial t} + \mathbf{v} \cdot \nabla \phi = -2\alpha K_E, \quad (4.1)$$

where \mathbf{v} is the horizontal velocity vector, and $K_E = \frac{1}{2}(u^2 + v^2)$ is the kinetic energy per unit mass. The thermodynamic equation and hydrostatic relation yield the potential energy equation,

$$\frac{\partial P_E}{\partial t} + w \frac{\partial \phi}{\partial z} = -2\alpha P_E + \frac{\kappa}{R\Gamma} \frac{\partial \phi}{\partial z} Q, \quad (4.2)$$

where $P_E = \frac{1}{2} \frac{1}{R\Gamma} (\frac{\partial \phi}{\partial z})^2$ is the potential energy. Combining (4.1) and (4.2) using the continuity equation, then integrating over the entire mass, we arrive at the total energy principle for (x, y, z, t) space,

$$\frac{d\mathcal{E}}{dt} = -2\alpha\mathcal{E} + \mathcal{G}, \quad (4.3)$$

where the total energy \mathcal{E} and the generation term \mathcal{G} are defined by

$$\begin{aligned} \mathcal{E} &= \iiint \frac{1}{2} \left[u^2 + v^2 + \frac{1}{R\Gamma} \left(\frac{\partial \phi}{\partial z} \right)^2 \right] e^{-z} dx dy dz, \\ \mathcal{G} &= \iiint \frac{1}{R\Gamma} \frac{\partial \phi}{\partial z} \kappa Q e^{-z} dx dy dz. \end{aligned} \quad (4.4)$$

Note that in the log-pressure vertical coordinate system, e^{-z} is pseudo-density. From (4.3) we see that the total energy of the system increases due to diabatic generation and decreases due to dissipation (the combined effects of friction and radiative cooling). In the steady state described previously $d\mathcal{E}/dt = 0$, and the total energy principle reduces to a balance between these two terms,

$$2\alpha\mathcal{E} = \mathcal{G}. \quad (4.5)$$

In solving the primitive equations we first separated the vertical and horizontal structures and then continued by solving the remaining set of equations dependent on (x, y, t) . Most of what follows will focus on this “shallow water” system so we would like to find the energy principle associated with it as well. By starting with the set of equations (2.14) and following the same procedure as above, we arrive at an analogous shallow water energy principle,

$$2\alpha\hat{\mathcal{E}} = \hat{\mathcal{G}}. \quad (4.6)$$

Here the total energy and generation terms are defined as,

$$\begin{aligned}\hat{\mathcal{E}} &= \iint \frac{1}{2} \left(\hat{u}^2 + \hat{v}^2 + \frac{1}{\bar{c}^2} \hat{\phi}^2 \right) dx dy, \\ \hat{\mathcal{G}} &= \iint \frac{\kappa}{\bar{c}^2} \hat{\phi} \hat{Q} dx dy,\end{aligned}\quad (4.7)$$

where the $(\hat{\cdot})$'s denote the lack of vertical dependence. This shallow water expression for total energy motivated the inner product defined in (2.25).

Recalling the structure of the diabatic forcing (2.15), the energy generation is due to a nonzero Q in a localized, eastward moving region near the equator. We can now show that the dissipation occurs in the much broader area into which the energy has propagated via equatorial wave motions. Wave energy propagates in the direction of the group velocity vector. The zonal component of a group velocity vector can be expressed as the partial derivative of frequency with respect to the zonal wavenumber. From this, zonal group velocity at any point can be found as the slope of a dispersion curve at that point when the frequency is plotted over continuous zonal wavenumbers. However, in our case zonal

wavenumbers take on only integer values so this definition is not valid. The speed (\mathcal{C}) at which energy propagates in the discrete wavenumber case is addressed in Appendix I. This speed can be seen as the generalization of the group velocity concept to a discrete wavenumber domain and is expressed as

$$\mathcal{C} = \hat{\nu}_{m+1,n,r} - \hat{\nu}_{m,n,r}, \quad (4.8)$$

where $m + 1 > m$ are consecutive integer zonal wavenumbers. This expression can be used to visually determine the direction of energy propagation by the sign of the slope between two consecutive frequencies. The majority of the wave response energy is contained in the Rossby and Kelvin modes, as will be shown in section 4.3. The phase speed of the Rossby wave is dependent on wavenumber, thus making it a dispersive wave. Referring to the primitive equation dispersion curves (blue lines, $n = 1, 2, 3$) in Figure 3.5, the slope between adjacent frequencies is clearly negative at least up to $m = 7$ for all meridional modes shown. This requires all energy in these wavenumbers to propagate to the west. Another result shown in section 4.3 is that all but a negligible amount of total energy is contained in lower zonal wavenumbers. The other wave type containing a significant portion of total energy, the Kelvin wave, has a constant phase speed of $c_K \equiv \frac{\hat{\nu}_{m-1,2}}{m} = \epsilon^{-1/2}$, so is non-dispersive by definition. A property of non-dispersive waves is that their phase speed is equivalent to the group speed. Since the phase speed is positive the Kelvin wave always propagates to the east, as does its energy. In summary, the Rossby response that appears to the west of the forcing carries its associated energy away from the source to the west. On the east side of the forcing where the Kelvin response occurs, the energy is carried away to the east. So in the zonal sense, the constant energy generation is balanced by dissipation of energy in the far field, which is carried there from the localized source by the Rossby-Kelvin response.

4.2 Parseval Relation

A form of Parseval's Theorem is expressed as

$$\int_{-\infty}^{\infty} |f(x)|^2 dx = \frac{1}{2\pi} \int_{-\infty}^{\infty} |F(k)|^2 dk, \quad (4.9)$$

where $F(k) = \mathcal{F}\{f(x)\}$ represents the Fourier transform of $f(x)$ and k represents the wavenumber component at x . This states physically that the energy (assumed to be $|f(x)|^2$) contained in a waveform $f(x)$ integrated across all physical space (x) is equal to the total energy of the waveform's Fourier transform $F(k)$ integrated over all of its wavenumber components (k). This is expected since the physical and wavenumber domains are equivalent representations of the same signal, so they must have the same energy. In this way it is a statement of conservation of energy.

The solutions found in Chapter 2 were attained by transform methods. More specifically, a zonal Fourier transform followed by a meridional normal mode transform (based on Hermite polynomials). Parseval's Theorem can be applied to any orthogonal basis of eigenfunctions, so a relation based on the the above mentioned transforms is valid. To derive a 2-dimensional Parseval relation for our system we will first construct the zonal relation, followed by the meridional relation, finally combining the two we arrive at the desired result. As the zonal relation is based on the Fourier transform, it will take a form similiar to that of (4.9), though modified for our model geometry. The zonal periodicity of our domain requires that the left hand side of (4.9) be modified by $\int_{-\infty}^{\infty} \rightarrow \sum_{k=-\infty}^{\infty}$. Likewise, the wavenumbers take only integer values so the right hand side becomes an infinite sum $\int_{-\infty}^{\infty} \rightarrow \sum_{k=-\infty}^{\infty}$, which allows us to partition the energy according to any wavenumber. The argument begins with the expression for total energy in (x, y, z, t) -space found in section 4.1,

$$\mathcal{E} = \int_0^{z_T} \int_{-\infty}^{\infty} \int_{-\pi a}^{\pi a} \frac{1}{2} \left[u^2 + v^2 + \frac{1}{R\Gamma} \left(\frac{\partial \phi}{\partial z} \right)^2 \right] e^{-z} dx dy dz. \quad (4.10)$$

Using the separable forms given in (2.12) and noting that

$$\int_0^{z_T} Z^2 e^{-z} dz = \frac{z_T^3 e^{-z_m}}{2\pi^2}, \quad \int_0^{z_T} Z'^2 e^{-z} dz = \frac{z_T^3 e^{-z_m}}{2\pi^2 \bar{c}^2},$$

the vertical integrals in (4.10) can be evaluated to give

$$\mathcal{E} = \frac{z_T^3 e^{-z_m}}{2\pi^2} \int_{-\infty}^{\infty} \int_{-\pi a}^{\pi a} \frac{1}{2} \left(\hat{u}^2 + \hat{v}^2 + \frac{1}{\bar{c}^2} \hat{\phi}^2 \right) dx dy. \quad (4.11)$$

Next, we convert the variables of integration to the translating zonal coordinate, $\xi = x - ct$, and the dimensionless meridional coordinate, $\hat{y} = \epsilon^{\frac{1}{4}} y/a$,

$$\mathcal{E} = \frac{az_T^3 e^{-z_m}}{2\pi^2 \epsilon^{\frac{1}{4}}} \int_{-\infty}^{\infty} \int_{-\pi a}^{\pi a} \frac{1}{2} \left(\hat{u}^2 + \hat{v}^2 + \frac{1}{\bar{c}^2} \hat{\phi}^2 \right) d\xi d\hat{y}. \quad (4.12)$$

Proceeding from here we will develop the zonal Parseval relation just for \hat{u} , the general form of which is valid for both \hat{v} and $\hat{\phi}$ as well. The sum of the three will constitute a Parseval relation for the total energy. The Fourier transform pair for $\hat{u}(\xi, y)$,

$$\hat{u}_m(y) = \frac{1}{2\pi a} \int_{-\pi a}^{\pi a} \hat{u}(\xi, y) e^{-im\xi/a} d\xi, \quad \hat{u}(\xi, y) = \sum_{m=-\infty}^{\infty} \hat{u}_m(y) e^{im\xi/a}, \quad (4.13)$$

was introduced in equation (2.19). Using the inverse transform, $|\hat{u}(\xi, y)|^2$ can be written as

$$|\hat{u}(\xi, y)|^2 = \left(\sum_{m=-\infty}^{\infty} \hat{u}_m(y) e^{\frac{im\xi}{a}} \right) \left(\sum_{m'=-\infty}^{\infty} \hat{u}_{m'}(y) e^{\frac{im'\xi}{a}} \right)^*,$$

where the $*$ symbol represents a complex conjugate. Integrating over the entire zonal domain and dropping the $|()$ on the left hand side (all our physical space functions will be real) gives,

$$\int_{-\pi a}^{\pi a} \hat{u}^2(\xi, y) d\xi = \sum_m \sum_{m'} \hat{u}_m(y) \hat{u}_{m'}^*(y) \int_{-\pi a}^{\pi a} e^{\frac{i(m-m')\xi}{a}} d\xi.$$

Noting that $\int_{-\pi a}^{\pi a} e^{\frac{i(m-m')\xi}{a}} d\xi$ evaluates to $2\pi a$ for $m = m'$, and 0 for $m \neq m'$, yields the zonal Parseval relation,

$$\frac{1}{2\pi a} \int_{-\pi a}^{\pi a} \hat{u}^2(\xi, y) d\xi = \sum_m \hat{u}_m(y) \hat{u}_m^*(y) \quad (4.14)$$

Using similar Parseval relations for $\hat{v}(\xi, y)$ and $\hat{\phi}(\xi, y)$ we can write,

$$\frac{1}{2\pi a} \int_{-\pi a}^{\pi a} \left(\hat{u}^2 + \hat{v}^2 + \frac{1}{\bar{c}^2} \hat{\phi}^2 \right) d\xi = \sum_{m=-\infty}^{\infty} \left(\hat{u}_m \hat{u}_m^* + \hat{v}_m \hat{v}_m^* + \frac{1}{\bar{c}^2} \hat{\phi}_m \hat{\phi}_m^* \right). \quad (4.15)$$

Integrating (4.15) over \hat{y} we obtain

$$\begin{aligned} \frac{1}{2\pi a} \int_{-\infty}^{\infty} \int_{-\pi a}^{\pi a} \left(\hat{u}^2 + \hat{v}^2 + \frac{1}{\bar{c}^2} \hat{\phi}^2 \right) d\xi d\hat{y} &= \sum_{m=-\infty}^{\infty} \int_{-\infty}^{\infty} \left(\hat{u}_m \hat{u}_m^* + \hat{v}_m \hat{v}_m^* + \frac{1}{\bar{c}^2} \hat{\phi}_m \hat{\phi}_m^* \right) d\hat{y} \\ &= \sum_{m=-\infty}^{\infty} (\hat{\eta}_m, \hat{\eta}_m), \end{aligned} \quad (4.16)$$

where the last equality follows from the definitions for the inner product (2.25) and zonally transformed solution vector (2.24). Using (2.37) to normal mode expand $\hat{\eta}_m$ allows the inner product in (4.16) to be expressed as

$$\begin{aligned} (\hat{\eta}_m, \hat{\eta}_m) &= \left(\sum_{n=-1}^{\infty} \sum_r \hat{\eta}_{mn} \mathbf{K}_{mn}, \sum_{n'=-1}^{\infty} \sum_{r'} \hat{\eta}_{mn'} \mathbf{K}_{mn'} \right) \\ &= \sum_{n=-1}^{\infty} \sum_r \sum_{n'=-1}^{\infty} \sum_{r'} \hat{\eta}_{mn} \hat{\eta}_{mn'}^* (\mathbf{K}_{mn}, \mathbf{K}_{mn'}) \\ &= \sum_{n=-1}^{\infty} \sum_r \hat{\eta}_{mn} \hat{\eta}_{mn}^*. \end{aligned} \quad (4.17)$$

The middle relationship was due to the inner product definition (2.25), and the last was a result of the orthonormality of the eigenfunctions (2.34). Combining results from (4.16) and (4.17) we arrive at the combined Parseval relation

$$\frac{1}{2\pi a} \int_{-\infty}^{\infty} \int_{-\pi a}^{\pi a} \left(\hat{u}^2 + \hat{v}^2 + \frac{1}{\bar{c}^2} \hat{\phi}^2 \right) d\xi d\hat{y} = \sum_{m=-\infty}^{\infty} \sum_{n=-1}^{\infty} \sum_r \hat{\eta}_{mn} \hat{\eta}_{mn}^*. \quad (4.18)$$

By using (4.18) in (4.12) the physical space integral expression for total energy can be reformulated in terms of a spectral summation

$$\mathcal{E} = \frac{a^2 z_T^3 e^{-z_m}}{2\pi \epsilon^{\frac{1}{4}}} \sum_{m=-\infty}^{\infty} \sum_{n=-1}^{\infty} \sum_r \hat{\eta}_{mn} \hat{\eta}_{mn}^*. \quad (4.19)$$

Equation (4.19) is convenient to use computationally because $\hat{\eta}_{mn}$ must be calculated to generate the primitive equation solutions. However, using the derived expression for $\hat{\eta}_{mn}$ in (2.38) reduces (4.19) to a more transparent form,

$$\mathcal{E} = \frac{a^2 z_T^3 e^{-z_m}}{2\pi \epsilon^{\frac{1}{4}}} \sum_{m=-\infty}^{\infty} \sum_{n=-1}^{\infty} \sum_r \frac{\kappa^2 \hat{Q}_{mn}^2}{\alpha^2 + (\nu_{mn} - \tilde{\nu}_m)^2}, \quad (4.20)$$

where $\tilde{\nu}_m = c(m/a)$ is the dimensional frequency of the convective forcing. So the term $(\nu_{mn} - \tilde{\nu}_m)^2$ accounts for the response energy dependence on resonance between the forcing

frequency and the natural frequencies of the system (Chao, 1987). Note that for the case of pure resonance in the absence of friction ($\alpha = 0$) the energy would become infinite.

To summarize, we can calculate the total steady state energy of our system (\mathcal{E}) from the physical space integral in (4.10), or equivalently from the spectral space sum in (4.19). An advantage of using (4.19) is the ability to partition the total energy into the fractions associated with the different equatorial wave types, as will be done in the next section.

4.3 Parameter Dependency

In this section we use the Parseval relation (4.19) to analyze the energy response to variations in the forcing parameters. As mentioned, we are able to look at the energy distribution among wave types as well as the total. The convective forcing parameters we are able to vary are: phase speed (c), zonal halfwidth (a_0), meridional e-folding width (b_0), and meridional offset of the center of forcing from the equator (y_0). The default values for these parameters (used in figures (2.5) and (2.6)) are $c = 5 \text{ m s}^{-1}$, $a_0 = 1250 \text{ km}$, $b_0 = 450 \text{ km}$, and $y_0 = 0 \text{ km}$. With the exception of the horizontal length scales of the forcing, as one parameter is varied the other three will be held fixed at these default values. An increase (decrease) of either a_0 or b_0 while the other is held fixed corresponds to an increase (decrease) of the heating area, and thus an increase (decrease) of the response energy. In this case it makes more sense to vary a_0 and b_0 simultaneously in such a way that the heating area ($\pi a_0 b_0$) remains constant, versus varying a_0 and b_0 individually.

The normalized total energy, \mathcal{E}_T , is the sum of energy contributions from all wave types divided by \mathcal{E}_* , the normalization energy.

$$\mathcal{E}_T = \frac{\sum_{m=-M}^M \sum_{n=-1}^N \sum_{r=0}^2 \hat{\eta}_{mnr} \hat{\eta}_{mnr}^*}{\mathcal{E}_*} \quad (4.21)$$

Note that the constant factor ($\frac{a^2 z_T^3 e^{-z_m}}{2\pi\epsilon^{\frac{1}{4}}}$) that appears in (4.19) does not appear above due to cancellation from division by \mathcal{E}_* . The fractions of \mathcal{E}_T belonging to a specific wave type

can be written as

$$\mathcal{E}_{\mathcal{R}} = \frac{\sum_{m=-M}^M \sum_{n=1}^N \hat{\eta}_{mn,0} \hat{\eta}_{mn,0}^*}{\mathcal{E}_*}, \quad (4.22)$$

$$\mathcal{E}_{\mathcal{M}} = \frac{\sum_{m=-M}^M \hat{\eta}_{m,0,0} \hat{\eta}_{m,0,0}^*}{\mathcal{E}_*}, \quad (4.23)$$

$$\mathcal{E}_{\mathcal{G}} = \frac{\sum_{m=-M}^M \left(\sum_{n=1}^N \sum_{r=1}^2 \hat{\eta}_{mnr} \hat{\eta}_{mnr}^* \right) + \hat{\eta}_{m,0,2} \hat{\eta}_{m,0,2}^*}{\mathcal{E}_*}, \quad (4.24)$$

$$\mathcal{E}_{\mathcal{K}} = \frac{\sum_{m=-M}^M \hat{\eta}_{m,-1,2} \hat{\eta}_{m,-1,2}^*}{\mathcal{E}_*}, \quad (4.25)$$

where $\mathcal{E}_{\mathcal{R}}$ corresponds to the Rossby energy, $\mathcal{E}_{\mathcal{M}}$ the mixed Rossby-gravity energy, $\mathcal{E}_{\mathcal{G}}$ the inertia-gravity energy, and $\mathcal{E}_{\mathcal{K}}$ the Kelvin energy. Note that the infinite sums have been truncated in m and n by $\infty \rightarrow M$ and $\infty \rightarrow N$, respectively.

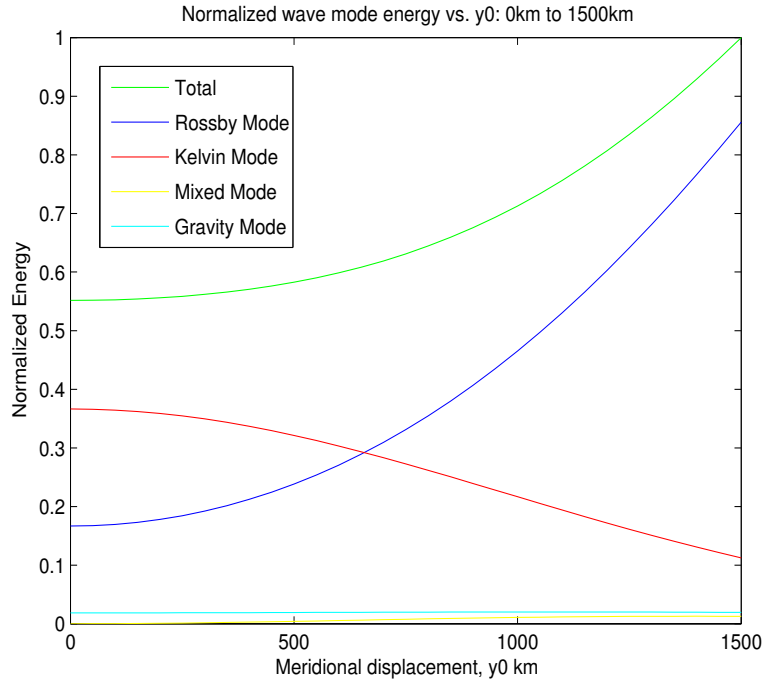


Figure 4.1: Normalized energy vs. y_0 (meridional displacement from the equator of the center of forcing).

In the first plot, Fig. 4.1, the displacement of the center of forcing from the equator is varied. The first thing to note from this figure, which will be obvious in the plots that follow as well, is the nonzero but very small contribution from the inertia-gravity wave.

Next, recall the mixed Rossby-gravity wave is anti-symmetric about the equator and its

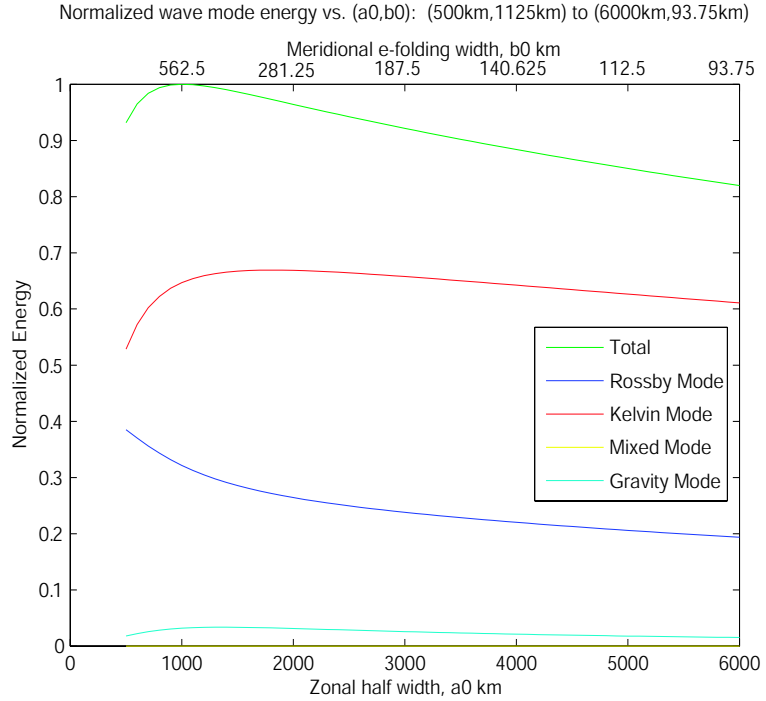


Figure 4.2: Normalized energy vs. [zonal halfwidth (a_0), meridional e-folding width (b_0)] of diabatic forcing, such that the horizontal area of heating (ellipse of area $\pi a_0 b_0$) remains constant.

response is identically zero for $y_0 = 0$. As would be expected its contribution becomes nonzero and grows as the center of forcing is moved away from the equator. However, even at $y_0 = 1500$ km which is an extreme value for our interest, the contribution is less than that of the inertia-gravity response and is essentially negligible. The total response energy is then seen to be composed primarily of the Rossby and Kelvin contributions, so on these grounds the mixed Rossby-gravity and inertia-gravity energy contributions will be neglected in the discussion that follows. Moving the source off the equator causes the total response energy to grow with increasing distance. For disturbances close to the equator the Kelvin wave is the largest contributor to the total. As y_0 increases the Kelvin portion slowly decreases and the Rossby portion soon starts to increase rapidly. At $y_0 \sim 650$ km the two components have equivalent energy contributions, and at the extremity the response is largely Rossby. The simplicity of the Kelvin wave energy dependence on \hat{y}_0 allows its

behavior to be verified mathematically, though this is not the case for the Rossby component which has a much more complicated dependence. Looking back at (4.20) with the spectral space heating ($Q_{m,-1,2}$) defined in (2.40), the decay with increasing y_0 is expected from the gaussian term.

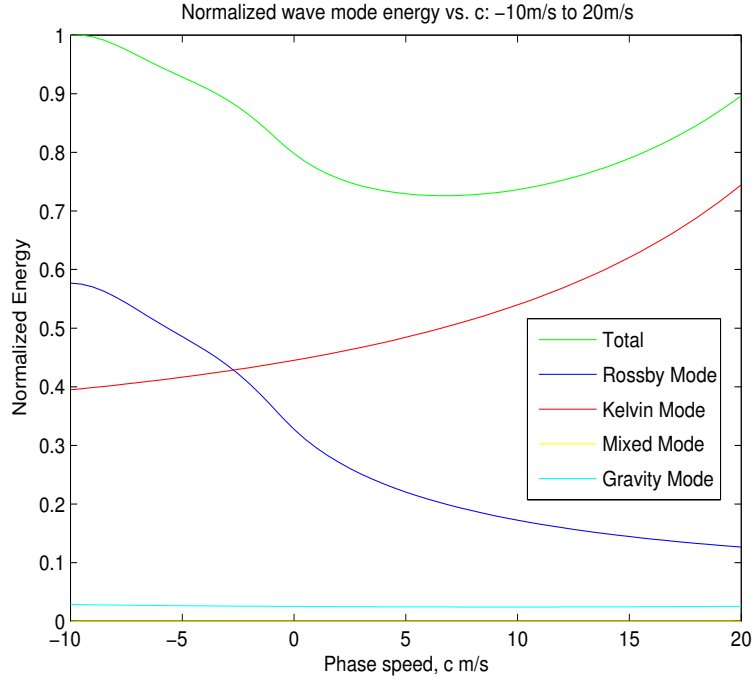


Figure 4.3: Normalized energy vs. propagation speed (c) of forcing.

In the next plot, the zonal halfwidth (a_0) and meridional e-folding width (b_0) are varied simultaneously ($\pi a_0 b_0$ remains fixed). The total response energy increases from $(a_0, b_0) = (500\text{km}, 1125\text{km})$ to a maximum at $(a_0, b_0) \approx (1000\text{km}, 562.5\text{km})$, and then steadily decreases. As a_0 increases and b_0 decreases the Kelvin component of energy increases to a maximum at $(a_0, b_0) \sim (2000\text{km}, 300\text{km})$, from which point the energy slowly decreases. The Rossby component of energy decreases as b_0 decreases and a_0 increases.

The last of the variable convective forcing parameters is the phase speed (c). Fig. 4.3 shows energy vs. phase speed, the values of which span from westward travel at 10 m s^{-1} to eastward travel at 20 m s^{-1} . The total energy exhibits a minimum in this range and the Rossby contribution is seen to decrease with increasing c while the Kelvin contribution

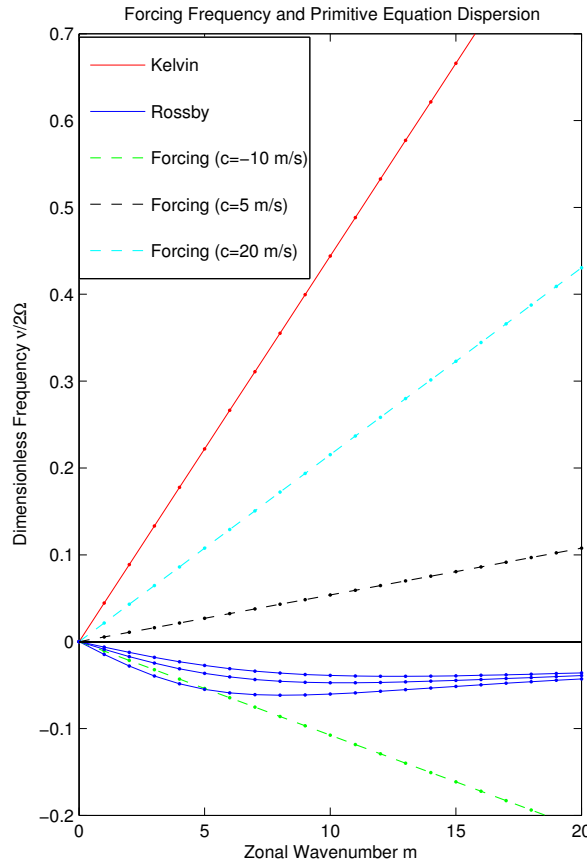


Figure 4.4: Dispersion diagram for the dimensionless frequencies: Kelvin ($\hat{\nu}_{m,-1,2}$), Rossby ($\hat{\nu}_{m,n,0}$, where $n = 1, 2, 3$), and forcing ($\hat{\nu}_m$, where $c = -10, 5, 20 \text{ ms}^{-1}$) vs. m .

increases with increasing c . An explanation for this behavior can be seen by returning to (4.20) and remembering that $\hat{\nu}_m = c(m/a)$ is the frequency of the convective forcing. Refer also to Fig. 4.4, which is a dispersion diagram for the Kelvin and Rossby modes plus some additional curves for the forcing frequency when $c = -10, 5$, and 20 ms^{-1} . The Rossby component of energy is the largest when $c = -10 \text{ ms}^{-1}$, which gives a forcing frequency close to the Rossby frequencies. When $c = 20 \text{ ms}^{-1}$, the Kelvin response experiences the highest resonance. The minimum in total energy is observed when the forcing frequency lies between the Kelvin and Rossby frequencies such that the resonance of both modes are simultaneously minimized. The minimum in Fig. 4.4 occurs at $c \approx 6.7 \text{ ms}^{-1}$.

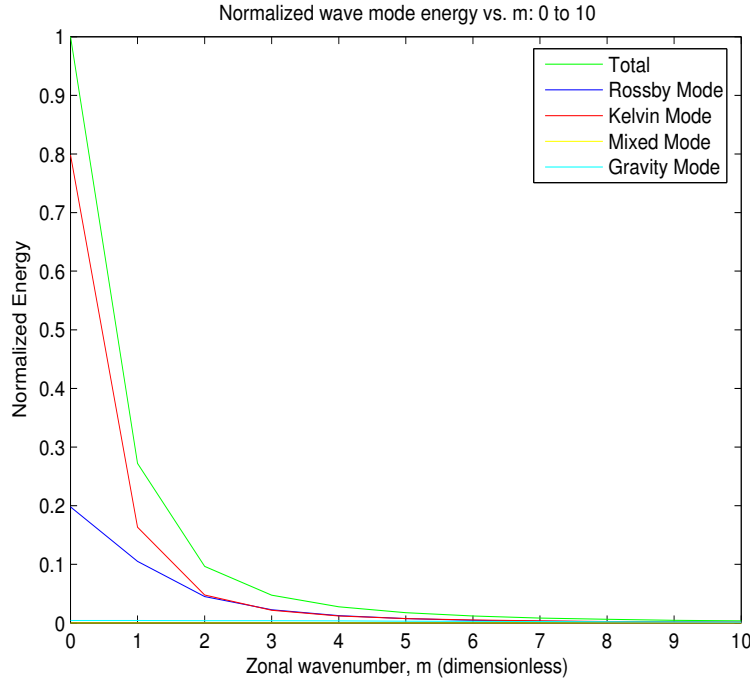


Figure 4.5: Normalized energy vs. zonal wavenumber (m).

Fig. 4.5 shows normalized energy plotted against zonal wavenumbers 1–10. The energy is maximized at the zonal mean state, decreases rapidly in the first few wave numbers, then continues to get smaller and becomes essentially negligible within the plotted wavenumber range. The zonal scale suggested by the total energy spectrum agrees with those assumed in studies of the MJO using spatial filtering (Wheeler and Kiladis, 1999; Kemball-Cook and Weare, 2001). The energy distribution over zonal wavenumbers is illustrated in the circulation fields of Fig. 4.6. Here the total flow response associated with a specific wavenumber ($m = 0, 1, \dots, 6$) is plotted. The equatorial trough zone is resolved in the zonal average, and the circulation pattern bearing the most resemblance to the full solution is found in the wavenumber 1 panel. Wavenumbers 2–6 contain decreasing, small amplitude fluxuations about zero. This distribution can be explained in part by the resonance term in (4.20). Referring to Fig. 4.4, for $c = 5 \text{ m s}^{-1}$, as m increases the frequency of forcing ($\tilde{\nu}_m$) deviates further from both the Kelvin and Rossby frequencies. In this way the phase speed of the forcing plays a role in the energy distribution over zonal length scales,

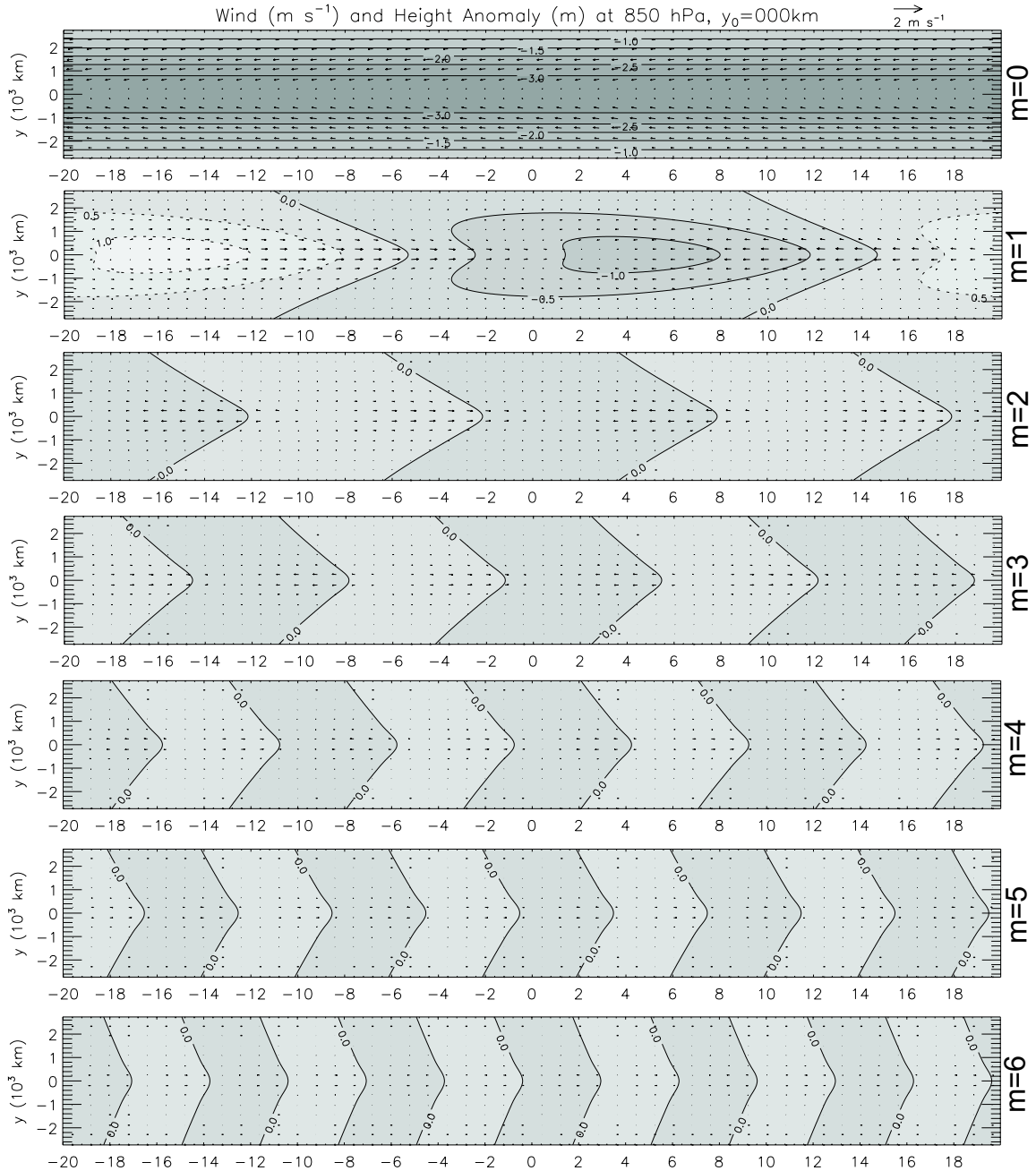


Figure 4.6: Total circulation field solutions using the default parameters plotted over the entire zonal domain, associated with wavenumbers $m = 0$ through $m = 6$.

though it should not be forgotten that the dependence of \hat{Q}_{mnr} on m plays a role as well.

Chapter 5

CONCLUSIONS

5.1 Chapter 2 Summary

We have used a linear, equatorial β -plane, primitive equation model as a tool to investigate the large-scale wind and mass fields around a moving heat source near the equator. The prescribed heat source was formulated to coarsely simulate an eastward propagating MJO convective core region. The large-scale characteristics of this convective envelope were incorporated into the forcing by basing the propagation speed, horizontal dimensions, heating rate, and meridional position on estimated values from observational and reanalysis studies. Within the context of the assumed linear dynamics, the resulting solution fields have been decomposed into Rossby, mixed Rossby-gravity, inertia-gravity, and Kelvin modes. The Rossby modes are responsible for the flow pattern west of the moving convective envelope, Kelvin modes for the flow pattern east of the convection, and inertia-gravity modes for the divergent flow near the convection, with mixed Rossby-gravity modes playing a minor role when the convection is centered near the equator. Although the patterns produced here by the primitive equation model are qualitatively similar to those found using the long wave approximation (Gill, 1980; Heckley and Gill, 1984; Chao, 1987), they are more accurate because the long wave approximation distorts the dispersion relation for Rossby waves (e.g., Fig. 1 of Stevens et al., 1990). However, it can be inferred from the partitioning of energy by zonal wavenumbers in Chapter 4 that the longwave approximation is probably in good agreement with the exact solutions for the parameters we have used. This is seen by comparing Fig. 4.5 and Fig. 5.1. Fig. 4.5 shows the majority of the total energy is

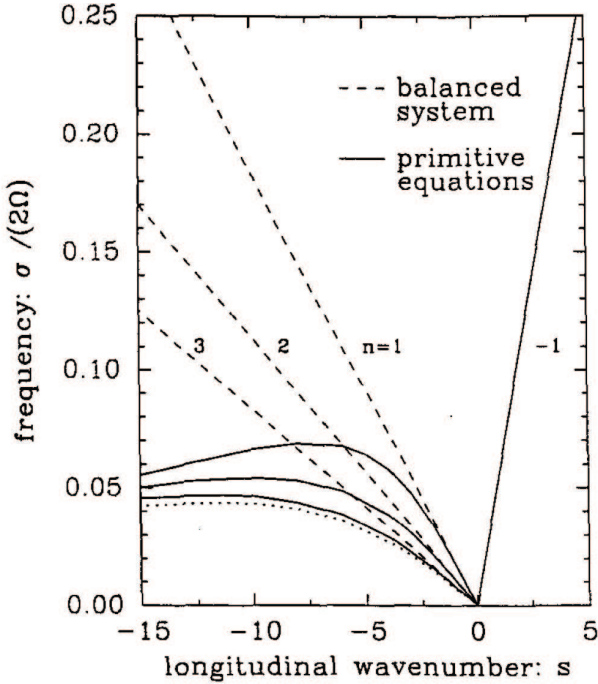


Figure 5.1: Reproduced from Stevens et al. 1990. The long-wave approximated (dashed) primitive equation Rossby wave frequencies (solid lines) are distorted for large magnitude zonal wavenumbers.

distributed over low zonal wavenumbers. Fig. 5.1 shows that the longwave frequencies are close to the exact Rossby frequencies for low zonal wavenumbers.

5.2 Chapter 3 Summary

A potential vorticity principle was derived from the governing set of equations solved in Chapter 2. From this local tendency equation, the PV was seen to increase due to diabatic heating and advection of planetary vorticity, while it decreased due to radiative and frictional dissipation. A factor of βy on the diabatic source term caused the generation of PV due to heating to be suppressed at the equator and maximized at the poleward edges of the simulated convection. The PV was then expressed in spectral space from which it was decomposed into contributions from the various equatorial wave types. The Kelvin PV contribution was seen to be identically zero while the inertia-gravity wave contribution was small, especially at higher wavenumbers. The temperature field of a mixed Rossby-

gravity wave is anti-symmetric about the equator so the contribution of this wave when the forcing is symmetric about the equator is identically zero. For small displacements from the equator the response is nonzero, but comparatively small. Because these modes contribute very little to the sum, the total PV field is essentially due to the Rossby component PV.

Through the use of an idealized PV principle involving only heating and dissipation, it was seen that the βv term plays an important role in increasing the strength and extent of the PV anomaly in both the poleward and westward directions. This idealized study also revealed that the magnitude of the PV anomaly trailing the convective region depends on τ_p/τ_c , the ratio of the passage time to the convective overturning time. The passage time τ_p is large if the convection moves slowly and has a large zonal extent, while the overturning time is small if the apparent heat source and surface rainfall are large. Such convection produces large PV anomalies and a large equatorial westerly wind burst in its wake. With increasing τ_p/τ_c nonlinear effects become important.

An equatorial invertibility principle was then proposed as a method to approximately recover the balanced wind and mass fields from the PV distribution. Comparing the circulation attained from inversion with that from the primitive equation model illustrates that the flow in the wake of an eastward moving equatorial convective envelope can be fairly accurately recovered from the PV, and is essentially described by balanced dynamics. The balance assumption used in the invertibility principle is valid on the entire equatorial domain, making it useful for study of the MJO.

It was also noted that the invertibility principle could be used in conjunction with an approximate PV principle to form a complete balanced theory. While the frequencies that resulted very closely approximate the primitive equation Rossby frequencies, the PV field was only 68% of that associated with the primitive equation field. The problem was seen to be in the approximation $\beta v \rightarrow \beta(\partial\psi/\partial x)$, which neglects the divergent flow that is important in advecting basic state PV. For this reason the invertibility principle is of more interest as a diagnostic tool assuming a known PV distribution.

5.3 Chapter 4 Summary

In the last chapter we derived a total energy principle for our system that reduced to an energy balance between dissipation and generation when we assume a steady state. A shallow water energy principle can be attained in the same way and the analogous steady state energy balance was given. The flow of energy through the system was then discussed by first introducing a generalization to the concept of group velocity for the case of discrete integer wavenumbers. From this generalization we showed that the energy generated in the small, localized, propagating convective region was carried (zonally) away from the source on either side and was then removed from the system by dissipation in the far field. Through this mechanism the derived steady state energy balance is maintained.

Next we found a Parseval relation which allowed the total energy of the system to be calculated by way of a truncated infinite sum in spectral space as opposed to evaluation of a physical space integral. Furthermore, we were able to decompose the energy into its contributions from each equatorial wave type.

We used this relation to evaluate the energy dependence on the convective forcing parameters. It was first established that the Rossby and Kelvin wave types gave the primary contributions to total energy. When the forcing ranged over meridional displacement values the total energy increased as the Rossby energy rapidly increased and the Kelvin energy slowly decreased. When the horizontal space parameters a_0 and b_0 were varied simultaneously such that the heating area remained constant, the total response energy attained a maximum near $(a_0, b_0) \sim (1000\text{km}, 550\text{km})$. The phase speed of the convective forcing was then varied, showing that the Rossby response energy decreases with increasing eastward speed and the Kelvin response energy increases. This effect was explained by resonance of the particular wave frequency with the forcing frequency.

The energy chapter concluded with a look at the normalized energy versus zonal wavenumber. The energy maximum was found at $m = 0$ and then decreased rapidly over the next few wavenumbers. This energy distribution was explained in part by noticing

that for the forcing phase speed of $c = 5 \text{ m s}^{-1}$, the resonance of both the Kelvin and Rossby modes decreased with increasing m . It was cautioned though that the dependence of \hat{Q}_{mnr} on m played a role as well. The high energy in the zonal average was seen to maintain the characteristic equatorial trough zone, and a coarse resolution of the combined Rossby-Kelvin pattern was evident in the $m = 1$ circulation field.

Appendix A

CONVERSION TO THE LOG-PRESSURE VERTICAL COORDINATE

Equations (2.1)–(2.4) are specific to a local cartesian plane using physical height (z) as the vertical coordinate. For later manipulation it is mathematically convenient to convert to the log-pressure vertical coordinate, $z^* = \ln(p_0/p)$.

In the horizontal momentum equations, (2.1) and (2.2), only the pressure gradient terms must be rewritten to be relevant in the z^* system. This is accomplished with the asserted substitutions

$$\frac{1}{\rho} \frac{\partial p}{\partial x} \Big)_z = \frac{\partial \phi}{\partial x} \Big)_{z^*}, \quad (\text{A.1})$$

$$\frac{1}{\rho} \frac{\partial p}{\partial y} \Big)_z = \frac{\partial \phi}{\partial y} \Big)_{z^*}, \quad (\text{A.2})$$

where $\phi = gz$ is the geopotential.

To put the hydrostatic equation (2.3) into the desired form for the z^* coordinate we start by rearranging it to contain the geopotential,

$$-\frac{1}{\rho} = \frac{\partial \phi}{\partial p}. \quad (\text{A.3})$$

Next, rearranging the above definition of z^* yields

$$p = p_0 e^{-z^*}, \quad (\text{A.4})$$

which can be used to find the log-pressure vertical coordinate derivative operator,

$$\frac{\partial}{\partial z^*} = -p \frac{\partial}{\partial p}. \quad (\text{A.5})$$

Multiply (A.3) by p and use (A.5) to arrive at

$$\frac{p}{\rho} = \frac{\partial \phi}{\partial z^*}. \quad (\text{A.6})$$

Use of the ideal gas law to write the left hand side of (A.6) in terms of temperature results in the form seen in (2.6).

It is easiest to convert the continuity equation starting in pressure coordinates,

$$\frac{\partial u}{\partial x} + \frac{\partial v}{\partial y} + \frac{\partial \omega}{\partial p} = 0, \quad (\text{A.7})$$

which is a simple step from (2.4). The pressure coordinate form of the horizontal divergence readily transforms to the z^* coordinate through the relationships

$$\left. \frac{\partial u}{\partial x} \right)_p = \left. \frac{\partial u}{\partial x} \right)_{z^*}, \quad \left. \frac{\partial v}{\partial y} \right)_p = \left. \frac{\partial v}{\partial y} \right)_{z^*}. \quad (\text{A.8})$$

Noting that $\omega = Dp/Dt$ and using the expression (A.4) for pressure, ω can be written as

$$\omega = -pw^*, \quad (\text{A.9})$$

where

$$w^* = \frac{Dz^*}{Dt}. \quad (\text{A.10})$$

Using (A.5) and (A.9) in the term $\partial\omega/\partial p$ results in

$$\frac{\partial \omega}{\partial p} = \frac{\partial w^*}{\partial z^*} - w^*, \quad (\text{A.11})$$

which concludes the transformation of the continuity equation.

The thermodynamic equation (2.5) is not restricted to any particular reference frame so no conversion is needed. However, we will rewrite it to contain the quantity w^* which was defined by (A.10). Inserting $z^* = \ln(p_0/p)$ into (A.10) leads to an alternative definition

$$w^* = -\frac{1}{p} \frac{Dp}{Dt}. \quad (\text{A.12})$$

Using this along with the ideal gas law in the second term on the left hand side of (2.5) yields a new form of the thermodynamic equation,

$$c_p \frac{DT}{Dt} + RTw^* = \mathcal{D}. \quad (\text{A.13})$$

At this point the system (2.1)–(2.4) has been converted to a set of equations relevant in the z^* vertical coordinate space. From here the system (2.6) is attained by linearizing these new equations about a basic resting state. It is important to point out that the field variables in (2.6) are perturbation quantities, although the (')'s have been dropped to keep the notation clean. For the same reason the (*)'s are dropped, so the log-pressure vertical coordinate context should be kept in mind in their absence.

Appendix B

VERTICAL NORMAL MODE TRANSFORM

Separation of the horizontal and vertical structure in (2.6) is accomplished by designing an integral transform that will eliminate the vertical derivatives (Fulton and Schubert, 1985). The kernel ($\Psi_\ell(z)$) of this transform is initially unspecified and is determined by solving the eigenvalue-eigenfunction problem it will be required to satisfy. Define $\phi_\ell(x, y, t)$, the vertical integral transform of $\phi(x, y, z, t)$ by

$$\phi_\ell(x, y, t) = \int_0^{z_T} \phi(x, y, z, t) \Psi_\ell(z) e^{-z/2} dz, \quad (\text{B.1})$$

where $e^{-z/2}$ is the weight.

When our continuously stratified, compressible atmosphere is in the basic resting state it is completely described by the hydrostatic equation, continuity equation, and unforced thermodynamic equation,

$$\frac{\partial \phi}{\partial z} = RT, \quad (\text{B.2})$$

$$\frac{\partial u}{\partial x} + \frac{\partial v}{\partial y} + \frac{\partial w}{\partial z} - w = 0, \quad (\text{B.3})$$

$$\frac{\partial T}{\partial t} + \Gamma w = 0. \quad (\text{B.4})$$

These can be combined into a single equation that contains all the vertical derivatives associated with (2.6),

$$e^z \frac{\partial}{\partial z} \left[\frac{e^{-z}}{R\Gamma} \frac{\partial}{\partial z} \left(\frac{\partial \phi}{\partial t} \right) \right] - \left(\frac{\partial u}{\partial x} + \frac{\partial v}{\partial y} \right) = 0. \quad (\text{B.5})$$

To find $\Psi_\ell(z)$, the intrinsic vertical modes, apply the constructed transform to (B.5),

$$\int_0^{z_T} e^z \frac{\partial}{\partial z} \left[\frac{e^{-z}}{R\Gamma} \frac{\partial}{\partial z} \left(\frac{\partial \phi}{\partial t} \right) \right] \Psi_\ell(z) e^{-z/2} dz - \int_0^{z_T} \left(\frac{\partial u}{\partial x} + \frac{\partial v}{\partial y} \right) \Psi_\ell(z) e^{-z/2} dz = 0. \quad (\text{B.6})$$

Assuming transforms $u_\ell(x, y, t)$ and $v_\ell(x, y, t)$ similar to (B.1) exist for $u(x, y, z, t)$ and $v(x, y, z, t)$, then (B.6) becomes

$$\underbrace{\int_0^{z_T} e^z \frac{\partial}{\partial z} \left[\frac{e^{-z}}{R\Gamma} \frac{\partial}{\partial z} \left(\frac{\partial \phi}{\partial t} \right) \right] \Psi_\ell(z) e^{-z/2} dz - \left(\frac{\partial u_\ell}{\partial x} + \frac{\partial v_\ell}{\partial y} \right)}_{I_1} = 0. \quad (\text{B.7})$$

The horizontal divergence has been transformed so only the first term (denoted by I_1 for convenience) needs attention. Using integration by parts on I_1 twice gives

$$I_1 = \int_0^{z_T} \frac{\partial \phi}{\partial t} \frac{\partial}{\partial z} \left[\frac{e^{-z}}{R\Gamma} \frac{\partial}{\partial z} \left(\Psi_\ell(z) e^{z/2} \right) \right] dz - \left[\frac{e^{-z}}{R\Gamma} \left\{ \frac{\partial}{\partial z} \left(\Psi_\ell(z) e^{z/2} \right) \frac{\partial \phi}{\partial t} - \Psi_\ell(z) e^{z/2} \frac{\partial}{\partial z} \left(\frac{\partial \phi}{\partial t} \right) \right\} \right]_{z=0}^{z=z_T}. \quad (\text{B.8})$$

Section 2.1 gave upper and lower model boundary conditions $w = 0$ at $z = z_T, 0$. Enforcing these for (B.4) together with (B.2) implies that $\frac{\partial}{\partial z} \left(\frac{\partial \phi}{\partial t} \right) = 0$ at $z = z_T, 0$, which eliminates the last term in (B.8),

$$I_1 = \int_0^{z_T} \frac{\partial \phi}{\partial t} \left\{ e^{z/2} \frac{\partial}{\partial z} \left[\frac{e^{-z}}{R\Gamma} \frac{\partial}{\partial z} \left(\Psi_\ell(z) e^{z/2} \right) \right] \right\} e^{-z/2} dz - \left[\frac{e^{-z}}{R\Gamma} \frac{\partial \phi}{\partial t} \left\{ \frac{\partial}{\partial z} \left(\Psi_\ell(z) e^{z/2} \right) \right\} \right]_{z=0}^{z=z_T}. \quad (\text{B.9})$$

Now impose conditions on the two terms contained in $\{ \}$ (which we are allowed to do as $\Psi_\ell(z)$ is yet unspecified) so that I_1 will yield the transform of $\partial \phi / \partial t$, as desired. This will in fact occur if the entire second term disappears (require second term in $\{ \}$ to vanish at boundaries), and if the entire first term is proportional to $\int_0^{z_T} (\partial \phi / \partial t) \Psi_\ell(z) e^{-z/2} dz$ (insist first term in $\{ \}$ is proportional to $\Psi_\ell(z)$). These conditions,

$$e^{z/2} \frac{d}{dz} \left[\frac{e^{-z}}{R\Gamma} \frac{d}{dz} \left(\Psi_\ell(z) e^{z/2} \right) \right] = -\frac{1}{\bar{c}_\ell^2} \Psi_\ell(z), \quad (\text{B.10})$$

$$\left. \frac{d}{dz} \left(\Psi_\ell(z) e^{z/2} \right) \right|_{z=0, z_T} = 0, \quad (\text{B.11})$$

form a Sturm-Liouville eigenproblem. The set of eigenfunction solutions ($\Psi_\ell(z)$) are known to be orthogonal and complete, and can thus be used as a basis for the inverse transform. An example of the inverse transform is

$$\phi(x, y, z, t) = \sum_{\ell=1}^{\infty} \phi_\ell(x, y, t) \Psi_\ell(z) e^{z/2}, \quad (\text{B.12})$$

which forms a transform pair with (B.1). Define the total vertical structure in (B.12) as

$$Z_\ell(z) = \Psi_\ell(z) e^{z/2}, \quad (\text{B.13})$$

and use it to rewrite (B.10) as

$$\left(\frac{d}{dz} - 1\right) \frac{d}{dz} Z_\ell(z) = -\frac{R\Gamma}{\bar{c}_\ell^2} Z_\ell(z). \quad (\text{B.14})$$

Substituting the known general solution for the internal modes ($Z_\ell(z) = e^{z/2}[A \cos(\gamma_\ell z) + B \sin(\gamma_\ell z)]$, where $\gamma_\ell^2 = [R\Gamma/\bar{c}_\ell^2 - 1/4]$ and $\ell = 1, 2, 3, \dots$) in (B.14) and applying the boundary conditions determines the eigenvalues,

$$\frac{1}{\bar{c}_\ell^2} = \frac{1}{R\Gamma} \left(\frac{\ell^2\pi^2}{z_T^2} + \frac{1}{4} \right). \quad (\text{B.15})$$

Using (B.15) in (B.14) and (B.13) in (B.11) the Sturm-Liouville problem takes the form seen in section 2.2,

$$\left(\frac{d}{dz} - 1\right) \frac{d}{dz} Z_\ell(z) = -\left(\frac{\ell^2\pi^2}{z_T^2} + \frac{1}{4}\right) Z_\ell(z), \quad (\text{B.16})$$

$$\frac{d}{dz} Z_\ell(z) \Big|_{z=0} = \frac{d}{dz} Z_\ell(z) \Big|_{z=z_T} = 0. \quad (\text{B.17})$$

From here $Z_\ell(z)$ for any $\ell = 1, 2, 3, \dots$ can easily be found from (B.16) and (B.17), though as discussed in section 2.2, only $Z(z) \equiv Z_1(z)$ is necessary for this study. As a result the inverse transform for the variables $u(x, y, z, t)$, $v(x, y, z, t)$, and $\phi(x, y, z, t)$ reduces to

$$\begin{pmatrix} u(x, y, z, t) \\ v(x, y, z, t) \\ \phi(x, y, z, t) \end{pmatrix} = \begin{pmatrix} \hat{u}(x, y, t) \\ \hat{v}(x, y, t) \\ \hat{\phi}(x, y, t) \end{pmatrix} Z(z), \quad (\text{B.18})$$

where the $(\hat{\cdot})$'s denote the lack of vertical dependence. Use of (B.18) in the hydrostatic equation for $\phi(x, y, z, t)$ shows that to be consistent, T must have vertical structure given by $Z'(z) \equiv (d/dz)Z(z)$. Substituting this structure for T in the forced thermodynamic equation shows w and Q must have this structure as well. In summary,

$$\begin{pmatrix} T(x, y, z, t) \\ w(x, y, z, t) \\ Q(x, y, z, t) \end{pmatrix} = \begin{pmatrix} \hat{T}(x, y, t) \\ \hat{w}(x, y, t) \\ \hat{Q}(x, y, t) \end{pmatrix} Z'(z), \quad (\text{B.19})$$

The expressions given in (B.18) and (B.19) give us the ability to separate the vertical and horizontal structure in equations (2.6).

Appendix C

TRANSFORMATION TO THE ξ -COORDINATE

Define new time and zonal distance variables as

$$\tau = t, \quad \xi = x - ct, \quad (\text{C.1})$$

respectively. Note that to remain at the same point in ξ as t increases, it is necessary to move eastward at a constant rate c . To perform the transformation $(x, t) \rightarrow (\xi, \tau)$ on our set of equations, a relationship between the derivative operators of each coordinate frame is needed. The necessary relationships can be attained by expanding the x and t derivative operators in terms of ξ and τ using the chain rule

$$\frac{\partial}{\partial t} = \frac{\partial \xi}{\partial t} \frac{\partial}{\partial \xi} + \frac{\partial \tau}{\partial t} \frac{\partial}{\partial \tau}, \quad (\text{C.2})$$

$$\frac{\partial}{\partial x} = \frac{\partial \xi}{\partial x} \frac{\partial}{\partial \xi} + \frac{\partial \tau}{\partial x} \frac{\partial}{\partial \tau}. \quad (\text{C.3})$$

The derivative terms evaluate to, $\partial \xi / \partial t = -c$, $\partial \tau / \partial t = 1$, $\partial \xi / \partial x = 1$, and $\partial \tau / \partial x = 0$, which reduces (C.2) and (C.3) to $\partial / \partial t = -c \partial / \partial \xi + \partial / \partial \tau$ and $\partial / \partial x = \partial / \partial \xi$, respectively. If we can assume that the flow does not change in time, τ , as seen from a reference frame translating at the same constant speed as the forcing (c), then mathematically we have that $\partial F / \partial \tau = 0$, for any field variable F . Applying this “steady state assumption” to the expression for the t derivative operator the final form of (C.2) and (C.3) becomes

$$\frac{\partial}{\partial x} = \frac{\partial}{\partial \xi}, \quad (\text{C.4})$$

$$\frac{\partial}{\partial t} = -c \frac{\partial}{\partial \xi}, \quad (\text{C.5})$$

which are the same forms seen in section 2.4.

Appendix D

EIGENFUNCTIONS FOR ZONALLY SYMMETRIC ROSSBY MODES

For the zonally symmetric Rossby modes (i.e., for $m = 0, n > 0, r = 0$), the eigenfunction formula (2.28) is indeterminant because both m and $\hat{\nu}_{0n0}$ vanish. However, orthonormal eigenfunctions are easily constructed in this case by considering m as continuous and applying l'Hospital's rule for the limit $m \rightarrow 0$. The eigenfunctions for the zonally symmetric Rossby modes are then given by

$$\mathbf{K}_{0n0}(\hat{y}) = (2n + 1)^{-\frac{1}{2}} \begin{pmatrix} \left[\left(\frac{n}{2} \right)^{\frac{1}{2}} \mathcal{H}_{n+1}(\hat{y}) - \left(\frac{n+1}{2} \right)^{\frac{1}{2}} \mathcal{H}_{n-1}(\hat{y}) \right] \\ 0 \\ \bar{c} \left[\left(\frac{n}{2} \right)^{\frac{1}{2}} \mathcal{H}_{n+1}(\hat{y}) + \left(\frac{n+1}{2} \right)^{\frac{1}{2}} \mathcal{H}_{n-1}(\hat{y}) \right] \end{pmatrix}. \quad (\text{D.1})$$

Using (2.35) it can easily be confirmed that the zonally symmetric eigenfunctions (D.1) satisfy the orthonormality condition (2.34). Using (2.30) and (2.31) it is also easily confirmed that the eigenfunctions (D.1) correspond to geostrophically balanced zonal flows.

Appendix E

MERIDIONAL NORMAL MODE TRANSFORM OF THE HEATING FUNCTION

Using the definition of $\hat{\mathbf{Q}}_m(y)$ given by (2.24) and (2.22), the inner product definition (2.25), and the formula (2.28) for the kernel $\mathbf{K}_{mnr}(\hat{y})$, we can write the inner product $\hat{Q}_{mnr} = (\hat{\mathbf{Q}}_m, \mathbf{K}_{mnr})$ as integrals of $\exp[-(\hat{y} - \hat{y}_0)^2/\hat{b}_0^2]\mathcal{H}_{n+1}(\hat{y})$ and $\exp[-(\hat{y} - \hat{y}_0)^2/\hat{b}_0^2]\mathcal{H}_{n-1}(\hat{y})$. These integrals can be evaluated using the following result from Gradshteyn and Ryzhik (1994, page 843):

$$\int_{-\infty}^{\infty} \exp\left[-\frac{(\hat{y} - \hat{y}_0)^2}{\hat{b}_0^2}\right] \mathcal{H}_n(\hat{y}) d\hat{y} = \left(\frac{2\pi\hat{b}_0^2}{2 + \hat{b}_0^2}\right)^{\frac{1}{2}} \left(\frac{2 - \hat{b}_0^2}{2 + \hat{b}_0^2}\right)^{\frac{n}{2}} \exp\left[\frac{\hat{b}_0^2\hat{y}_0^2}{4 - \hat{b}_0^4}\right] \mathcal{H}_n\left(\frac{2\hat{y}_0}{(4 - \hat{b}_0^4)^{\frac{1}{2}}}\right), \quad (\text{E.1})$$

for $0 \leq \hat{b}_0 < 2^{\frac{1}{2}}$.

Appendix F

COMPUTATIONAL PROCEDURE

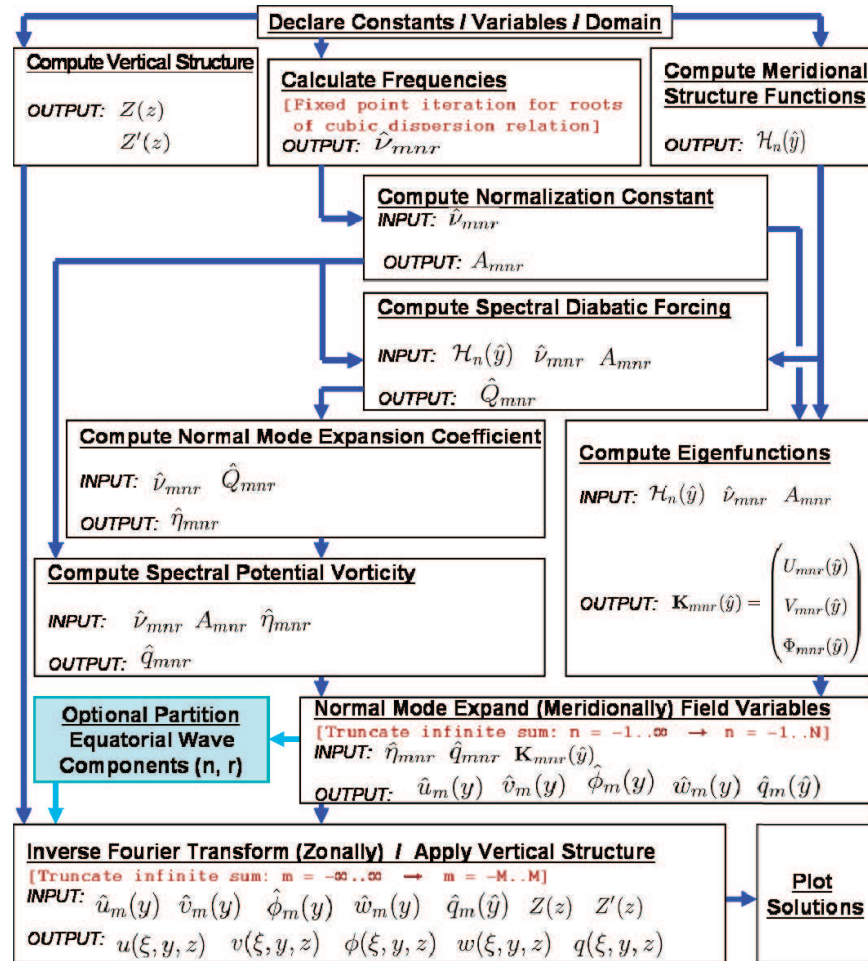


Figure F.1: A schematic showing the procedure for computing the primitive equation solutions. The red text marks steps that use a numerical approximation to the exact solution. All plots presented in this study use the truncation values of $M = 200$ and $N = 200$. The alternate light blue path denotes the ability to partition the total solution into its equatorial wave components by summing over the relevant indicies (n, r) for a specific wave mode, type.

Appendix G

IDEALIZED PV PRINCIPLE SOLUTION

Neglecting the advection of basic state PV and assuming the flow is steady when viewed from a reference frame moving with the forcing, the primitive equation PV principle is

$$c \frac{\partial q}{\partial \xi} = \alpha q - \frac{\beta y}{c_p \Gamma} \left(\frac{\partial}{\partial z} - 1 \right) Q. \quad (\text{G.1})$$

Referring back to section 2.2, the separable forms shown in (2.12) along with equation (2.8) when $\ell = 1$ (recall $Z(z) \equiv Z_1(z)$) allow separation of the vertical structure from (G.1). Then multiplying by the integrating factor $e^{-(\alpha/c)\xi}$, and rearranging modifies (G.1) to

$$\frac{\partial}{\partial \xi} \left(e^{-\frac{\alpha}{c}\xi} \hat{q} \right) = \frac{1}{c} \frac{\beta y}{c^2} \kappa \hat{Q} e^{-\frac{\alpha}{c}\xi}, \quad (\text{G.2})$$

where \hat{Q} is given by (2.15). In a zonally infinite domain \hat{Q} is defined piecewise over three subdomains. The PV field for the entire domain is found by integrating (G.2) over each subdomain, then joining the relevant pieces together by requiring that the solutions and their derivatives match at both subdomain interfaces. The boundary conditions imposed are $\hat{q}(\xi, y) \rightarrow 0$ as $\xi \rightarrow \pm\infty$. After reapplying the vertical structure $Z(z)$ given by (2.10), the piecewise definition of this idealized PV distribution is

$$q(\xi, y, z) = -\frac{\tau_p}{\tau_c} \left(\frac{\pi^2}{\pi^2 + \alpha^2 \tau_p^2} \right) F(\xi) \beta y \exp \left[-\left(\frac{y - y_0}{b_0} \right)^2 \right] Z(z), \quad (\text{G.3})$$

$$F(\xi) = \begin{cases} \frac{\sinh[(\alpha/c)a_0]}{(\alpha/c)a_0} \exp[(\alpha/c)\xi] & -\infty < \xi \leq -a_0, \\ \frac{1 - \exp[-(\alpha/c)(a_0 - \xi)]}{2(\alpha/c)a_0} + \frac{\alpha a_0}{2\pi^2 c} [1 + \cos(\pi\xi/a_0)] - \frac{1}{2\pi} \sin(\pi\xi/a_0) & -a_0 \leq \xi \leq a_0, \\ 0 & a_0 \leq \xi < \infty. \end{cases}$$

Appendix H

EQUATORIAL BALANCE RELATION

As shown in section 3.3, assuming that βy varies slowly compared to ψ , the linear balance relation given by (3.16) reduces to (3.17),

$$\nabla^2(\beta y \psi) = \nabla^2 \phi. \quad (\text{H.1})$$

Combining terms and letting $F = (\phi - \beta y \psi)$, (H.1) can be written as

$$\nabla^2 F = 0. \quad (\text{H.2})$$

The Fourier ξ -transform of (H.2) is found to be,

$$\frac{d^2 F_m}{dy^2} - \frac{m^2}{a^2} F_m = 0, \quad (\text{H.3})$$

by using a Fourier transform pair similar to (2.19) for $F(x, y)$. The general solution of this second order ODE is

$$F_m(y) = A e^{\frac{m}{a}y} + B e^{-\frac{m}{a}y}, \quad (\text{H.4})$$

which must satisfy our imposed boundary conditions $F \rightarrow 0$ as $y \rightarrow \pm\infty$. Because $e^{(m/a)y} \rightarrow \infty$ as $y \rightarrow \infty$, it's required that $A = 0$. Similarly, the other boundary condition requires that $B = 0$, leaving only the trivial solution

$$F_m = 0. \quad (\text{H.5})$$

Inverse Fourier transforming (H.5) and then using the definition of F yields the equatorial balance relation (3.18),

$$\phi = \beta y \psi. \quad (\text{H.6})$$

Appendix I

GROUP VELOCITY CONCEPTS FOR DISCRETE WAVENUMBERS

By Fourier analysis a complex wave disturbance of sufficiently small amplitude can be represented by a linear combination of different sinusoidal waves (Lighthill, 1978). If this complex waveform has a phase speed that is independent of wavelength, then the simple harmonic components will all be moving at the same speed and the complex waveform will maintain its shape as it travels. In this case the wave is considered to be non-dispersive, and the associated wave energy travels with the phase speed. However, if the phase speed depends on the wavelength then the simple harmonic components will each travel at different speeds, thus changing the shape of the complex waveform as it travels. In this case the waveform is considered to be dispersive, and the associated wave energy does not travel with the phase speed.

For a dispersive wave the associated energy propagates in the direction of the group velocity vector, which can be shown to be the gradient of the frequency in wavenumber space (Kundu and Cohen, 2004). However, when the wavenumbers are restricted to be discrete, this form of the group velocity vector is not definable. By following the analysis of Hoskins et al. (1977) we can derive a speed at which the energy propagates in this situation. This speed can be seen as a generalization of the group velocity concept to a discretized wavenumber space. The idea is to look at the interaction between two simple harmonic wave components that have the same amplitude, but have wavenumbers m_1 and m_2 that differ by a small amount. Because dispersive waves are of interest here, we will assume these waves propagate at different speeds due to their different wavelengths. Linear superposition states

the interaction between these two waves is additive. So when the two waves are 180° out of phase the interference is completely destructive and the resulting waveform amplitude is zero. When the waves are exactly in phase, the interference is constructive and the amplitude is maximized. Due to their different phase speeds, these two harmonic wave components will periodically pass through the spectrum of interference positions, yielding a combined periodic waveform with amplitude that is dependent on the interference. The result is a waveform that appears as propagating “wave packets”, which are delimited by the nodes, or points of zero amplitude. These “wave packets” or “groups” travel at a speed we will call \mathcal{C} . Because the associated wave energy cannot pass through the nodal points (Kundu and Cohen, 2004), and the nodal points travel at \mathcal{C} , then the wave energy travels at \mathcal{C} as well. In the limit as $m_1 \rightarrow m_2$, then $\mathcal{C} \rightarrow c_g$, or group velocity as it is commonly defined. For this reason we will interpret \mathcal{C} as a generalization of group velocity to a discrete wavenumber space.

The two interacting sinusoids described above can be written as $\cos(m_1x - \omega_1t)$ and $\cos(m_2x - \omega_2t)$, where $2\pi/m_1 > 2\pi/m_2$. Since our interest is in finding an expression for the speed at which the resulting wave packets travel, we can start by finding the distance and time over which its peak amplitude or nodes repeat. Let $t = t_0$ be the intial time when the waves are in phase at $x = x_0$, at which point the wave group has a peak amplitude. Then let (x_1, t_1) be the next point at which the waves are in phase. The time over which it takes a wave group peak amplitude to repeat itself is then $\Delta t = t_1 - t_0$ and the distance over which this occurs is $\Delta x = x_1 - x_0$. When the difference between the wavelengths equals the difference in the distance traveled,

$$\left(\frac{2\pi}{m_1} - \frac{2\pi}{m_2} \right) = \left(\frac{\omega_2}{m_2} - \frac{\omega_1}{m_1} \right) \Delta t,$$

and the difference in periods equals the difference in travel times,

$$\left(\frac{2\pi}{\omega_1} - \frac{2\pi}{\omega_2} \right) = \left(\frac{m_1}{\omega_1} - \frac{m_2}{\omega_2} \right) \Delta x,$$

the waves will be in phase at (x_1, t_1) . The above conditions can be solved for Δt and Δx

respectively, and are given by

$$\Delta t = 2\pi \frac{m_2 - m_1}{\omega_2 m_1 - \omega_1 m_2}, \quad (\text{I.1})$$

$$\Delta x = 2\pi \frac{\omega_2 - \omega_1}{\omega_2 m_1 - \omega_1 m_2}. \quad (\text{I.2})$$

From the physical reasoning above, it makes sense to define a speed that dispersive wave energy propagates at in a discrete wavenumber space as,

$$\mathcal{C} = \frac{\Delta x}{\Delta t} = \frac{\omega_2 - \omega_1}{m_2 - m_1}. \quad (\text{I.3})$$

Taking the limit of \mathcal{C} as the discrete wavenumbers approach a continuous spectrum,

$$c_g = \lim_{m_1 \rightarrow m_2} \left(\frac{\omega_2 - \omega_1}{m_2 - m_1} \right) = \frac{\partial \omega}{\partial m}, \quad (\text{I.4})$$

which is seen to be the standard definition of group velocity in the positive m direction.

BIBLIOGRAPHY

- Benedict, J. J., and D. A. Randall, 2007: An analysis of the MJO guided by TRMM rainfall data. *J. Atmos. Sci.*, submitted.
- Chao, W. C., 1987: On the origin of the tropical intraseasonal oscillation. *J. Atmos. Sci.*, **44**, 1940–1949.
- DeMaria, M., 1985: Linear response of a stratified tropical atmosphere to convective forcing. *J. Atmos. Sci.*, **42**, 1944–1959.
- Emanuel, K. A., 1987: An air-sea interaction model of intraseasonal oscillations in the tropics. *J. Atmos. Sci.*, **44**, 2324–2340.
- Fulton, S. R., and W. H. Schubert, 1985: Vertical normal mode transforms: Theory and application. *Mon. Wea. Rev.*, **113**, 647–658.
- Gill, A. E., 1980: Some simple solutions for heat-induced tropical circulation. *Quart. J. Roy. Meteor. Soc.*, **106**, 447–462.
- Gradshteyn, I. S., and I. M. Ryzhik, 1994: *Table of Integrals, Series, and Products*. 5th ed., Academic Press, New York.
- Harris, K. A., 1999: The barotropic response of the global atmosphere to large-scale tropical convective forcing. Master’s thesis, Colorado State University, Department of Atmospheric Science.
- Hausman, S. A., K. V. Ooyama, and W. H. Schubert, 2006: Potential vorticity structure of simulated hurricanes. *J. Atmos. Sci.*, **62**, 87–108.
- Heckley, W. A., and A. E. Gill, 1984: Some simple analytical solutions to the problem of forced equatorial long waves. *Quart. J. Roy. Meteor. Soc.*, **110**, 203–217.
- Hendon, H. H., and B. Liebmann, 1994: Organization of convection within the Madden-Julian oscillation. *J. Geophys. Res.*, **99**, 8073–8083.
- Hendon, H. H., and M. L. Salby, 1994: The life cycle of the Madden-Julian oscillation. *J. Atmos. Sci.*, **51**, 2225–2237.
- Hoskins, B. J., A. J. Simmons, and D. G. Andrews, 1977: Energy dispersion in a barotropic atmosphere. *Quart. J. Roy. Meteor. Soc.*, **103**, 553–567.
- Hu, Q., and D. A. Randall, 1994: Low-frequency oscillations in radiative-convective systems. *J. Atmos. Sci.*, **51**, 1089–1099.

- Johnson, R. H., and P. E. Ciesielski, 2000: Rainfall and radiative heating rates from the TOGA COARE atmospheric budgets. *J. Atmos. Sci.*, **57**, 1497–1514.
- Kemball-Cook, S. R., and B. C. Weare, 2001: The onset of convection in the Madden-Julian oscillation. *J. Climate*, **14**, 780–793.
- Kiladis, G. N., K. H. Straub, and P. T. Haertel, 2005: Zonal and vertical structure of the Madden-Julian oscillation. *J. Atmos. Sci.*, **62**, 2790–2809.
- Kundu, P. K., and I. M. Cohen, 2004: *Fluid Mechanics*. 3rd ed., Elsevier Academic Press.
- Lau, K.-M., and L. Peng, 1987: Origin of low-frequency (intraseasonal) oscillations in the tropical atmosphere. Part I: Basic theory. *J. Atmos. Sci.*, **44**, 950–972.
- Lau, W. K., and D. E. Waliser, Eds., 2005: *Intraseasonal Variability in the Atmosphere-Ocean Climate System*. Springer-Praxis, Chichester, UK.
- Lighthill, J., 1978: *Waves in Fluids*. Cambridge University Press.
- Lin, J.-L., M. Zhang, and B. Mapes, 2005: Zonal momentum budget of the Madden-Julian oscillation: The source and strength of equivalent linear damping. *J. Atmos. Sci.*, **62**, 2172–2188.
- Lin, X., and R. H. Johnson, 1996: Heating, moistening, and rainfall over the western Pacific warm pool during TOGA COARE. *J. Atmos. Sci.*, **53**, 3367–3383.
- Madden, R. A., and P. R. Julian, 1971: Detection of a 40-50 day oscillation in the zonal wind in the tropical Pacific. *J. Atmos. Sci.*, **28**, 702–708.
- Madden, R. A., and P. R. Julian, 1972: Description of global scale circulation cells in the tropics with a 40-50 day period. *J. Atmos. Sci.*, **29**, 1109–1123.
- Madden, R. A., and P. R. Julian, 1994: Observations of the 40-50 day tropical oscillation — a review. *Mon. Wea. Rev.*, **122**, 814–837.
- Madden, R. A., and P. R. Julian, 2005: *Intraseasonal Variability in the Atmosphere-Ocean Climate System*, chap. 1: Historical perspective. Springer-Praxis, Chichester, UK, 1–18. (Eds.) William K.M. Lau and Duane E. Waliser.
- Matsuno, T., 1966: Quasi-geostrophic motions in the equatorial area. *J. Meteor. Soc. Japan*, **44**, 25–43.
- Matthews, A., webpage content: MJO OLR Animation. School of Environmental Sciences, University of East Anglia. <http://envam1.env.uea.ac.uk/~e058/>.
- Nakazawa, T., 1986: Mean features of 30-60 day variations as inferred from 8-year OLR data. *J. Meteor. Soc. Japan*, **64**, 777–786.
- Nakazawa, T., 1988: Tropical super clusters within intraseasonal variations over the western Pacific. *J. Meteor. Soc. Japan*, **66**, 823–839.
- Phillips, N. A., 2000: The start of numerical weather prediction in the United States. A. Spekat, Ed., *50th Anniversary of Numerical Weather Prediction. Commemorative Symposium.*, Deutsche Meteorologische Gesellschaft, 13–28.

- Schubert, W. H., P. E. Ciesielski, D. E. Stevens, and H.-C. Kuo, 1991: Potential vorticity modeling of the ITCZ and the Hadley circulation. *J. Atmos. Sci.*, **48**, 1493–1509.
- Schubert, W. H., and M. T. Masarik, 2006: Potential vorticity aspects of the MJO. *Dynam. Atmos. Oceans*, **42**, 127–151.
- Silva Dias, P. L., W. H. Schubert, and M. DeMaria, 1983: Large-scale response of the tropical atmosphere to transient convection. *J. Atmos. Sci.*, **40**, 2689–2707.
- Slingo, J. M., and Coauthors, 1996: Intraseasonal oscillations in 15 atmospheric general circulation models: Results from an AMIP diagnostic subproject. *Clim. Dynam.*, **12**, 325–357.
- Stevens, D. E., H.-C. Kuo, W. H. Schubert, and P. E. Ciesielski, 1990: Quasi-balanced dynamics in the tropics. *J. Atmos. Sci.*, **47**, 2262–2273.
- Tomita, H., H. Miura, S. Iga, T. Nasuno, and M. Satoh, 2005: A global cloud-resolving simulation: Preliminary results from an aqua planet experiment. *Geophys. Res. Lett.*, **32**, 1–4. L08805, doi:10.1029/2005GL022459.
- Wang, B., 2005: *Intraseasonal Variability in the Atmosphere-Ocean Climate System*, chap. 10: Theory. Springer-Praxis, Chichester, UK, 307–360. (Eds.) William K.M. Lau and Duane E. Waliser.
- Wheeler, M., and G. N. Kiladis, 1999: Convectively coupled equatorial waves: Analysis of clouds and temperature in the wavenumber-frequency domain. *J. Atmos. Sci.*, **56**, 374–399.
- Wu, Z., and D. W. Moore, 2004: The completeness of eigenfunctions of the tidal equation on an equatorial beta plane. *J. Atmos. Sci.*, **61**, 769–774.
- Yanai, M., B. Chen, and W.-W. Tung, 2000: The Madden-Julian oscillation observed during the TOGA COARE IOP: Global view. *J. Atmos. Sci.*, **57**, 2374–2396.
- Zhang, C., 2005: Madden-Julian oscillation. *Rev. Geophys.*, **43**, 1–36.
- Zhang, C., and M. Dong, 2004: Seasonality in the Madden-Julian oscillation. *J. Climate*, **17**, 3169–3180.